

PHOTOELASTIC ANALYSIS OF RESIDUAL STRESS ARISING FROM WATER INTERACTION AT GLASS SURFACES

Bronson Hausmann

Submitted in Partial Fulfillment of the Requirements
For the Degree of

DOCTOR OF PHILOSOPHY

Approved by:
Minoru Tomozawa, Chair
Thierry Blanchet
Liping Huang
Yunfeng Shi



Department of Materials Science and Engineering
Rensselaer Polytechnic Institute
Troy, New York

[August 2022]

Submitted June 2022

© Copyright 2022

By
Bronson Hausmann
All Rights Reserved

TABLE OF CONTENTS

| | |
|--|------|
| LIST OF TABLES | vi |
| LIST OF FIGURES | vii |
| ACKNOWLEDGEMENT | xiii |
| ABSTRACT | xiv |
| 1. INTRODUCTION | 1 |
| 1.1 Water and silica interaction | 1 |
| 1.1.1 Water diffusion in silica | 1 |
| 1.1.2 Surface stress relaxation | 5 |
| 1.2 Water and sodium trisilicate glass: Case II diffusion | 7 |
| 1.3 Photoelastic stress measurement | 10 |
| 2. RESIDUAL STRESS IN SILICA GLASS FIBER: TENSILE SURFACE STRESS RELAXATION | 15 |
| 2.1 Experimental procedure | 17 |
| 2.2 Results | 23 |
| 2.3 Discussion | 33 |
| 2.4 Conclusion | 36 |
| 2.5 Derivation of tensile stress relaxation model | 36 |
| 3. RESIDUAL STRESS IN SILICA GLASS: BENDING OF FIBERS AND SHEAR STRESS RELAXATION OF RODS | 40 |

| | |
|--|----|
| 3.2 Fiber bending | 41 |
| 3.2.1 Analysis of residual bending stress | 41 |
| 3.2.2 Experimental procedure | 46 |
| 3.2.3 Results | 48 |
| 3.2.4 Discussion | 54 |
| 3.3 Shear stress relaxation and residual stress | 56 |
| 3.3.1 Analysis of residual shear stress | 56 |
| 3.3.2 Experimental procedure | 58 |
| 3.3.3 Results | 60 |
| 3.3.4 Discussion | 64 |
| 3.4 Conclusion | 66 |
| 4. RESIDUAL STRESS AND WATER DIFFUSION IN AT-REST SILICA GLASS PLATES AT LOW TEMPERATURES | 67 |
| 4.1 Experimental procedure | 68 |
| 4.1.1 Sample preparation | 68 |
| 4.1.2 Stress measurement | 70 |
| 4.2 Results | 73 |
| 4.3 Discussion | 78 |
| 4.4 Conclusion | 78 |
| 5. CASE II DIFFUSION IN SODIUM SILICATE GLASS | 79 |

| | |
|---|-----|
| 5.1 Experimental procedure | 83 |
| 5.2 Results | 87 |
| 5.3 Discussion | 90 |
| 5.4 Conclusions | 95 |
| 6. CONCLUSIONS | 97 |
| REFERENCES | 99 |
| APPENDIX A: SÈNARMONT METHOD JONES MATRIX EVALUATION | 106 |
| APPENDIX B: FORCE BALANCE IN FIBER CROSS SECTION FOUND BY DIFFERENT INTEGRATIONS | 109 |

LIST OF TABLES

| | |
|---|----|
| Table 2.1. Estimated model parameters, $\pm 95\%$ confidence bounds, and surface residual stress estimate as defined in section 2.5. Relaxation depth z , applied tensile stress, bulk structural anisotropy k , and surface residual stress estimates. All heat treatments were performed at 200°C for 60 seconds..... | 29 |
| Table 3.1. Diffusivity of bending stress relaxation, measured by bending angle Φ and retardance fit of z | 53 |
| Table 3.2. Comparison of surface shear stress relaxation depth and diffusivity by method. | 63 |

LIST OF FIGURES

| | |
|---|----|
| Figure 1.1. Comparison of effective diffusivity of structural relaxation to diffusivity of molecular water estimated from the diffusion-reaction model by Doremus ⁴ and apparent OH diffusivity as measured by IR spectroscopy by Davis. ⁶ | 2 |
| Figure 1.2. Surface OH concentration as measured by FTIR spectroscopy of successively etched Suprasil W-2 plate. Plot from data collected by Davis and Tomozawa. ⁶ | 3 |
| Figure 1.3. OH concentration at various heat treatment times, showing departures from equilibrium as estimated from high-temperature solubility. Plot from data collected by Wakabayashi and Tomozawa ⁸ and Davis. ¹⁹ | 4 |
| Figure 1.4. Effective diffusivity of surface stress relaxation as measured by residual bending curvature. Rate of relaxation is highly sensitive to temperature and environmental water content. OH diffusivity, ⁶ structural relaxation, ²² and molecular water diffusivity ⁴ estimates are provided for comparison. Surface stress relaxation data collected by Lezzi et al. ¹⁶ | 6 |
| Figure 1.5. Schematic of the concentration profile expected for case II diffusion, indicating diffusion interface X as defined in equation (1.3). Similar schematics have been previously proposed by Crank, ²⁴ Wang <i>et al.</i> , ³⁰ Thomas and Windle, ³¹ and Edwards and Cohen. ³² | 8 |
| Figure 1.6. Approximation of the boundary between Fickian and case II diffusion behavior in sodium trisilicate glass as a function of initial water content of the glass and temperature during diffusion. Data from Tomozawa and Molinelli. ³³ | 10 |
| Figure 1.7. Schematic of optical elements and sample in the configuration used for the Sénarmont method. Retardance of the sample is measured by its interaction with the quarter wave plate. Elliptically polarized light which is produced by the sample enters the quarter wave plate and is emitted as rotated, linearly polarized light. The angle of rotation is proportional to the retardance. Rotation of the analyzer allows for this angle to be calculated and converted into retardance. Sign convention is from the perspective of the observer as opposed to the source..... | 12 |
| Figure 2.1. (a) Schematic of relevant optical elements in the microscope and (b) outgoing light polarization following each component. Randomly polarized light is first filtered to 546 nm green light before becoming linearly polarized. This linearly polarized light passes through the fiber and is rendered elliptically polarized, with a fast (ordinary) and slow (extraordinary) component related to the retardance. This light is again converted back to linearly polarized light at a new angle via quarter wave plate. The angle can be determined as a function of analyzer angle, as intensity is minimized when the analyzer is perpendicular to the quarter wave plate output. This minimized intensity is measured via the attached camera to calculate the retardance at a given point in the fiber..... | 19 |
| Figure 2.2. Schematic of fiber geometry in relation to incoming microscope light as described in equation (2.3). Coordinates as defined here are used throughout the work | |

when discussing the fiber cross section. I/I_0 is the relative intensity of light as measured by the microscope camera, x and y are the horizontal and vertical directions in the fiber cross section, r is an interior radial position in the fiber, $r_0 = 62.5 \mu\text{m}$ is the radius of the fiber, and z is the characteristic depth of surface stress relaxation. 22

Figure 2.3. (a) Color map of as-received fiber retardance created using the same process as the profile measurement extended to the full microscope field of view. (b) measured retardance profile of as-received fiber, with fiber surface x position and the zero point of retardance indicated in vertical and horizontal guidelines, respectively. Points are the measured data while the line is a guide to the eye. 24

Figure 2.4. Model fit of as-received fiber retardance measurement, showing excess of internal uniform “tensile stress.” As there is no force balance to account for this tensile stress, it is more proper to discuss it as a plastic strain, likely resulting from the fiber drawing process. 25

Figure 2.5. (a) A color map generated from a heat-treated fiber (650°C , 10 min at rest in lab air), revealing imbalanced apparent tensile stress in the fiber interior. (b) Corresponding retardation profile. 27

Figure 2.6. Resultant fit between the combined retardation of residual stress due to surface stress relaxation and structural anisotropy and the measurement. 28

Figure 2.7. (a) Progressive strengthening via surface stress relaxation using progressively higher applied stress during heat treatment at 200°C for 60 seconds and (b) an enlarged region of interest as indicated in (a), with error bars on the highest curve representative of those on each curve. Note that the peak height increases systematically with increasing applied stress during heat treatment. The drop in retardance near the fiber surface is due to the measurement being over an increasingly short path length. In reality, the stress per path length increases significantly at the surface. 31

Figure 2.8. Progressive surface etching, with retardance zero point and fiber surface indicated with thin guidelines. (a) Surface compression peaks drop with etching, leaving a slightly smaller remnant retardance. (b) Further etching past $1.5 \mu\text{m}$ results in little change to bulk retardance, implying it is a result of an inelastic strain, as only apparent tensile stress remains. Note that the scale of y axis of (b) is magnified by about three times compared with (a). 32

Figure 2.9. (a) Plot of retardance with variations in parameter z with σ_{applied} fixed at 1.0 GPa (b) as well as variations in parameter σ_{applied} with z fixed at $0.75 \mu\text{m}$. The plots shown use the stress optic coefficient of Suprasil II.⁷³ 39

Figure 3.1. Schematic of the residual stress distribution in a fiber cross-section with radius r_0 following removal of the applied bend after relaxation in a two-point bending configuration. The relaxation depth is denoted by z . At the apex of the bend, the maximum tensile strain was applied at position $(x = r_0, y = 0)$ during bending and the maximum compressive strain was applied at position $(x = -r_0, y = 0)$. This results in a residual stress

in the fiber axial direction of opposite sign of the applied strain, compressive stress at ($x = r_0$, $y = 0$) and tensile at ($x = -r_0$, $y = 0$) for example. Polarized light was passed through the sample in the y direction in order to measure the stress distribution in the fiber as a function of x 44

Figure 3.2. Plot of the change in stress profile following surface stress relaxation in bending as developed previously by Lezzi et al.²¹ A constant bending moment is applied resulting in an initial stress profile (equation (3.4)). Upon heat-treatment in the presence of water, surface stress relaxation takes place (equation (3.5)). Here, relaxation is assumed to follow an error function profile with all stress relaxed at $x = r_0$. After removing the applied bending, the residual stress in the near-surface which was previously under compression is now in tension and vice versa (equations (3.8) and (3.13)). The interior stress, however, retains the same sign as the initial stress. The relaxation depth $z/r_0 = 0.05$ is over-exaggerated for visibility. 46

Figure 3.3. (a) Example of a measured fiber bending retardance map of a 500°C, 408 h treatment as measured with retardance profile. The positive y direction corresponds to negative retardance and thus residual compressive stress. (b) Theory fit following heat treatments at 500°C from 24 to 408 hours under a maximum bending stress of 728 MPa. Fiber edges are indicated by vertical lines. 48

Figure 3.4. Fiber bending retardance data fit using equation (3.14). Curves are shown to fit to the optical retardance measurements for samples heat treated at (a) 500°C and (b) 400°C with a maximum bending stress of 728 MPa for 408 hours. In this case, the tensile and compressive stress fits of depth z do not appear to differ significantly. The fiber surface is indicated by solid vertical lines, with z depth indicated by dashed lines. Retardance corresponding to compressive stress is positive. 49

Figure 3.5. Fiber bending retardance profile for sample heat treated at 300°C under a maximum bending stress of 728 MPa for 168 hours. The slight deviation between peak widths for the side which was heated under compression (left) versus tension (right) is apparent at this lower temperature. 50

Figure 3.6. Arrhenius plot of bending relaxation diffusivity for various stress values. Line indicates activation energy of 122 ± 8 kJ/mol. 51

Figure 3.7. Arrhenius plot comparing diffusivity measurement methods as applied in this work and previous work.⁷⁸ The current work's measurements are differentiated by applied stress. Dashed lines indicate the activation energy fit for retardance and bending angle diffusivity calculations (122 ± 8 and 109 ± 14 kJ/mol, respectively). In all cases, diffusivity calculated by bending angle measurement was slightly higher than the corresponding retardance measurement calculation. 52

Figure 3.8. Comparison of diffusivity values calculated using the two discussed methods. A linear regression was applied to demonstrate the systematic difference in calculated diffusivities of about 10 percent overall. 54

| | |
|--|----|
| Figure 3.9. Schematic of shear stress relaxation relative to the maximum applied shear stress. Applied stress is defined by equation (3.14). Once the stress has relaxed to depth $z = 0.05r_o$, the stress is defined by equation (3.16). The residual stress following removal of the applied shear strain is defined by equation (3.24). | 58 |
| Figure 3.10. Schematic of shear relaxation sample geometry. Gage section was cut and polished to a consistent thickness for six samples. Dimensions indicated correspond to those in equations (3.13) and (3.14). The line across the section surface corresponds to the scribe mark used for section alignment. | 59 |
| Figure 3.11. A superposition of six individual radial profiles is shown, confirming the predicted residual surface stress form but lacking necessary detail for fitting. The vertical lines mark the sample surface. | 61 |
| Figure 3.12. (a) High magnification image of the sample surface. Sample section interior is shown in the bottom right while the index matching oil is in the upper left. (b) Radial profile fit to equation (3.26). Relaxation depth z is indicated by the dashed line and the sample surface is indicated by the solid line..... | 62 |
| Figure 3.13. Torque relaxation during heat treatment with fits using equation (3.21) and (3.28)..... | 63 |
| Figure 3.14. Deviation from thickness measured by micrometer as a function of radial position for one sample, as measured by profilometer. The solid curves are profiles measured from several sample rotations, with an average given by the dashed line. Maximum change in depth near the sample surface was found to be about 10 microns..... | 65 |
| Figure 4.1. a.) Schematic of silica parent sample with the surface polished before heat treatment indicated with shading and approximate dimensions. An interior section is removed for characterization as indicated by the dashed lines. Incremental heat-treatment and thus water diffusion can be evaluated by subsequent sectioning. b.) Polishing of the cut cross section, and retardance measurement of said cross section is performed perpendicular to the diffusion surface or interest. Dimension y is the cross-section thickness (~ 2 mm) and x is the direction of diffusion, measured from the shaded surface inward. | 70 |
| Figure 4.2. Schematic of the microscope configuration used for retardance measurement with the Sénarmont method. The optical components are shown above with the polarization state of the light shown schematically below. Elliptically polarized light is output from the sample which is at 45 degrees to the incoming polarized light. The difference in semimajor axes is proportional to the birefringence. Analyzer angle θ is incremented to find the minimum intensity resulting from a rotation of polarized light by the quarter wave plate, and thus retardance via equation (4.5)..... | 72 |
| Figure 4.3. Experimental configuration during retardance measurement following heat-treatment illustrating orientation between the microscope and sample fixture. The sample is indicated in the center and measures roughly 10mm x 7mm x 2mm. Diffusion direction | |

| | |
|---|----|
| during heat treatment is indicated by arrows within the sample along the x axis defined in figure 4.1. | 72 |
| Figure 4.4. Retardance map of silica glass sample surfaces for samples heat-treated for 400 hours at 350 °C (a) and 650 °C (b). Glass surface is indicated with an arrow with the water diffusion into glass proceeding in the direction of the arrow (along coordinate x). | 74 |
| Figure 4.5. Residual stress profiles plotted alongside OH concentration profiles for 350 °C. OH concentration profile adapted from Davis. ¹⁹ | 75 |
| Figure 4.6. Residual stress profiles plotted alongside OH concentration profiles for 650 °C. OH concentration profile adapted from Davis. ¹⁹ Over identical time periods, surface OH concentration is found to initially increase then decrease, while the same pattern is observed in residual stress following an initial delay. | 76 |
| Figure 4.7. Comparison of surface residual stress (closed points) and surface OH content (open points) within the first 0.5 μm of material as a function of heat treatment time for 350 °C (a) and 650 °C (b). Surface OH concentration adapted from reference. ⁶ Note the slight delay at the higher temperature between surface OH concentration and residual stress change. | 77 |
| Figure 5.1. a.) Schematic of typical diffusion interface progression of case II diffusion, showing the interface progression at point X. b.) Schematic curves describing case II and Fick's law interface progression as a function of time. | 80 |
| Figure 5.2. Schematic of the long-time behavior of case II diffusion, which has been observed to approach Fick's law as a result of stress relaxation in the case of glassy polymers. | 81 |
| Figure 5.3. DTA curve depicting the glass transition temperature estimate from the change in heat of the glass sample. T_g value agrees with a sodium trisilicate glass containing approximately 0.1 wt% water. | 84 |
| Figure 5.4. FTIR spectrum of two samples of sodium trisilicate glass polished to the indicated thickness. Water content was estimated to be 800 ± 50 wt. ppm using a practical extinction coefficient of 24 for the 3500 cm^{-1} as previously determined by Acocella. ²⁷ The relevant band is indicated by the arrow for both spectra. | 85 |
| Figure 5.5. Schematic of sample configuration during heat treatment. Samples are suspended above deionized water, upon a silica plate, within a sealed PTFE vessel to ensure saturated vapor pressure during the experiment. | 86 |
| Figure 5.6. Schematic of the heated stage in relation to the incident light of the microscope and the sample. | 87 |
| Figure 5.7. Diffusion interface depth versus time for water in sodium trisilicate at 80 °C saturated water vapor. Fit is linear with an intercept of zero and rate of $4.67 \pm 0.23\text{ }\mu\text{m per hour}$ | 88 |

| | |
|---|-----|
| Figure 5.8. Residual stress profiles on the unreacted side of the diffusion interface in sodium silicate for 4 to 96 hours. Between 6 and 12 hours, the maximum stress begins to decrease. The interface appears to progress more slowly at this inflection but is still within experimental error for a constant interface velocity. | 89 |
| Figure 5.9. Measured maximum birefringence as a function of heat treatment time. A maximum is reached at about 12 hours at which point an exponential decay occurs as described by equation (5.7), with a relaxation time of about 37 hours..... | 90 |
| Figure 5.10. Comparison of dominant diffusion behavior in sodium trisilicate glass as a function of temperature and water content of the unreacted glass. The dependence of T_g with water content is also included. Data collected by Tomozawa and Molinelli. ³³ | 92 |
| Figure 5.11. Retardance profiles from 12 to 96 hours displaying nearly identical initial slopes from the surface inward. The data was fit to an average slope of 0.014 ± 0.009 MPa/mm, or 0.0341 nm/mm^2 | 93 |
| Figure 5.12. Schematic of the surface stress relaxation in comparison to the expected stress pattern assuming an error function relaxation, as observed in surface stress relaxation elsewhere. This relaxation accounts for the positive stress gradient at the surface whereas a negative gradient is to be expected if there were no relaxation. | 94 |
| Figure 5.13. Negative stress gradient near the diffusion interface as a function of heat treatment time. The gradient is seen to decrease with time in a manner similar to the maximum tensile stress as seen in figure 5.9, although at a much faster pace. The relaxation time was estimated using the same exponential proportion as equation (5.7) and was found to be 3.75 ± 1 hour..... | 95 |
| Figure B.1. Schematic of a fiber cross section showing equivalent stress profiles of equivalent diameter at different angles. | 110 |
| Figure B.2. Schematic of a fiber cross section showing the variation in path length as a function of x position. | 111 |

ACKNOWLEDGEMENT

I want to thank my advisor Professor Tomozawa for his tireless mentorship and constant enthusiasm for discovering the hidden causes of glass behavior. He and every member of my committee have been a vital source of insight at every point of my program.

I must also acknowledge the valuable insight of my many other collaborators including in particular my fellow researchers Emily, Arron, and Zhenhan. None of the work presented here would have been possible without the support I received from these amazing individuals.

Finally I want to extend my deepest gratitude for the enduring support of my friends and family, in particular to my partner Athena for her constant love and encouragement and to my parents for ensuring that my curiosity could carry me to such an amazing field of study.

Felix qui potuit rerum cognoscere causas

Happy are they who are able to know the causes of a thing

-Virgil, *Georgicon* 2.490

ABSTRACT

A high-resolution characterization technique was developed based on existing polarized light microscopy techniques in concert with digital photography. This technique was employed to measure the residual stress near glass surfaces in response to environmental water and various forms of mechanical deformation and thermal processing. Techniques were developed with the goal of clarifying aspects of the behavior regarding three cases in particular: 1.) surface stress relaxation in silica glass fibers; 2.) anomalous water diffusion and stress generation in low-water silica; 3.) the connection between stress and case II diffusion in sodium silicate glass.

In each case it was found that residual stress near the glass surface contributes significantly to aspects of the observed material properties. This is seen specifically in 1.) the strengthening via surface compressive stress of glass which has undergone surface stress relaxation; 2.) the time dependence of surface compressive stress generation in low-water silica which correlates with hydroxyl concentration; 3.) the tensile stress gradient present in sodium silicate glass during case II diffusion which results in a constant flux at the diffusion interface. Explanations for these observations are discussed in light of the new findings. Results agree with what previous researchers have hypothesized but never directly observed.

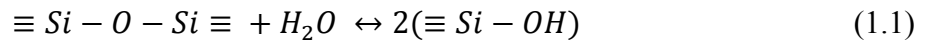
1. INTRODUCTION

Water and silica are among the most abundant substances on the planet, yet interactions between water and silicate glasses lack the detailed understanding one might expect from such a ubiquitous pair. The study of water at glass surfaces has historically been interested in its effect upon the structure and mechanical properties of glass. The current understanding was constructed through characterization of water's influence on crack growth,¹⁻³ measurements of water diffusion into the silica network,⁴⁻⁹ and detailed analysis of the relaxation behavior of glass (near the surface and in the bulk).¹⁰⁻¹⁵ Many intersections exist within these works with even greater opportunity to explore further connections. This work seeks to further strengthen the connections between such understandings by analysis of residual stress near the glass surface which arise from water interaction under various conditions.

1.1 Water and silica interaction

1.1.1 Water diffusion in silica

Molecular water is theorized to enter silica and react to form hydroxyl (OH) groups within the network by the following reaction:



This reaction is a hydration of bridging oxygen bonds within the network.^{4,5} The reaction quickly reaches equilibrium at high temperatures, but this may not be assumed at temperatures well below the glass transition temperature, where structural relaxation may be occurring at a limiting timescale (figure 1.1).^{6,9} In any case, although OH concentration is seen to increase with time as expected by equation 1.1, H₂O is believed to be the only significantly mobile diffusion

species involved in the reaction. Thus discussions of OH diffusion are in reality discussions of “apparent diffusion” and instead represent conversion of molecular water via equation 1.1.

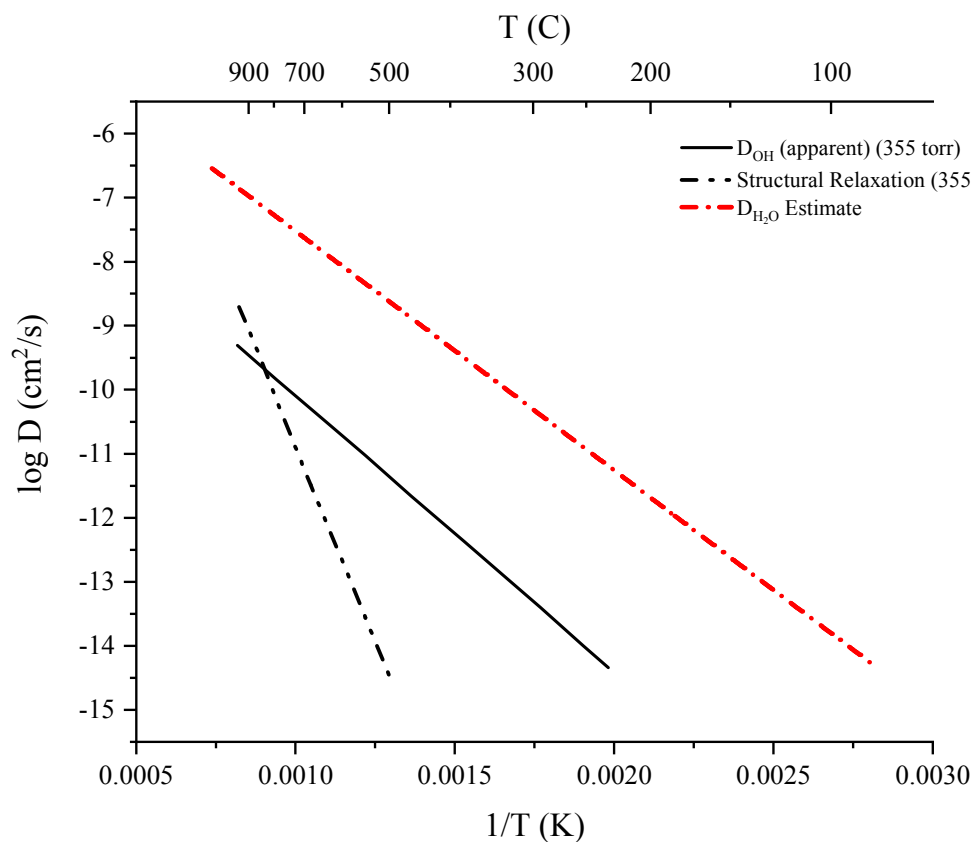


Figure 1.1. Comparison of effective diffusivity of structural relaxation to diffusivity of molecular water estimated from the diffusion-reaction model by Doremus⁴ and apparent OH diffusivity as measured by IR spectroscopy by Davis.⁶

Beyond the influences of temperature, concentration of environmental water vapor and applied stress upon the glass network have both been shown to influence water diffusion through acceleration or inhibition of the reaction.^{16–18} These effects are more pronounced at low temperatures and have been observed in surface stress relaxation experiments as well as in the diffusion of bulk silica surfaces heat-treated in the absence of applied stress.

For silica surfaces at rest, it was found that apparent surface OH diffusivity changes as a function of time.⁸ Using IR spectroscopy, the surface OH concentration was measured as a function of heat treatment time in a 355 Torr p_{H_2O} environment.^{6,9} At temperatures below 650 °C, equilibrium is approached gradually while above this temperature, an initial sharp increase in surface OH concentration is followed by a gradual decrease (figure 1.2).^{6,19} This has been discussed previously in terms of a change in solubility of the glass surface as a function of time, with an equilibrium solubility estimated from higher temperature water diffusion at or above 850 °C (figure 1.3).⁹

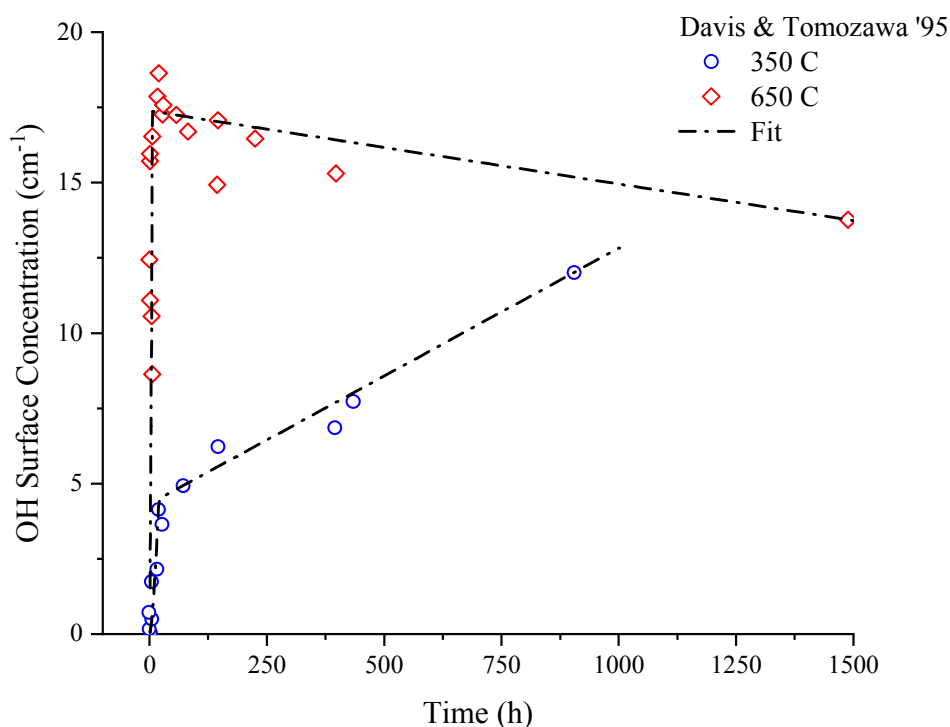


Figure 1.2. Surface OH concentration as measured by FTIR spectroscopy of successively etched Suprasil W-2 plate. Plot from data collected by Davis and Tomozawa.⁶

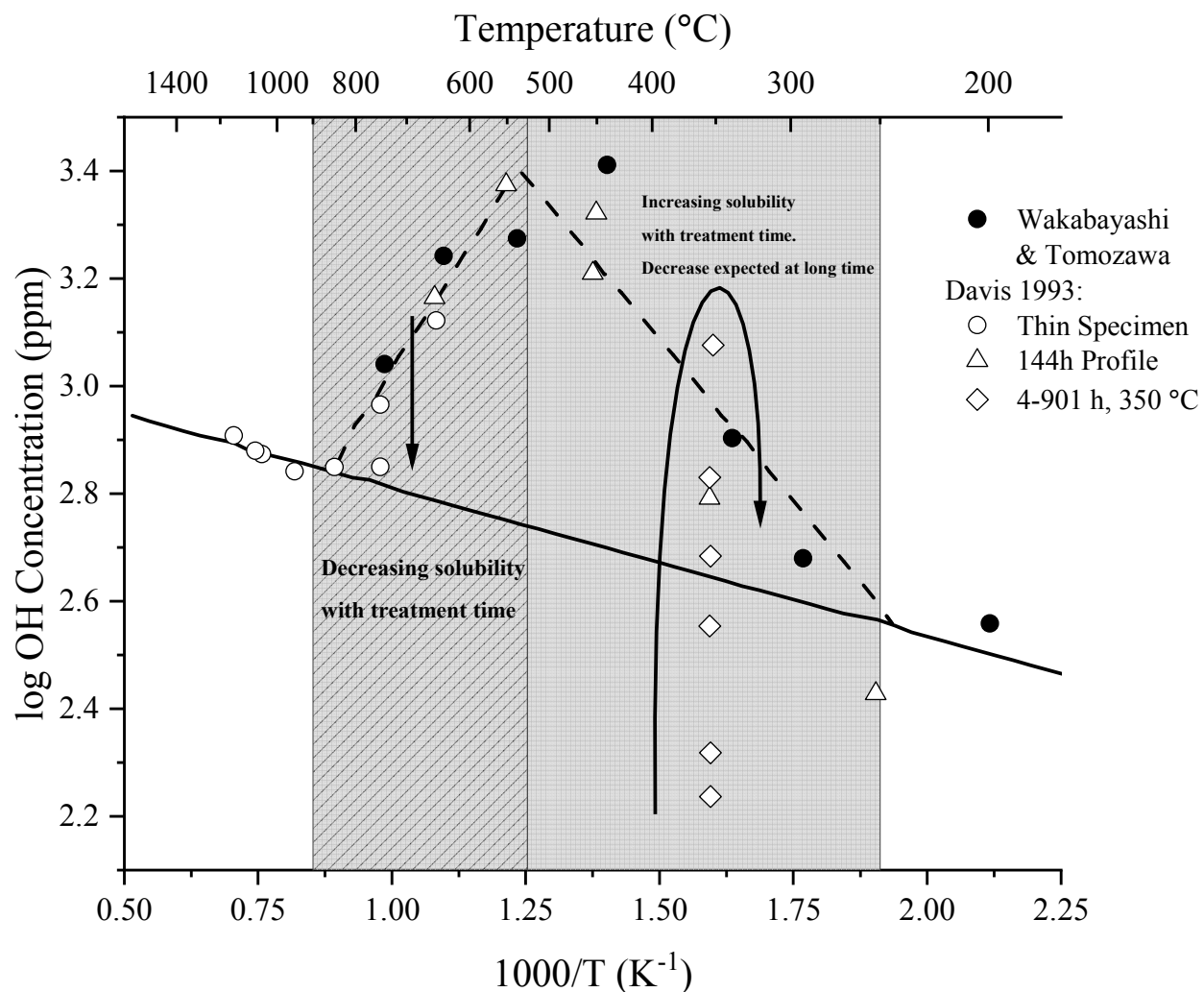


Figure 1.3. OH concentration at various heat treatment times, showing departures from equilibrium as estimated from high-temperature solubility. Plot from data collected by Wakabayashi and Tomozawa⁸ and Davis.¹⁹

Surface stress generation and relaxation during water diffusion is hypothesized to be the origin of this time-dependent solubility behavior. A primary goal of the present work is to compare the evolution of residual stress near the glass surface during this anomalous diffusion behavior to previously obtained OH concentration profiles.

1.1.2 Surface stress relaxation

Fast relaxation of applied stress in silica glass was first observed through heat treatment of silica optical fibers under a constant bending moment.²⁰ After treatment it was found that fibers retained a residual curvature proportional to the square root of heat treatment time. Successive etching of the fibers was found to result in un-bending, confirming the phenomenon to be caused by surface relaxation and subsequent generation of a residual stress responsible for the deformation. The effective diffusivity of this relaxation was found to be thermally activated and sensitive to water vapor pressure, in agreement with expectations for the reaction of molecular water with the silica network (figure 1.4).^{12, 20} Further work found that surface stress relaxation can be leveraged as a means of strengthening glass fibers. Short-time heat treatment of fibers at 200°C in lab air resulted in statistically significant two-point bending strength increase in both silica and E-glass fibers.^{13, 21} This strengthening was proportional to the applied stress during heat treatment, implying a residual compressive stress proportional to the applied tensile stress was likely the cause of strengthening.

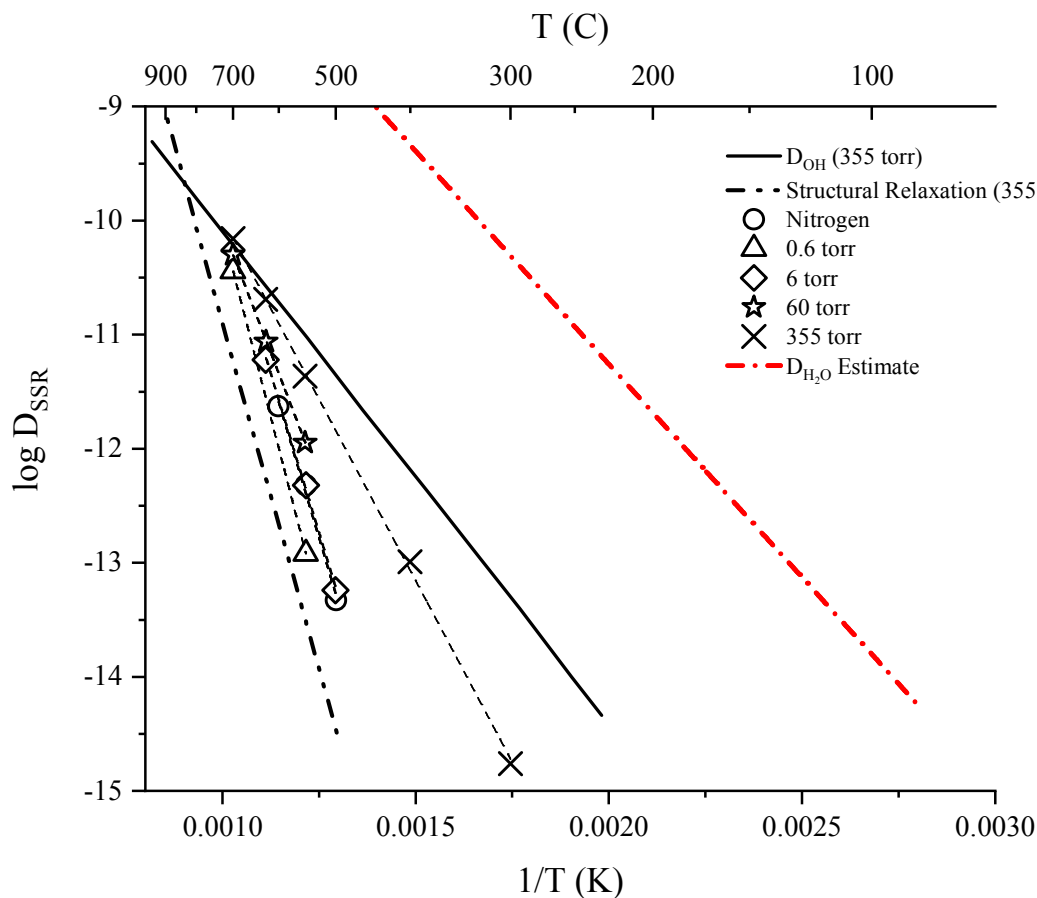


Figure 1.4. Effective diffusivity of surface stress relaxation as measured by residual bending curvature. Rate of relaxation is highly sensitive to temperature and environmental water content. OH diffusivity,⁶ structural relaxation,²² and molecular water diffusivity⁴ estimates are provided for comparison. Surface stress relaxation data collected by Lezzi et al.¹⁶

Further work revealed torsion (shear stress) relaxation in silica rods, indicating a change in volume was not necessary for surface stress relaxation to occur.²³ As will be discussed, this result also indicated that residual stress from water entry during diffusion is not the cause of compressive stress observed in optical fibers heat-treated under tension. Because surface stress relaxation is found to occur in the absence of volume change (shear), it must therefore act via a mechanism separate from volume change. Chapter 2 discusses the use of experimental

techniques identical to those of the original works to replicate findings while additionally directly characterizing the residual stress profiles of samples through photoelastic techniques. While previous work provided indirect evidence of the effects surface stress relaxation (via residual curvature, an increase in bending strength, or torsion relaxation), this work's stress measurements confirm the specific behavior of surface stress relaxation through direct observation of the residual stress profiles. In all cases, it is assumed that surface stress relaxation follows a complementary error function profile, where depth of relaxation is proportional to the square root of time:

$$z = 2\sqrt{Dt} \quad (1.2)$$

where z is the depth of diffusion or relaxation, D is the diffusivity, and t is time. The diffusivity itself has been shown to be sensitive to environmental conditions as well as applied stress.

1.2 Water and sodium trisilicate glass: Case II diffusion

It has been observed that in sodium silicate glasses, water diffusion results in the formation of a hydrated layer. This layer forms a sharp interface with the unreacted, lower water content glass (figure 1.5).^{24, 25} Progression of this interface is similar to the diffusion/reaction behavior observed in polymers exposed to solvents and is referred to as “case II diffusion.”²⁶ In addition to a step-function water concentration profile (both molecular water and OH to differing concentrations)²⁷, the interface is observed to progress through the material linearly with time.^{28, 29} This is in opposition to the diffusion behavior predicted by Fick's Law, which anticipates a square root time dependency along a concentration gradient.

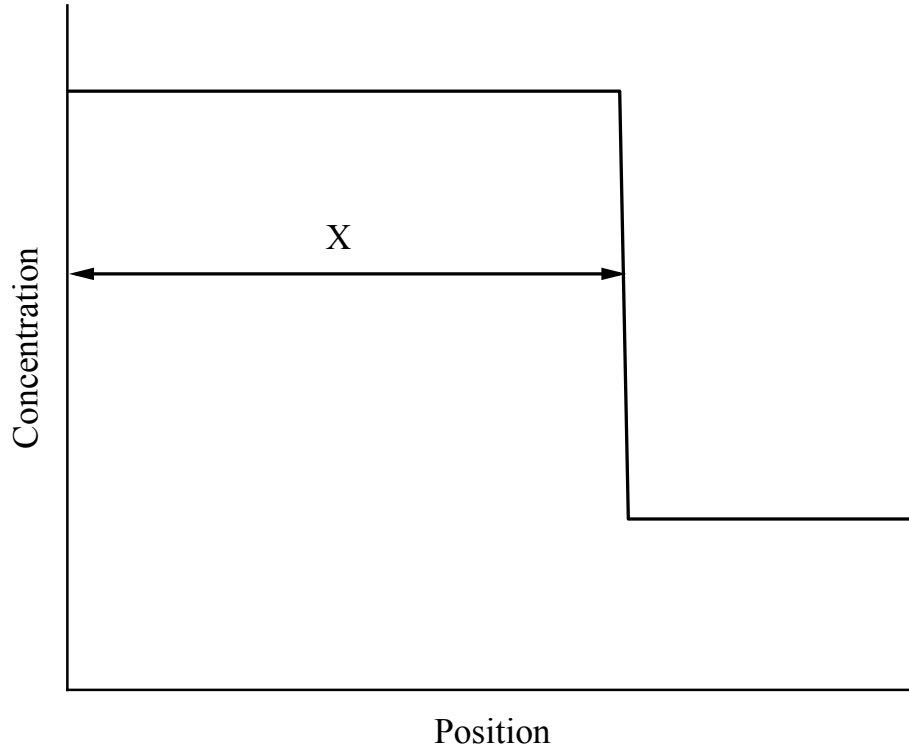


Figure 1.5. Schematic of the concentration profile expected for case II diffusion, indicating diffusion interface X as defined in equation (1.3). Similar schematics have been previously proposed by Crank,²⁴ Wang *et al.*,³⁰ Thomas and Windle,³¹ and Edwards and Cohen.³²

The linear progression of the diffusing interface is described by Crank as dependent upon a typical diffusivity as well as an additional contribution which determines structural relaxation during diffusion. This was later expressed as a rule of mixing by Wang *et al.*:³⁰

$$X(t) = 2k\sqrt{Dt} + \nu t \quad (1.3)$$

where X is thickness of the surface layer as a function of time, k is a material constant, D is the diffusivity of the material, and ν is the rate parameter for linear progression which Crank describes as a mobility constant accounting for stress and structural relaxations. Case II diffusion

in sodium trisilicate glass was found to occur at low temperatures, with Fick's law diffusion observed to be the dominant diffusion mechanism at relatively higher temperatures.^{28, 33} Whether case II or "Fickian" diffusion is the dominant behavior is heavily dependent both on temperature and the initial water content of the glass (thus ν increases more rapidly than D as a function of temperature or composition) (figure 1.6).³³ As the transition between case II and Fickian diffusion can be observed to occur along a contour of approximately constant viscosity (as inferred from similar curvature in the glass transition temperature as a function of water content), it is hypothesized that the dominant mechanism of diffusion is determined by the structural relaxation of the unreacted portion of the interface. To confirm this theory, the residual stress at the unreacted half of the sodium trisilicate interface was measured after various heat treatments in a saturated water vapor environment in the case II regime.

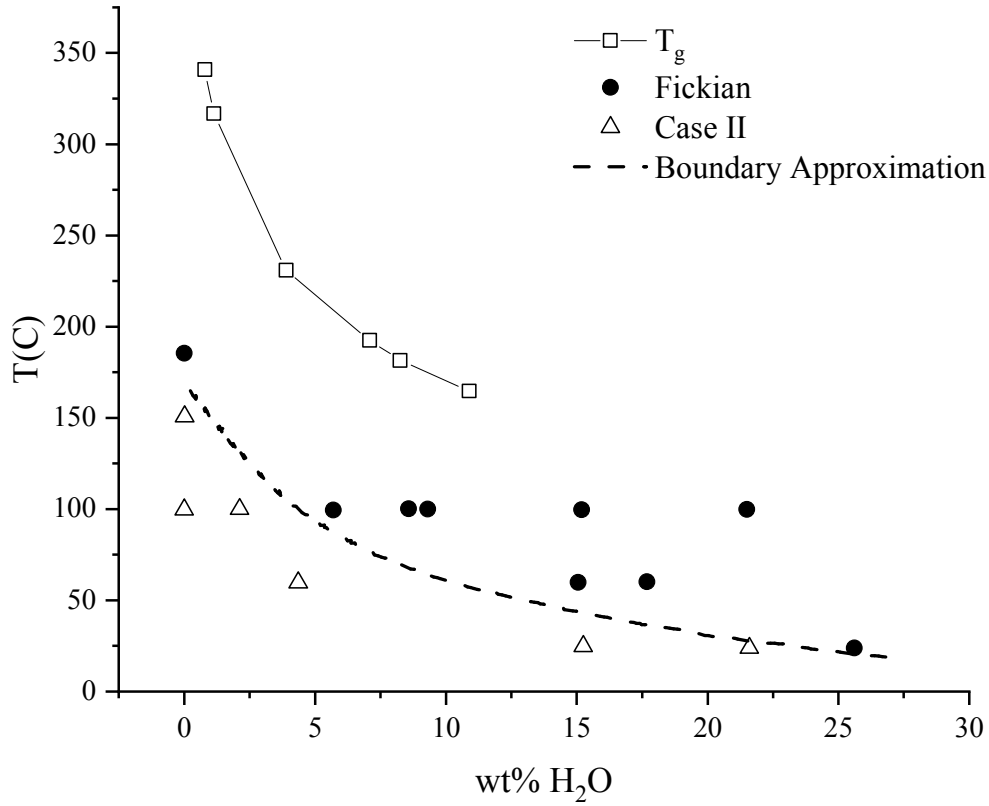


Figure 1.6. Approximation of the boundary between Fickian and case II diffusion behavior in sodium trisilicate glass as a function of initial water content of the glass and temperature during diffusion. Data from Tomozawa and Molinelli.³³

1.3 Photoelastic stress measurement

Transparent materials with structural or externally imposed anisotropy exhibit birefringence, a difference in refractive indices with respect to said anisotropy:

$$B = n_e - n_o \quad (1.4)$$

where B is the birefringence, n_e is the extraordinary refractive index resulting from the anisotropy (e.g. as induced by a tensile stress); and n_o is the ordinary refractive index for the material in an isotropic state.³⁴ Birefringence can be related to stress by the stress-optic law³⁵:

$$\sigma = \frac{B}{C} \quad (1.5)$$

where σ is the magnitude of a one-dimensional stress in the direction of the birefringence, B is birefringence in nm/mm and C is the stress-optic coefficient in Brewster [$10^{-12} \cdot Pa^{-1}$]. While birefringence is a measure of the total change in index per unit path length, it can also be thought of as a difference in the relative phase of polarized light components in degrees. This angle is related to the retardance Δ , the phase difference in nanometers as a proportion of the incident wavelength:

$$\delta = 360^\circ \cdot \left(\frac{\Delta}{\lambda}\right) \quad (1.6)$$

In this work however, relative retardation δ is treated as an intermediary and instead birefringence is reported as a measurement of retardance to remain linearly proportional to residual stress:

$$\Delta = B \cdot y \quad (1.7)$$

where Δ is the retardance in nm of phase shift, and y is the path length through the material in mm. Thus, residual stress can be calculated through measurement of sample dimensions, sample retardance, and knowledge of the material's stress optic coefficient. Measurements were taken using the Sènmarmont method, a well-established technique for measurement of small retardances along one dimension.^{36–39}

The Sènmarmont method is most readily explained for the simple case of measurement of a flat (constant path length y) sample with a constant retardance. Light consisting of a known wavelength (via interference filter) is passed through crossed polarizers. Between the polarizer (P) and analyzer (A) (the second polarizer and final optical element before the observer/camera) are the sample (S), at 45 degrees to the polarizers, and a quarter wave plate, often called a Sènmarmont compensator. For sake of clarity it will be referred to here as the quarter wave plate

(figure 1.7). All discussions of polarization rotation shall adhere to the perspective of the observer/detector, as opposed to the perspective of the source.

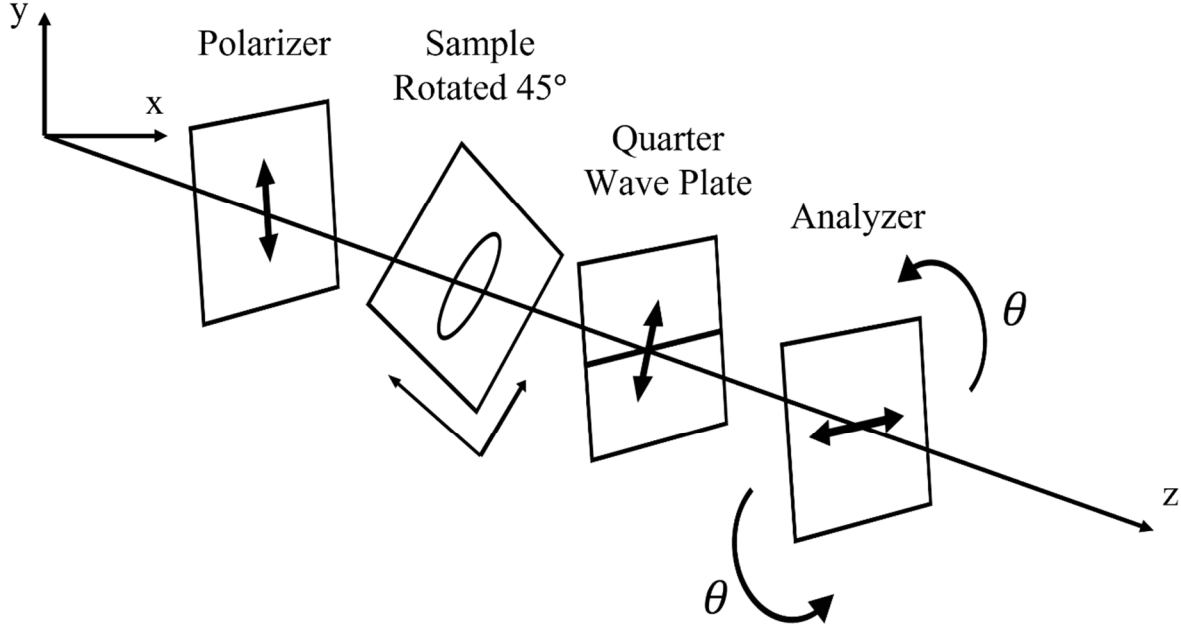


Figure 1.7. Schematic of optical elements and sample in the configuration used for the Sèarmont method. Retardance of the sample is measured by its interaction with the quarter wave plate. Elliptically polarized light which is produced by the sample enters the quarter wave plate and is emitted as rotated, linearly polarized light. The angle of rotation is proportional to the retardance. Rotation of the analyzer allows for this angle to be calculated and converted into retardance. Sign convention is from the perspective of the observer as opposed to the source.

The optics of the Sèarmont method configuration can be described via Jones calculus.^{34, 40} Jones calculus is a mathematical technique by which the effect of linear optical elements on the electric field vector of propagating light can be represented as a series of matrix operations. A starting electric field vector of unity is used to represent the randomly polarized light as produced by the microscope lamp:

$$\mathbf{E}_{in} = \begin{bmatrix} 1 \\ 1 \end{bmatrix} \quad (1.8)$$

Following from the initial vector, each element of the Sènarmon configuration is defined as a 2 column, 2 row matrix. The first element is the initial polarizer, which we will assume to be vertical:

$$\mathbf{P} = \begin{bmatrix} 0 & 0 \\ 0 & 1 \end{bmatrix} \quad (1.9)$$

This is then followed by the sample, with fixed relative retardation δ with the “faster” optical axis along the horizontal direction:

$$\mathbf{S} = \begin{bmatrix} e^{-i(\frac{\delta}{2})} & 0 \\ 0 & e^{i(\frac{\delta}{2})} \end{bmatrix} \quad (1.10)$$

Because the sample is rotated by 45 degrees relative to the polarizer and analyzer, an additional rotation operation is performed upon equation (1.10) to represent the sample as it interacts with the rest of the configuration:

$$\begin{aligned} \mathbf{S}_{rot} &= \frac{1}{2} \cdot \begin{bmatrix} 1 & -1 \\ 1 & 1 \end{bmatrix} \cdot \mathbf{S} \cdot \begin{bmatrix} 1 & 1 \\ -1 & 1 \end{bmatrix} \\ &= \begin{bmatrix} \cos\left(\frac{\delta}{2}\right) & -i \cdot \sin\left(\frac{\delta}{2}\right) \\ -i \cdot \sin\left(\frac{\delta}{2}\right) & \cos\left(\frac{\delta}{2}\right) \end{bmatrix} \end{aligned} \quad (1.11)$$

Following the sample is the quarter wave plate, with its fast axis also horizontal:

$$\mathbf{Q} = \begin{bmatrix} e^{-i(\frac{\pi}{4})} & 0 \\ 0 & e^{i(\frac{\pi}{4})} \end{bmatrix} \quad (1.12)$$

Finally the light emitted by the quarter wave plate passes through an analyzer with transmission axis at angle θ :

$$\mathbf{A} = \begin{bmatrix} \cos^2(\theta) & \sin(\theta) \cos(\theta) \\ \sin(\theta) \cos(\theta) & \sin^2(\theta) \end{bmatrix} \quad (1.13)$$

Thus to express the electric field vector output by the analyzer following the other elements of the configuration, equations (1.8), (1.9), (1.11), (1.12), and (1.13) are multiplied:

$$E_{out} = A \cdot Q \cdot S_{rot} \cdot P \cdot E_{in} \quad (1.14)$$

The magnitude of the electric field vector (which is proportional to the relative light intensity I/I_o) has a simple form, and can be found by multiplication of E_{out} with its transposed complex conjugate:

$$\begin{aligned} |E_{out}| \propto I/I_o &= E_{out}^* \cdot E_{out} \\ &= \frac{1}{2} - \frac{\cos(\delta - 2\theta)}{2} \end{aligned} \quad (1.15)$$

Thanks to the relation between the measured intensity and the intensity dependence on δ and θ , it can be deduced via inspection of equation (1.15) that light intensity is minimized as δ approaches 2θ . Thus by measuring the intensity at several values of θ , one can estimate δ for a material within the configuration. Therefore, use of equations (1.5), (1.6), (1.7), and (1.15) allows for measurement of residual stress at a point within a material. This method coupled with digital photography and image processing can thus allow for two-dimensional mapping of residual stress in an otherwise isotropic transparent material. An expansion of equations (1.14) and (1.15) is included in Appendix A.

All measurements in this work were obtained using the same polarized light microscope (Nikon Eclipse, LV-100 NPOL) equipped with a CMOS camera. Polarized light microscopy was coupled with digital photography to measure retardance near the glass surface in various experiments to follow. Previous groups have established the accuracy of quantifying retardance with the S  narmont method and digital photography,^{41, 42} while others have quantified birefringence in fibers directly following production.^{43–47} Details of the sample configuration and specific measurement considerations for such configurations are included with the respective experiments to follow.

2. RESIDUAL STRESS IN SILICA GLASS FIBER: TENSILE SURFACE STRESS RELAXATION

Silica glass fibers are known to exhibit birefringence which increases with applied axial tensile stress, such as during fiber drawing.^{47, 48} While some groups have investigated these effects in the fiber bulk, birefringence at or near the surface has not yet been explored. Birefringence can appear in glass either through residual stress or structural anisotropy. One example of the formation of residual stress in the glass surface is thermal tempering. Glass is strengthened by the formation of a surface compressive stress through rapidly cooling the glass from its softening point. Since thermal tempering requires the formation of a temperature gradient in the glass piece during cooling, it is unlikely to occur in glass fibers with a 125 μm diameter since the fiber is too thin to produce an adequate temperature distribution.⁴⁹ Structural anisotropy can occur in some organic glasses through alignment of chain structures. Among oxide glasses, phosphate glass fibers exhibit a high degree of structural birefringence through the orientation of chain structures.⁵⁰ Oxide glasses with a phase-separated structure can also exhibit birefringence when stretched due to elongation of the spherical microstructure into spheroidal shapes in the tensile direction.⁵¹ In order to explain the observed birefringence of silica glass fibers, non-Newtonian viscous flow⁵² and frozen-in viscoelasticity⁴⁶ have been proposed previously. These mechanisms may produce a uniform birefringence per sample thickness throughout a homogenous silica glass

Portions of this chapter previously appeared as:

Hausmann BD, Miller PA, Aaldenberg EM, Blanchet TA, Tomozawa M. Modeling birefringence in SiO₂ glass fiber using surface stress relaxation. *J Am Ceram Soc.* 2020;103(3):1666–1676. <https://doi.org/10.1111/jace.16900>

fiber, but the reported birefringence per unit thickness in silica glass fibers appears to vary radially.^{43, 47, 53}

Recently, a new method was discovered to strengthen glass fibers by introducing a residual compressive stress in the surface of glass fibers.⁵⁴ Subjected to a tensile stress for a short duration at a temperature far lower than the glass transition temperature (T_g) in air, the glass surface undergoes rapid stress relaxation. The process is accelerated by small amounts of water vapor, and bulk stress relaxation is negligible at these low temperatures.^{9, 23} When the applied tensile stress is removed after cooling, the fiber acquires a surface compressive stress with nearly the same magnitude as the applied tensile stress, compensated by a low tensile stress inside the fiber bulk. The strengthening of fibers by this method has been demonstrated for silica glass,¹⁶ E-glass,²¹ and soda-lime silicate glass.¹³ Fast surface stress relaxation has also been used to explain various mysterious phenomena related to the mechanical strength of glass, such as surface degradation of compressive stress made by ion-exchange,¹⁵ crack arrest,⁵⁵ and the static fatigue limit.¹⁴

Fast surface stress relaxation would also produce non-uniform birefringence in glass fibers due to the resulting stress distribution. The existence of the surface residual stress of silica glass fibers by fast surface stress relaxation has previously been confirmed using shifts in the infrared reflection peak of strengthened fibers.⁵⁶ While surface stress relaxation and the resulting residual surface compressive stress have been demonstrated for silica glass fibers primarily at low temperatures (well below T_g) and short times in lab air, e.g. 200–500 °C in 60 s for silica glass, the same phenomenon is likely to occur at the higher temperatures in an even shorter time duration during fiber drawing. At higher temperatures, however, the effect is in concert with bulk

stress relaxation as well as structural relaxation.⁹ In the present research, the radial distribution of the birefringence of silica glass fibers is measured using a polarizing microscope and compared with a theoretical model based upon fast surface stress relaxation.

2.1 Experimental procedure

Silica glass fibers with a 125 μm diameter are widely used for optical communications. Most commercial optical fibers consist of a core of about 8 μm in diameter with a slightly higher refractive index as well as a surrounding cladding with lower refractive index for a total of 125 μm . This core-cladding structure can produce residual stress due to the differences in glass compositions and properties of the glasses involved.⁵⁷ In order to simplify the birefringence observation and analysis, a coreless silica glass fiber with the same diameter as a commercial optical fiber made of Suprasil II (Heraeus Quartz Inc.) was analyzed in the current experiments. The silica glass contains 1200 wt. ppm OH, 0.1 wt. ppm Al, with all other impurities less than 0.05 wt. ppm. The glass transition temperature was estimated to be $\sim 952\text{--}1006\text{ }^{\circ}\text{C}$.^{58, 59}

Fibers were observed under a polarizing microscope (Nikon Eclipse, LV-100 NPOL) with an attached CMOS camera. Fibers were immersed in index-matching fluid matching the fiber surface index (Cargille immersion oil, $n=1.459$) and placed with the fiber axis at 45° to both polarizer and analyzer in a cross-polarization configuration. The index of the immersion oil is accurate at $25\text{ }^{\circ}\text{C}$, with a deviation of $-3.7 \cdot 10^{-4}\text{ }^{\circ}\text{C}^{-1}$. The lab environment was kept within 2 degrees of this temperature. A conventional halogen light source with a $\lambda = 546\text{ nm}$ interference filter (green) was used (figure 2.1 (a)). Functions of the optical elements of the microscope are explained briefly in figure 2.1 (b). With the focal plane positioned in the center of the sample, 25 images were captured, and the measured intensity was averaged to mitigate noise. Relative

intensity was analyzed using the digital values of the captured images, with an average standard deviation of 0.3% arising from the sensitivity of the camera. The fiber intensity profile was measured on a line perpendicular to the fiber drawing tension axis, which was used to define the x axis as perpendicular to the microscope image plane and fiber draw axis (figure 2.2). Fifty such fiber profiles were averaged from this image using 0.17 μm increments (the pixel resolution of the camera, roughly half the spatial resolution of the microscope optics) to mitigate the effect of surface dust or other noise. A quarter wave plate was used in order to make quantitative measurements of retardance via the S  narmont method.^{37, 60} This wave plate is paired to the green filter such that the retardance within the filter's wavelength is $\lambda/4$. The accuracy of the wave plate is assumed to be significantly higher than the error from the analyzer rotation. The quarter wave plate converts the elliptically polarized light resultant from the birefringent sample into linearly polarized light. This linearly polarized light has a retardance proportional to the angle of polarization that exits the wave plate (figure 2.1).³⁹ Rotation of the analyzer allows for this resultant polarization angle to be quantified for the incident light wavelength: when the analyzer's polarization is perpendicular to the light exiting the quarter wave plate, intensity is minimized.

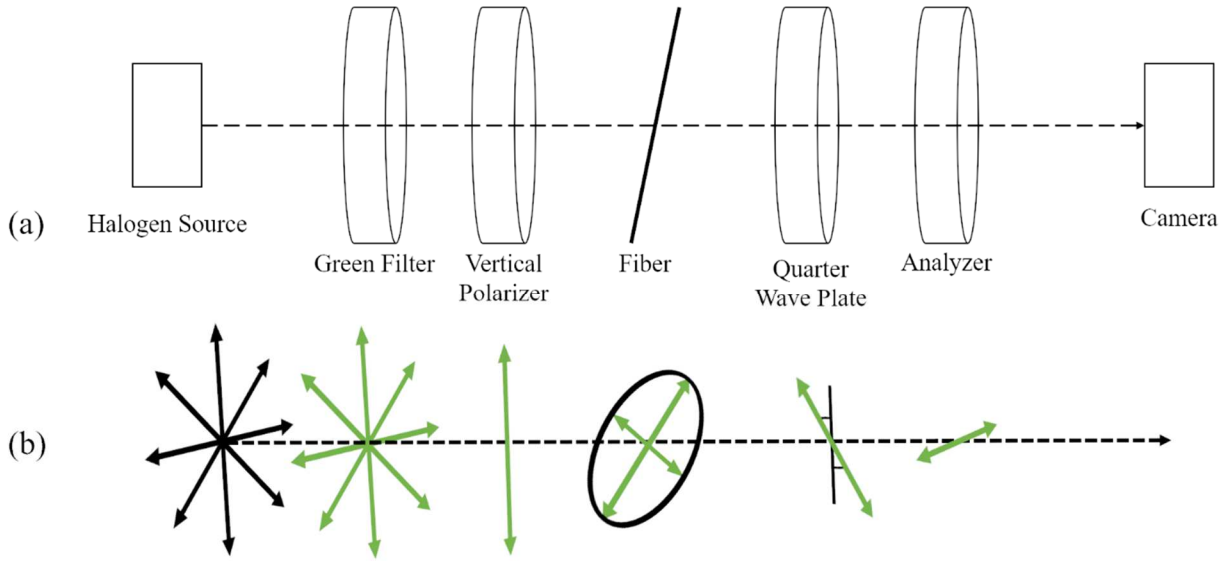


Figure 2.1. (a) Schematic of relevant optical elements in the microscope and (b) outgoing light polarization following each component. Randomly polarized light is first filtered to 546 nm green light before becoming linearly polarized. This linearly polarized light passes through the fiber and is rendered elliptically polarized, with a fast (ordinary) and slow (extraordinary) component related to the retardance. This light is again converted back to linearly polarized light at a new angle via quarter wave plate. The angle can be determined as a function of analyzer angle, as intensity is minimized when the analyzer is perpendicular to the quarter wave plate output. This minimized intensity is measured via the attached camera to calculate the retardance at a given point in the fiber.

This method and equipment are similar to those used previously by other groups.^{41, 44, 61, 62} The retardance or optical phase shift, $\Delta(x)$, is proportional to the refractive index difference and path length in a birefringent material:

$$\Delta(x) = (n_e - n_o) \cdot t(x) \quad (2.1)$$

where n_e is the refractive index of the extraordinary ray, n_o is that of the ordinary ray, and $t(x)$ is the sample thickness at horizontal position, x (figure 2.2). This index difference, a consequence of the material's response to incident polarized light, produces elliptically polarized light which varies as a function of x position along the fiber. The retardance is related to the stress by the stress-optic law:

$$\Delta(x) = C \cdot \sigma_{res}(x) \cdot t(x) \quad (2.2)$$

where C is the stress-optic coefficient of the material and σ_{res} is the residual axial stress. Many glasses including silica glass exhibit a positive stress-optical effect (i.e. tensile stress exhibiting $n_e > n_o$ *et vice versa*). Thus, tensile stress, which is defined positive, produces positive retardance. On the other hand, in literature on glass strengthening by residual surface compressive stress, it is customary to plot the surface compressive stress in positive y axis. Thus, in this study, $-\Delta(x)$, which corresponds to net axial compressive stress, will be plotted on the positive y axis as a function of fiber x position.

The S  narmont method allows a connection to be made between incident wavelength, relative intensity, and the analyzer angle relative to the fixed polarizer. Intensity measured by the camera can be shown to be a function of analyzer angle and local retardance of the material.³⁴

$$\frac{I(x)}{I_0} = \frac{1}{2} - \frac{1}{2} \cos(\delta(x) - 2\theta) \quad (2.3)$$

where I/I_0 is the relative intensity of the light measured by the camera, θ is the angle of the analyzer (with a range of ± 90 degrees) relative to its initial position perpendicular to the polarizer, and δ is the phase shift, or relative retardation, inside the cosine function. The phase shift may be expressed in nanometers of retardance (Δ) instead of degrees of relative retardation (δ) by dimensional conversion:

$$\Delta(x) = \frac{\lambda}{180^\circ} \cdot \frac{\delta(x)}{2} \quad (2.4)$$

where λ is the wavelength corresponding to the filter and paired quarter wave plate.

From equation (2.3), $\frac{I}{I_0}$ is minimized when

$$\delta = 2\theta \quad (2.5)$$

as shown by Jessop and is derived fully in section 1.3.⁶⁰ This solution provides the conversion factor between analyzer angle and relative retardation. A complete derivation for equation (2.3) has been performed by Mori and Tomita for a cylinder, the fiber geometry and is also provided in Appendix A.⁴² Alternatively, if a flat plate of glass with a uniform stress were examined in this manner, a single relative retardation value of δ would exist that corresponds to the analyzer angle θ at which the measured intensity is minimized. The only difference in the case of a fiber is the retardance is now affected by the difference in path length (fiber geometry) and the change in stress through that path (in this case, surface compression and interior tension). Figure 2.2 shows how the radial position of the fiber can affect the measured retardation, as each x position produces a corresponding δ value, depending on the sum of tensile and compressive stresses through the fiber cross section at points of constant x .

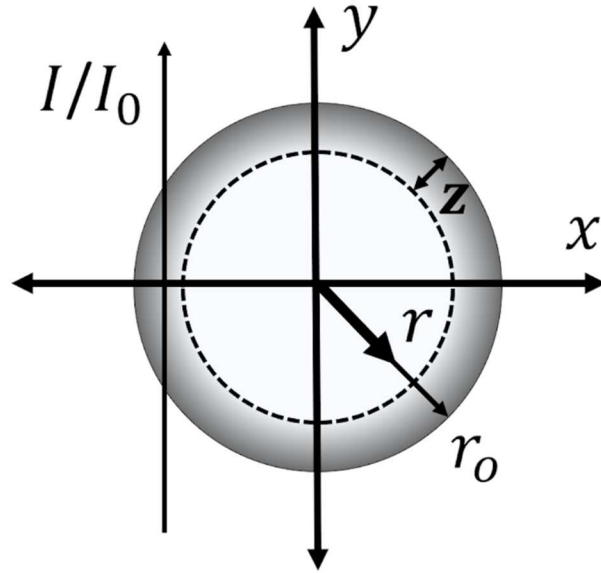


Figure 2.2. Schematic of fiber geometry in relation to incoming microscope light as described in equation (2.3). Coordinates as defined here are used throughout the work when discussing the fiber cross section. I/I_0 is the relative intensity of light as measured by the microscope camera, x and y are the horizontal and vertical directions in the fiber cross section, r is an interior radial position in the fiber, $r_0 = 62.5 \mu m$ is the radius of the fiber, and z is the characteristic depth of surface stress relaxation.

The relative intensity profile of the fiber was measured as it varied across several acquired images using a second-order polynomial least squares fit to estimate the minimum intensity angle θ to a greater accuracy than the measurement interval of 0.2 ± 0.05 degrees. The minimum intensity as described in equation (2.3) was determined at each pixel of the profile as a function of θ . Thus, the minimum intensity angle could be mapped to its x position on the fiber. Relative retardation δ was calculated using equation (2.3) at every point, then converted to retardance using equation (2.4). The retardance measurement error depends mainly on the accuracy of the analyzer rotation, which is performed by hand using 0.1-degree Vernier marks. Error in measurement is conservatively estimated to be about half of the increment, corresponding to a

retardance error of about 0.15 nm based on equation (2.4). The measurement error and spatial resolution are used as the error bounds for the figures in this work, as demonstrated in figure 2.7(b), the only figure in which the error is noticeably larger than the data points. This procedure can produce retardance measurements at every point captured by the microscope, allowing for both x position profiles as well as full two-dimensional retardance plots (figure 2.3). The resulting retardance profiles were then fit to the proposed model for retardance from surface stress relaxation (see section 2.5).

In order to confirm the trend of increasing surface stress with increasing applied load during strengthening by surface stress relaxation at low temperatures, fibers were heated to 200°C for 60 seconds in air while under a tensile load ranging from 0 to 2.0 GPa. Fibers annealed at 1200 °C for 1 hour then furnace cooled were found to have negligible retardance. Additionally, some as-received fibers were progressively etched by immersion in a 48% HF solution. Etching took place over various lengths of time (20 seconds to 6 minutes) to remove between 0.5 and 4.0 μm of the surface layer. The retardance of the processed fibers were then compared to the as-received fibers, which consisted of evaluating the values of the effective depth, z , and the estimated compressive stress at the fiber surface via the developed model.

2.2 Results

The average measured retardance for as-received silica glass fibers were obtained (figure 2.3). Both the birefringence photograph and the measured retardance profile are shown. The measured retardance was compared with the curves generated from the surface stress relaxation model shown in figure 2.9 and equation (2.17) in section 2.5. In figure 2.9, residual stress profiles

produced by surface stress relaxation are shown using the applied tensile stress, σ_{applied} , and the surface relaxed layer thickness, z , as parameters. The measured retardation profile shown in figure 2.3 was compared with the best fit theoretical model. By fitting the proposed model to the measured data and the applied stress while using a literature value for the stress optic coefficient C (3.19 Brewster, $[10^{-6} \text{ MPa}^{-1}]$),³⁵ estimates of this z value (μm) and σ_{applied} were selected to obtain the best fit, especially in the fiber surface region. The resultant curves were compared to the measured data as shown in figure 2.4.

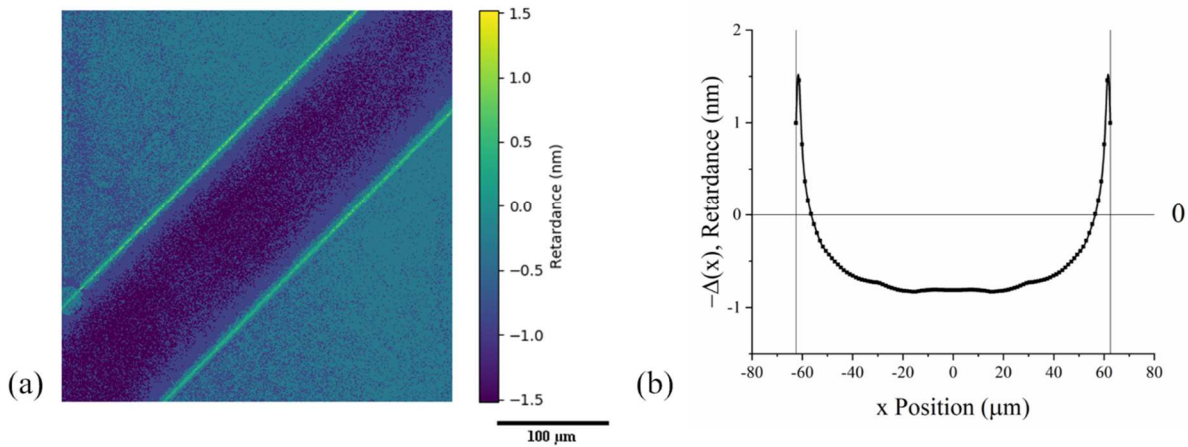


Figure 2.3. (a) Color map of as-received fiber retardance created using the same process as the profile measurement extended to the full microscope field of view. (b) measured retardance profile of as-received fiber, with fiber surface x position and the zero point of retardance indicated in vertical and horizontal guidelines, respectively. Points are the measured data while the line is a guide to the eye.

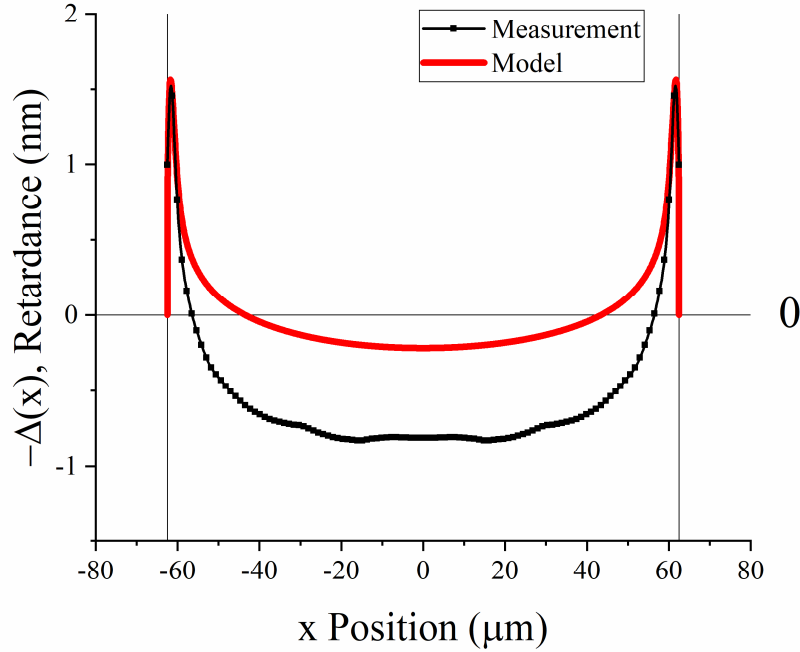


Figure 2.4. Model fit of as-received fiber retardance measurement, showing excess of internal uniform “tensile stress.” As there is no force balance to account for this tensile stress, it is more proper to discuss it as a plastic strain, likely resulting from the fiber drawing process.

The general features of the measured retardance of these fibers agreed with the predicted values using the surface stress relaxation model, both exhibiting high compressive stresses on the surface of the fibers with the shallower tensile stress zone observed in the middle part of the fibers. However, the details of the measured and predicted curves showed some systematic difference in the interior of the fiber. The balance of forces within the fiber predicts that the sum of the retardation from residual stresses of the fiber should be zero, with the total integrated compressive stress (area above the zero retardance line) cancelling the total integrated tensile stress (area below the zero line). This is explained further in Appendix B. The measurement, however, appears to have a greater contribution of “tensile stress” near the center of the fiber (below the zero retardance line) equivalent to ~5-20 MPa. The effect is consistent across

samples. The extra retardance greatly surpasses the error of the measurement (± 0.15 nm) near the center of the fiber, while it approaches the error range near the surface. This extra “tensile stress” appears to be related to an anisotropic structure due to previous uniaxial stress application.^{36, 37}

The model parameters were first fit to estimate the surface stress relaxation contribution followed by a correction factor k for the bulk anisotropy:

$$\Delta(x) = \int_{y_{min}=-\sqrt{r_o^2-x^2}}^{y_{max}=\sqrt{r_o^2-x^2}} C \cdot \{\sigma_{res}(x, y) + k\} dy \quad (2.6)$$

Equation (2.6) is thus a modification of equation (2.17) to include uniform structural anisotropy. The correction factor is within the integral, rendering it proportional to the fiber path length as expected.

In order to quantitatively isolate this additional component of structural anisotropy, the retardance of the silica glass fiber based upon the surface stress relaxation model was subtracted from the measured retardance. First, the measured retardance of the fiber surface was fit to the theory by adjusting the value of z and the applied stress, $\sigma_{applied}$. The residual stress is determined primarily by the applied tensile stress at the treatment temperature (see section 2.5 equation (2.14)). The model prediction of the retardance due to the residual stress caused by the surface stress relaxation can thus be obtained. By subtracting the model retardance from the experimental retardance (difference of two lines in figure 2.4, the remaining experimental retardance due to structural anisotropy is shown in figure 2.5(b), together with the color map of the corresponding fiber (figure 2.5(a)). The surface residual stress due to surface stress relaxation can be eliminated at a temperature far lower than the glass transition temperature, while the birefringence due to structural anisotropy requires much higher temperature. The heat-treatment

at 650°C for 10 minutes in air is appropriate to eliminate the former while leaving the latter intact.

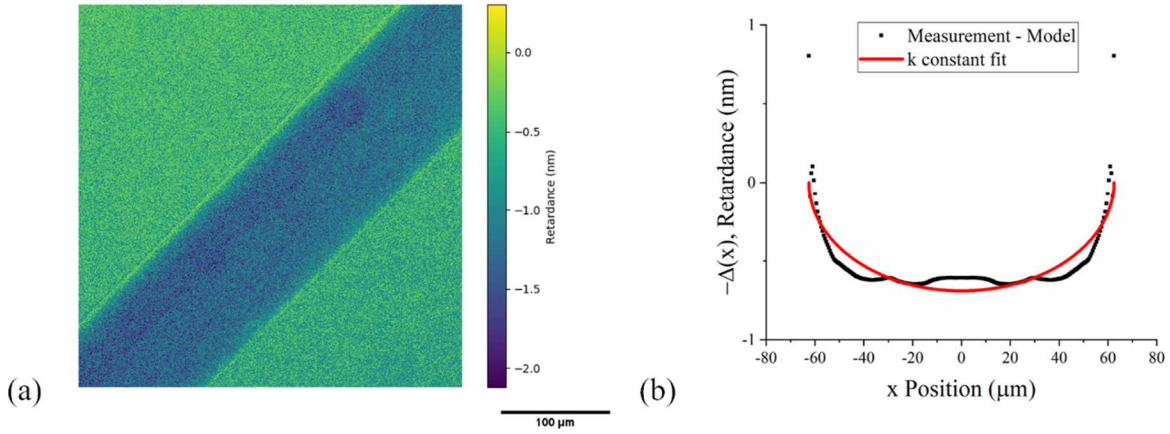


Figure 2.5. (a) A color map generated from a heat-treated fiber (650°C, 10 min at rest in lab air), revealing imbalanced apparent tensile stress in the fiber interior. (b) Corresponding retardation profile.

These analyses were conducted for all the measured retardance profiles of glass fibers, including those given low temperature tensile stress treatment. In this case, applied stress parameter, σ_{applied} , was the stress employed in the tensile stress treatment. All the parameters generated through this analysis are shown in Table 2.1. When these two contributions to the birefringence were combined, the results agree with the measured retardation as shown in figure 2.6, as expected.

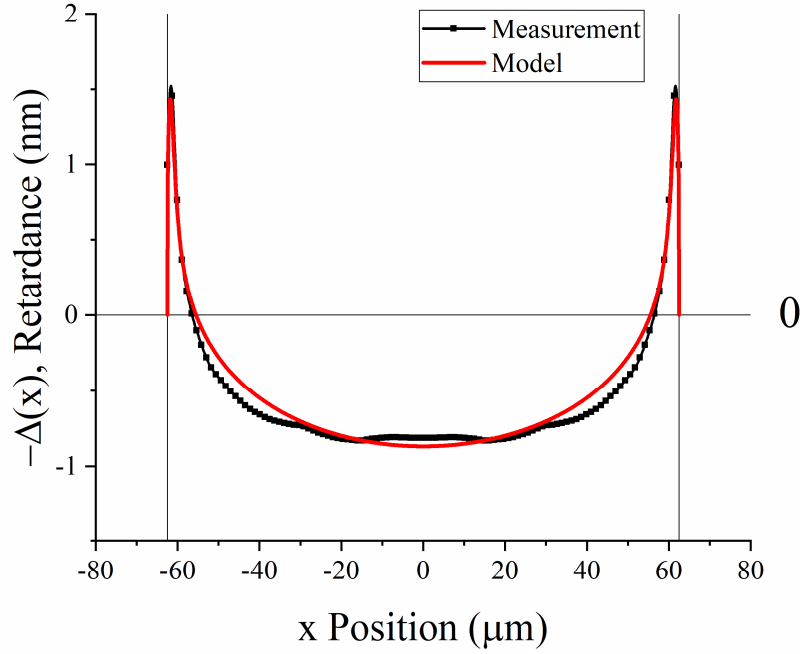


Figure 2.6. Resultant fit between the combined retardation of residual stress due to surface stress relaxation and structural anisotropy and the measurement.

Thus, the discrepancy between the experimental retardance and the model based upon surface stress relaxation can be attributed to structural anisotropy, which corresponds to “tensile stress.” The constant k , introduced to represent uniform structural anisotropies, is listed in Table 2.1 alongside the other fitting parameters as well as estimates of the surface residual stress. Stress units were used for the anisotropy to show what magnitude of tensile stress would produce a comparable retardance. The same table lists the fitting parameters for the measured retardance of fibers given strengthening treatment at a low temperature, 200°C, for 60 s in air under various tensile stresses as well as zero stress.

Table 2.1. Estimated model parameters, $\pm 95\%$ confidence bounds, and surface residual stress estimate as defined in section 2.5. Relaxation depth z , applied tensile stress, bulk structural anisotropy k , and surface residual stress estimates. All heat treatments were performed at 200°C for 60 seconds.

| Fiber Condition | z [μm] | σ_{applied} [GPa] (tensile) | k [MPa] (tensile) | $\sigma_{\text{res, surface}}$ [GPa] (compressive) |
|-----------------------------|--|---|---|--|
| As-Received (fig. 3) | 0.68 ± 0.07 | $0.45 \pm 0.4^*$ | 16.5 ± 0.2 | 0.43 ± 0.02 |
| Heat Treat, 0 GPa | 0.71 ± 0.09 | $0.29 \pm 0.15^*$ | 17.0 ± 0.2 | 0.27 ± 0.02 |
| 0.5 GPa | 0.47 ± 0.07 | 0.5 | 19.6 ± 0.2 | 0.47 ± 0.02 |
| 1.0 GPa | 0.29 ± 0.02 | 1.0 | 17.9 ± 0.2 | 0.97 ± 0.02 |
| 1.5 GPa | 0.18 ± 0.01 | 1.5 | 18.3 ± 0.2 | 1.47 ± 0.02 |
| 2 GPa | 0.22 ± 0.01 | 2.0 | 16.3 ± 0.2 | 1.97 ± 0.02 |

*value estimate from fit; applied stress unknown or negligible during treatment

Figure 2.7(a) shows the collective change of birefringence profiles of silica glass fibers by the low temperature strengthening treatment and figure 2.7 (b) shows, in magnified scales, a part of figure 2.7(a) indicating the detailed change of surface compressive stress profiles. These results show that surface stress profiles are sensitive to low temperature (200°C) tensile stress treatment conducted for a short time (60 s in air), supporting that the observed surface stress is originated from the surface stress relaxation during heat treatment: relaxation which in turn enables the elastic response during unloading of applied stress to produce surface compression. The surface compressive stress decreased under low tensile stress, while it increases under higher tensile stress. This is reasonable since the surface compressive residual stress produced is nearly equal to the applied tensile stress^{10, 11}. On the other hand, the change of the depth z of the surface residual stress due to surface stress relaxation is known to increase with the square root of the treatment time. There is an apparent trend of decreasing relaxation depth with increasing applied stress. Despite being near the resolution limitations of the measurement, the fitting error for this

trend (about 10%) is lower than the trend itself. This may merit further investigation involving longer heat treat times to determine if the same trend is also observed for larger values of z .

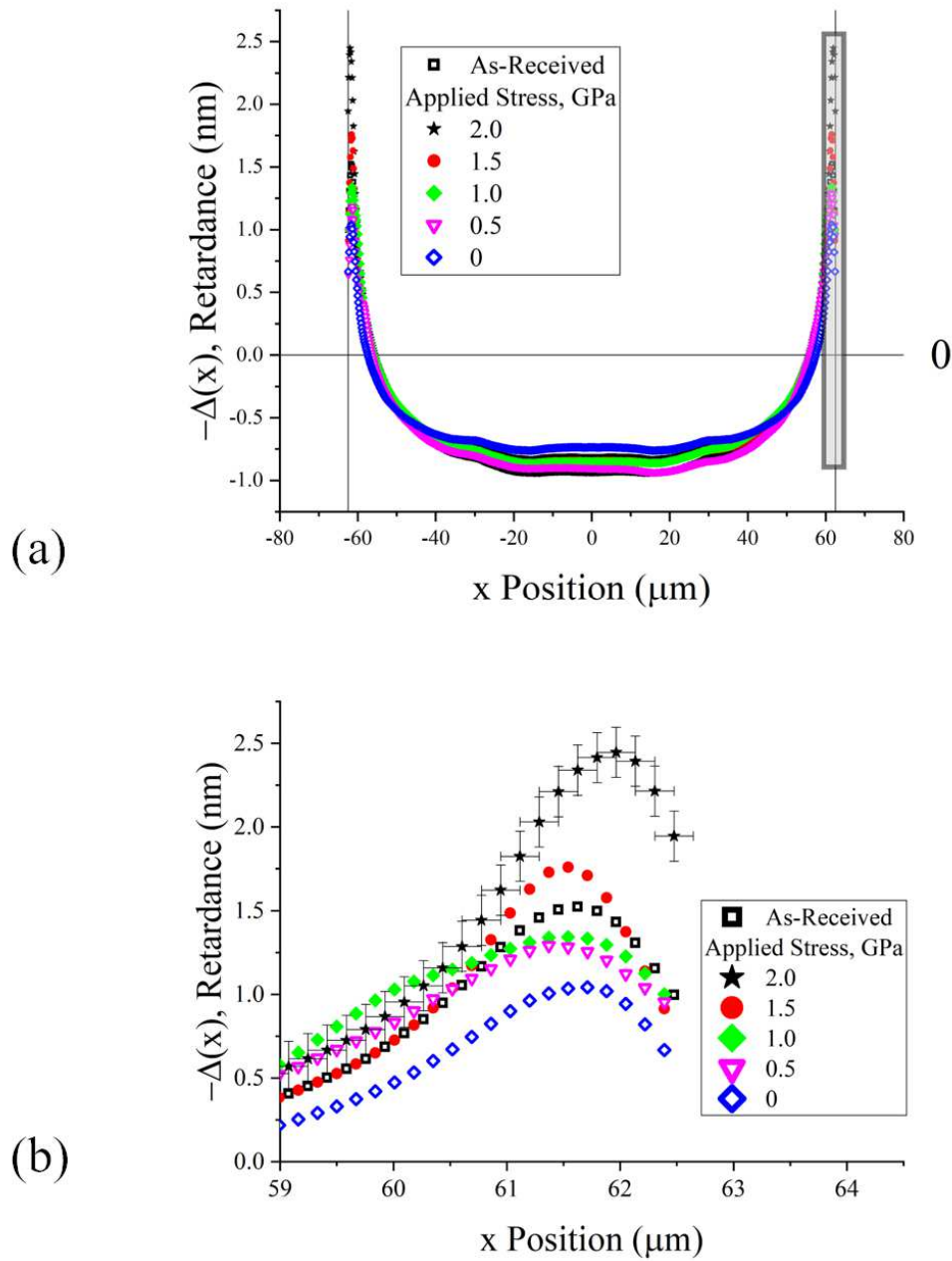


Figure 2.7. (a) Progressive strengthening via surface stress relaxation using progressively higher applied stress during heat treatment at 200°C for 60 seconds and (b) an enlarged region of interest as indicated in (a), with error bars on the highest curve representative of those on each curve. Note that the peak height increases systematically with increasing applied stress during heat treatment. The drop in retardance near the fiber surface is due to the measurement being over an increasingly short path length. In reality, the stress per path length increases significantly at the surface.

The compressive stress peaks present in the as-received fiber must be the result of a surface stress relaxation phenomenon, as the peaks are significantly decreased proportional to progressive etching (see figure 2.8), while the retardance in the interior of the fiber was affected much less so. This surface etching of the sample accentuates the imbalance between the surface compressive stress and the interior tensile stress and demonstrate the presence of interior structural anisotropy. With the removal of surface compression, much of the interior structural anisotropy-originated “tension” remains. Here, the observed fluctuation of the retardance curves in figure 2.8(b) may be due to the magnified scale of retardance with the corresponding magnification of error range. On the other hand, since this fluctuation appears to be symmetric with respect to the central fiber axis, there may be a small fluctuation of structural anisotropy.

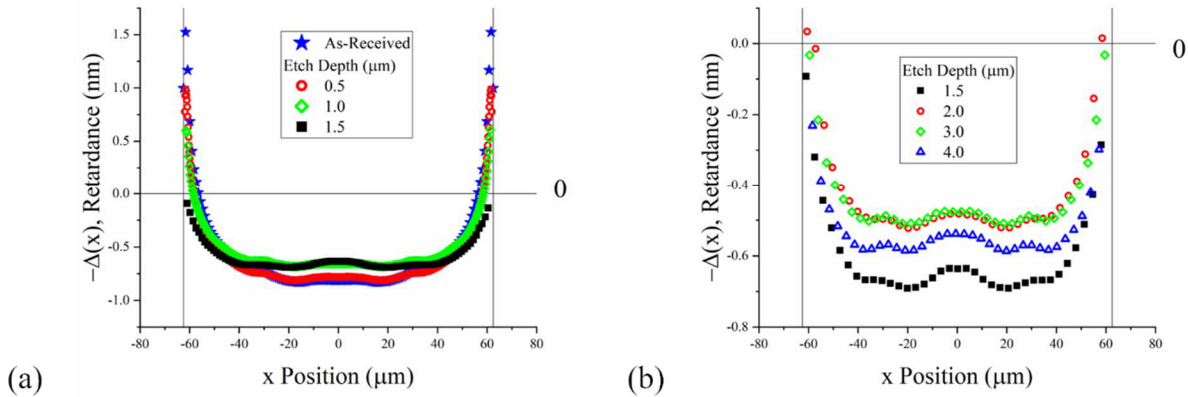


Figure 2.8. Progressive surface etching, with retardance zero point and fiber surface indicated with thin guidelines. (a) Surface compression peaks drop with etching, leaving a slightly smaller remnant retardance. (b) Further etching past 1.5 μm results in little change to bulk retardance, implying it is a result of an inelastic strain, as only apparent tensile stress remains. Note that the scale of y axis of (b) is magnified by about three times compared with (a).

2.3 Discussion

The measured retardance of as-received silica glass fibers agrees with the surface stress relaxation model well, except for a finite deviation from the theory which appears to be a nearly uniform structural anisotropy in the fiber. This deviation in the interior of fibers likely resulted from structural anisotropy created at high temperature, as the low temperature tensile stress treatment at 200°C for 60 s in air appears to have little effect. This is seen in the magnitude of the correction factor k in Table 1.1, which seems to be constant and independent of the low temperature strengthening treatment, approximately 17.6 ± 1.3 MPa. This excess retardance corresponding to “tensile stress” cannot be a result of residual stress, as there is no corresponding compressive stress to balance the forces. Because this interior retardance is nearly constant throughout the low temperature strengthening heat treatments, the retardance is a result of bulk structural anisotropy, which requires higher temperatures or longer heat-treatment times to be significantly affected and is clearly separate from the surface stress relaxation mechanism.^{9, 47}

Although the anisotropy can be fit alongside the compressive and tensile stresses within the fiber using the same stress optic coefficient, as is done in equation (2.6), this does not imply the stress optic coefficient is necessarily identical for both contributions. More work would be necessary to determine if the stress optic coefficient itself is sensitive to the fiber drawing conditions, although this is unlikely. Others have found that in as-received single-mode fibers containing a core with a doped surface layer, the stress optic coefficient appears constant through the cross section.⁶³

The obtained k values in Table 2.1 are nearly constant, independent of the low temperature strengthening process, indicating that the structural anisotropy represented by k was unaffected by the change of residual stress. This constant value of k supports the notion that structural anisotropy is a bulk phenomenon which was produced during the fiber drawing process at higher temperatures. The low temperature heat-treatments are unable to affect the structural anisotropy in the 60 s heat-treatment since they take place so far below T_g , where bulk structural relaxation occurs readily.

Similarly, progressive etching results in a decrease and ultimately a removal of surface compressive stress. The interior “tensile stress” retardance decreases to a lesser degree by the etching process but does not vanish with the disappearance in surface compression. This also seems to suggest a bulk retardance resulting from structural alignment due to the fiber drawing process and not simply a compensating tensile stress for the surface compression. A similar structural anisotropy was observed in silica glass subjected to uniaxial stresses, both compressive stress and tensile stress.^{64, 65} Sato et al.⁶⁴ observed a shift of first sharp diffraction peak (FSDP) position of x-rays, a measure of the intermediate order in glass corresponding to the arrangement of tetrahedral units, in silica glass subjected to uniaxial compressive stress. This shift remained after the compressive stress was removed. Furthermore, the position of the FSDP was a function of the sample orientation with respect to the uniaxial stress, meaning that the shift was not a result of simple uniform densification, but was in fact anisotropic.

Earlier, Murach and Bruckner⁴⁸ observed frozen-in birefringence in fine silica fibers with diameters ranging from ~ 10 – $60\ \mu\text{m}$ of three different silica glasses drawn at high temperatures

~2350–2430°C. They measured the magnitude of birefringence of the bundle of these fibers and found a greater birefringence in the fiber when the silica glass fibers were drawn under a higher stress or when the fibers had a higher water content.⁴⁸

Observed birefringence in fibers is often attributed to frozen-in viscoelasticity.⁶⁶ It is known that the second-order delayed elastic response in a viscoelastic material caused by inhomogeneity is absent when a glass has only one relaxation time at a given temperature. This occurs when the KWW exponent, β , of relaxation is unity.⁶⁷ High purity silica glasses, including silica glass containing Cl, has a single relaxation time as can be seen from the absence of memory effect.^{68, 69} For these glasses, there can be no frozen viscoelasticity. When silica glasses contain increasing impurity contents of water or fluorine, glasses exhibited greater memory effect, and thus a widening distribution of relaxation times.⁶⁸ This distribution of relaxation times is thought to correspond to local compositional fluctuations, which could align under stress to produce the observed structural anisotropy.⁷⁰

Glasses containing water impurities exhibited large internal friction or viscoelasticity: on a per mole basis, in both phosphate¹⁰ and silicate glasses¹¹, water in glass exhibited an internal friction loss peak, which is greater in magnitude than those of alkali or alkaline ions in the same glass by a factor of 100. The previously mentioned increased birefringence with increased OH content by Murach and Bruckner⁴⁸ suggests greater frozen viscoelasticity (or internal friction peak) due to OH impurity for silica glass as well. In the method of birefringence measurement employed by Murach and Bruckner⁴⁸, who analyzed a bundle of several fibers to produce an average value, residual stress contribution from surface stress relaxation would not be detected due to the

cancellation of compressive stress with tensile stress. Furthermore, their birefringence data do not extrapolate to zero when the water impurity content was extrapolated to zero. This is probably due to the entry of the additional water impurity into silica glass fibers during the fiber drawing process, since they used hydrogen-oxygen burner.^{71, 72}

It is thus suggested that the observed structural anisotropy in the fibers employed in the present study, Suprasil II, which contains 1200 ppm OH, can be attributed to the water impurity. The large effect of small water content in silica glasses has been attributed to concentration fluctuation of SiO₂-H₂O system.⁷⁰

2.4 Conclusion

Birefringence observed at the surface of silica glass fibers can be explained by surface stress relaxation. The fiber undergoes fast surface stress relaxation enhanced by water vapor in air during the fiber drawing process. Similar retardance profiles can be observed in fibers undergoing low temperature heat treatments in air under tension, resulting in retardance proportional to the applied tensile load. Removal of the fiber surface via etching results in a decrease in the observed retardance, by removal of the surface compressive stress. Remaining retardance after etching is likely the result of structural alignment from the fiber drawing process, produced by viscoelastic alignment of regions with small compositional fluctuations.

2.5 Derivation of tensile stress relaxation model

A uniform uniaxial tensile stress is imposed on the fiber either during the manufacturing process or in the lab via uniform applied stress, which is correlated to a uniform strain in the material:

$$\sigma_{applied} = E \cdot \epsilon_{applied} \quad (2.7)$$

Due to the surface stress relaxation, the originally uniform applied tensile stress, σ_{applied} , changes to a relaxed stress, σ_{relax} , with a thin surface layer of thickness z losing the stress by a diffusion-controlled process, promoted by moisture in the atmosphere:

$$\begin{aligned}\sigma_{\text{relax}}(r, z) &= \sigma_{\text{applied}} \cdot \left[1 - \text{erfc}\left(\frac{r_0 - r}{2z}\right) \right] \\ &= \sigma_{\text{applied}} \cdot \text{erf}\left(\frac{r_0 - r}{2z}\right)\end{aligned}\tag{2.8}$$

where r_0 is fiber radius, r is radial position within the fiber, and z is the characteristic relaxation depth (see figure 2.2). Note this model assumes that $z \ll r_0$ in order to approximate a planar diffusion at the fiber surface using the error function.¹³ This depth can be related to the effective diffusivity of surface stress relaxation, D , and the time of the heat treatment, t :

$$z = \sqrt{Dt}\tag{2.9}$$

With this relaxation, when the imposed axial strain is subsequently released, strain will spring back by some uniform $\Delta\epsilon_{sb}$ resulting in a residual axial stress σ_{res} as $\sigma_{\text{relax}}(r)$ is reduced by $\Delta\sigma_{sb}$:

$$\sigma_{\text{res}}(r, z) = \sigma_{\text{relax}}(r, z) - \Delta\sigma_{sb}\tag{2.10}$$

This balance is radially symmetrical about the cross section of the fiber, and must also radially integrate to zero:

$$\int (\sigma_{\text{applied}} \cdot \text{erf}\left(\frac{r_0 - r}{2z}\right) - \Delta\sigma_{sb}) dA = 0\tag{2.11}$$

Considering the radial cross section:

$$\sigma_{\text{applied}} \cdot \int_0^{r_0} \text{erf}\left(\frac{r_0 - r}{2z}\right) 2\pi r dr - \Delta\sigma_{sb} \pi r_0^2 = 0\tag{2.12}$$

Solving for $\Delta\sigma_{sb}$ and substituting into equation (2.10), residual axial stress becomes a function of radial position:

$$\sigma_{res}(r, z) = \sigma_{applied} \left\{ \operatorname{erf} \left(\frac{r_o - r}{2z} \right) - \frac{2}{r_o^2} \int_0^{r_o} \operatorname{erf} \left(\frac{r_o - r}{2z} \right) \cdot r \, dr \right\} \quad (2.13)$$

The integral has a closed-form solution resulting in the following residual stress profile:

$$\sigma_{res}(r, z) = \sigma_{applied} \cdot \left\{ \operatorname{erf} \left(\frac{r_o - r}{2z} \right) - \left(\frac{2r_o z \cdot e^{-\frac{r_o^2}{4z^2} + \sqrt{\pi} \cdot (r_o^2 + 2z^2) \cdot \operatorname{erf} \left(\frac{r_o}{2z} \right) - 4r_o z}}{\sqrt{\pi} r_o^2} \right) \right\} \quad (2.14)$$

Birefringence (and thus retardance) is linearly proportional to stress, and can be expressed as follows:

$$d\Delta = C \cdot \sigma_{res}(r, z) dy \quad (2.15)$$

where C is the stress optic coefficient dy is a differential form of the path length. Thus, referring to the coordinates of figure 2.1 (a), for any x position along the fiber profile:

$$\Delta(x) = \int_{y_{min}(x)}^{y_{max}(x)} C \cdot \sigma_{res}(r, z) dy \quad (2.16)$$

where Δ is retardance and dy gives the orientation of the path length parameter, which is expressed in the integral limits as a function of x position. $\sigma_{res}(r)$ can be converted to rectangular coordinates. The r term in equation (2.14) is simply replaced with $\sqrt{x^2 + y^2}$:

$$\Delta(x) = \int_{y_{min} = -\sqrt{r_o^2 - x^2}}^{y_{max} = \sqrt{r_o^2 - x^2}} C \cdot \sigma_{res}(x, y) dy \quad (2.17)$$

This result produces a retardance profile comparable to those expected from surface stress relaxation.¹⁰ figure 2.9 below illustrates the result of this equation using different z and $\sigma_{applied}$ values.

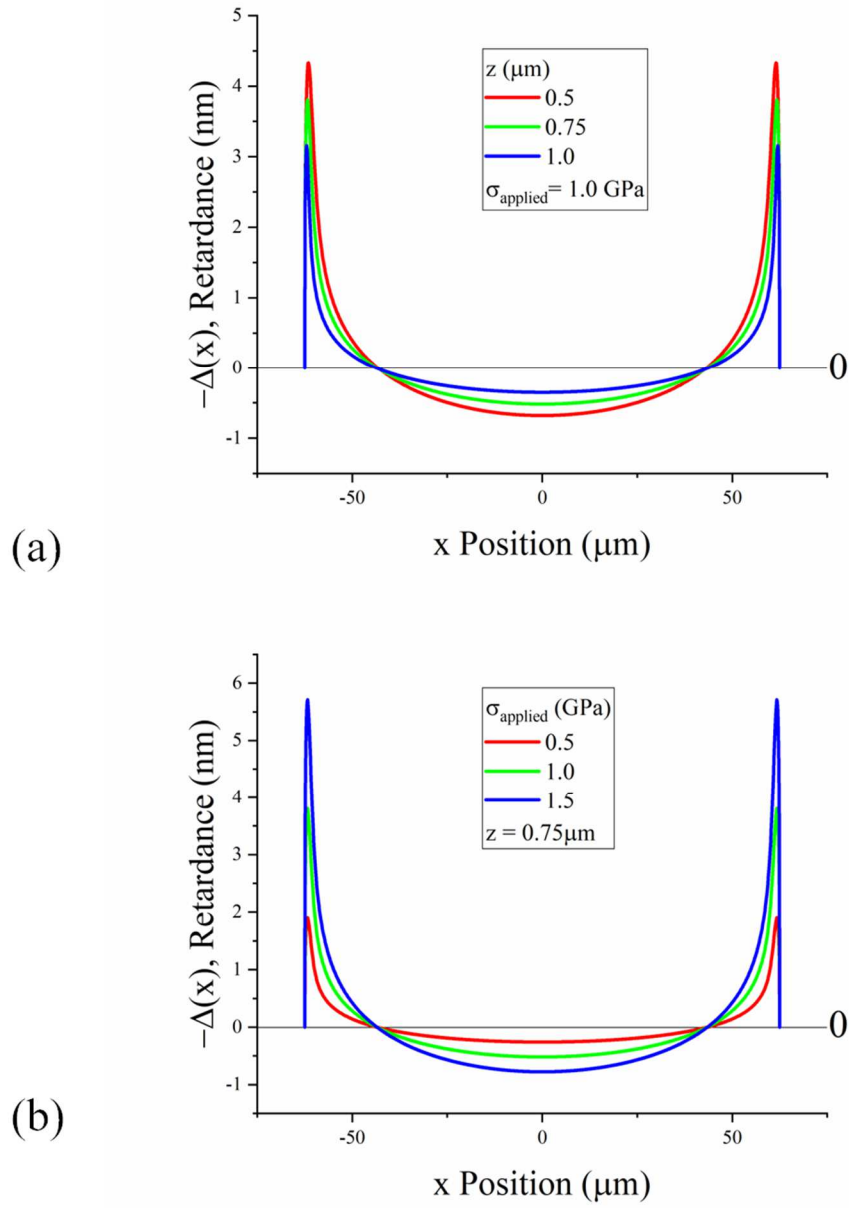


Figure 2.9. (a) Plot of retardance with variations in parameter z with $\sigma_{applied}$ fixed at 1.0 GPa (b) as well as variations in parameter $\sigma_{applied}$ with z fixed at 0.75 μm . The plots shown use the stress optic coefficient of Suprasil II.⁷³

3. RESIDUAL STRESS IN SILICA GLASS: BENDING OF FIBERS AND SHEAR STRESS RELAXATION OF RODS

Fast surface stress relaxation in silica glass has been found to occur at low temperatures in the presence of water vapor.⁵⁴ Various methods have been employed to characterize surface stress relaxation in glass fibers including IR spectroscopy,⁵⁶ fiber bending relaxation kinetics,¹² and fiber strengthening by surface stress relaxation.^{13, 54} Surface stress relaxation has been used to account for phenomena such as crack toughening by tensile stress application below the fatigue limit, region zero in the slow crack growth velocity vs. stress intensity diagram,^{55, 74} and the corresponding static fatigue limit of glass.^{14, 74} Shear stress relaxation of silica rods at low temperatures has been similarly attributed to interaction with ambient water vapor.²³

Previous calculations of the surface stress relaxation rate or residual stress in the glass surface were made from various measurable quantities of stress relaxation, such as the failure strength in bending, fiber bending residual curvature, or torque relaxation under applied shear strain.^{12, 23, 75} In all configurations, it was assumed that the relaxation advances from the sample surface in a diffusion-controlled manner with the relaxation depth given by

$$z = \sqrt{D_{SSR} \cdot t} \quad (3.1)$$

where z is the depth of 50% surface relaxation, such that full relaxation occurs at $2z$, D_{SSR} is the effective diffusivity of surface stress relaxation, and t is the time duration of heat-treatment.

Portions of this chapter previously appeared as:

Hausmann BD, Aaldenberg EM, Tomozawa M. Photoelastic confirmation of surface stress relaxation in silica glasses: Fiber bending and rod torsion. *J Am Ceram Soc.* 2021;104(7):3087–3096. <https://doi.org/10.1111/jace.17690>

Discussion of the stress relaxation rate as an effective diffusivity limited by water diffusion allows for analysis of the process kinetics, which are different from the water diffusion itself. In this work, residual stresses near the glass surface of both silica glass fibers and rods were measured through optical retardation and compared with the theoretical stress produced by fast surface stress relaxation, after the samples were heat-treated at a temperature far below the glass transition temperature in lab air while under applied strain.

Optical measurements were made using a polarized light microscope (Nikon Eclipse, LV-100 NPOL) using the S  narmont method, which has been used to measure stress profiles in optical fibers previously.^{41, 42, 61} The intensity of cross-polarized light passing through the sample and a quarter wave plate was analyzed in order to produce retardance profiles across the field of view of the microscope. Retardance can be related to the stress, σ , in glass by the stress-optic law⁷⁶:

$$\sigma = \frac{\Delta}{C \cdot y} \quad (3.2)$$

where Δ is the retardance, C is the stress-optic coefficient, and y is the path length through the material.

3.2 Fiber bending

3.2.1 Analysis of residual bending stress

Previously, surface stress relaxation kinetics were measured based on the residual curvature of fiber heat-treated in a two-point bend configuration. A simplified analysis related the difference in angle between the straight portion of the fiber tail (where no bend was applied) and the original straight fiber, Φ in radians, to the radius of curvature of the fiber¹²

$$\Phi = \frac{R_0}{R_S} \cdot \frac{\pi}{2} \quad (3.3)$$

where R_0 is the radius of curvature of the fiber during the bending stress application and R_S is the springback radius of curvature following heat-treatment when the fiber is removed from the two-point bending configuration and springback occurs. R_0 and R_S vary as a function of position along the bend, but the ratio R_0/R_S is shown theoretically to be constant at all positions along the curved portion of the fiber. A simple method for obtaining Φ has been developed previously.²¹ First, a straight fiber is placed horizontally, and a bent fiber is placed underneath the straight fiber symmetrically. The angle between the horizontal line and straight edge of the bent fiber is given by Φ . Since the residual curvature results from a stress distribution in the fiber, photoelastic analysis can be used to determine the curvature from the stress distribution.

The fiber axial stress as a function of radial position is known to be given by the following expression for a known bending radius R_0 :

$$\sigma_{applied}(r, \theta) = \frac{E \cdot r \cdot \cos \theta}{R_0} \quad (3.4)$$

where E is the Young's modulus and r and θ are the polar coordinates within the fiber (see figure 3.1). As fibers under applied stress are heated and undergo surface stress relaxation, the degree of relaxation from the surface inward, $\Delta\sigma_{relax}$, is assumed to follow a complementary error function:

$$\Delta\sigma_{relax}(r, \theta) = \frac{E \cdot r \cdot \cos \theta}{R_0} \cdot \operatorname{erfc} \left(\frac{r_0 - r}{2z} \right) \quad (3.5)$$

where r_0 is the fiber radius. The residual stress is then related to the applied stress and the relaxation ($\Delta\sigma_{relax}$) with an additional contribution from the elastic response of the fiber upon removal of applied bending ($\Delta\sigma_{spring}$):

$$\begin{aligned}
\sigma_{res}(r, \theta) &= \frac{E \cdot r \cdot \cos\theta}{R_0} - \Delta\sigma_{relax} - \Delta\sigma_{spring} \\
&= \frac{E \cdot r \cdot \cos\theta}{R_S} - \Delta\sigma_{relax}
\end{aligned} \tag{3.6}$$

where $\Delta\sigma_{spring}$ has the same form as $\sigma_{applied}$ but has a different curvature, R_S .⁵⁴ Combining equation (3.5) and equation (3.6), the residual stress can be expressed as follows:

$$\sigma_{res}(r, \theta) = E \cdot \left\{ \frac{r \cdot \cos\theta}{R_S} - \frac{r \cdot \cos\theta}{R_0} \cdot \operatorname{erfc}\left(\frac{r_0 - r}{2z}\right) \right\} \tag{3.7}$$

The cross-section of a silica fiber with radius r_0 is schematically shown in figure 3.1, demonstrating this theoretical residual stress following heat treatment under bending stress. In rectangular coordinates, this can be rewritten as

$$\sigma_{res}(x, y) = E \cdot \left\{ \frac{x}{R_S} - \frac{x}{R_0} \cdot \operatorname{erfc}\left(\frac{r_0 - \sqrt{x^2 + y^2}}{2z}\right) \right\} \tag{3.8}$$

which allows for the coordinates of the theory to align with the measured data, where fiber radial position x is parallel to the stage, as shown in figure 3.1.

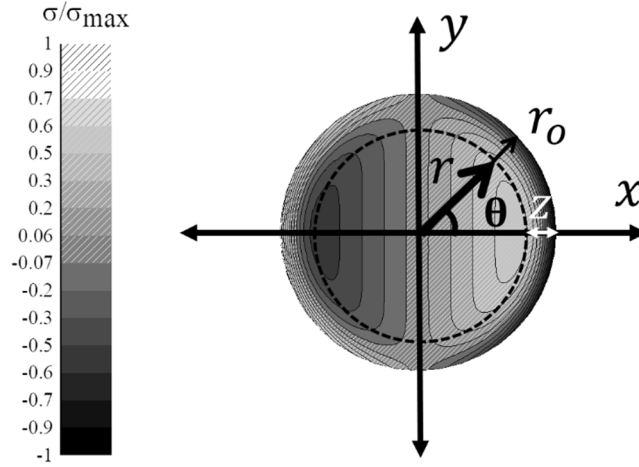


Figure 3.1. Schematic of the residual stress distribution in a fiber cross-section with radius r_0 following removal of the applied bend after relaxation in a two-point bending configuration. The relaxation depth is denoted by z . At the apex of the bend, the maximum tensile strain was applied at position $(x = r_0, y = 0)$ during bending and the maximum compressive strain was applied at position $(x = -r_0, y = 0)$. This results in a residual stress in the fiber axial direction of opposite sign of the applied strain, compressive stress at $(x = r_0, y = 0)$ and tensile at $(x = -r_0, y = 0)$ for example. Polarized light was passed through the sample in the y direction in order to measure the stress distribution in the fiber as a function of x .

Experimentally, the fiber geometry and the applied bending curvature are known. Thus, as currently written, equation (3.8) requires the measurement of the residual curvature R_S and relaxation depth z to give the residual stress as a function of x position. The residual curvature however is necessarily dependent on the experimental conditions and relaxation depth, because the bending moment of the fiber must be equal to zero under zero applied bending strain⁵⁴:

$$M = 0 = \int_0^{2\pi} \int_0^{r_0} \left\{ E \frac{r}{R_S} \cos\theta - E \frac{r}{R_0} \cos\theta \cdot \operatorname{erfc} \left[\frac{r_0 - r}{2z} \right] \right\} \cdot r^2 \cos\theta \, dr \, d\theta \quad (3.9)$$

where M is the bending moment of the fiber. This integral has been evaluated for the case when $z \ll r_0$ to give the simplified form⁵⁴:

$$M = 0 = \pi E \left[\frac{r_0^4}{4R_S} - \frac{1}{R_0} \left(\frac{2}{\sqrt{\pi}} r_0^3 z \right) \right] \quad (3.10)$$

which gives by inspection:

$$\frac{r_0}{4R_s} = \frac{2z}{\sqrt{\pi}R_0} \quad (3.11)$$

thus allowing for the approximation:

$$R_s = \frac{\sqrt{\pi}R_0r_0}{8z} \approx \frac{R_0r_0}{4.51z} \quad (3.12)$$

Equation (3.8) can therefore be rewritten in terms of z , r_0 , and R_0 alone, eliminating R_s by substitution with equation (3.12):

$$\sigma_{res}(x, y) = E \cdot \left\{ \frac{4.51 \cdot z \cdot x}{R_0 \cdot r_0} - \frac{x}{R_0} \cdot \operatorname{erfc} \left(\frac{r_0 - \sqrt{x^2 + y^2}}{2z} \right) \right\} \quad (3.13)$$

A residual stress profile can thus be fit to find the parameter z for $z \ll r_0$ since the applied radius of curvature R_0 and the fiber radius r_0 are known. Figure 3.2 shows the initial stress distribution in the center of the fiber along the y direction (the case when the fiber is in focus on the microscope) when the bending moment is applied, the stress after relaxation has occurred to a depth z , and the residual stress following heat treatment and removal from the initial bend.

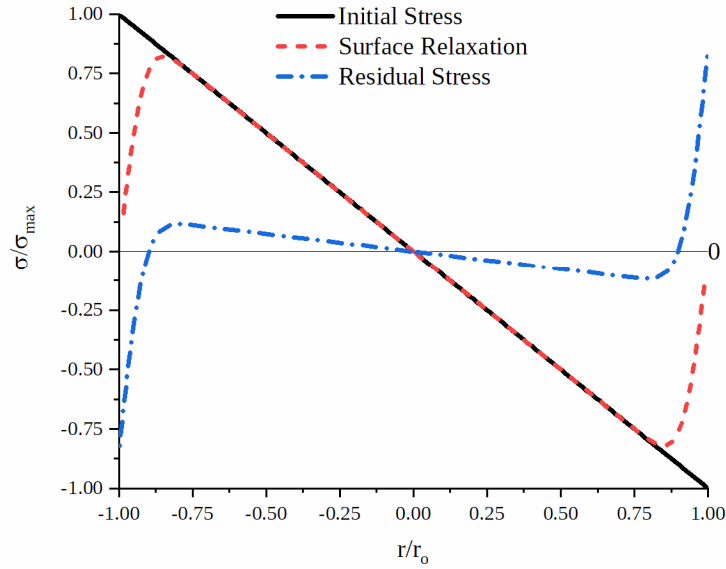


Figure 3.2. Plot of the change in stress profile following surface stress relaxation in bending as developed previously by Lezzi et al.²¹ A constant bending moment is applied resulting in an initial stress profile (equation (3.4)). Upon heat-treatment in the presence of water, surface stress relaxation takes place (equation (3.5)). Here, relaxation is assumed to follow an error function profile with all stress relaxed at $x = r_0$. After removing the applied bending, the residual stress in the near-surface which was previously under compression is now in tension and vice versa (equations (3.8) and (3.13)). The interior stress, however, retains the same sign as the initial stress. The relaxation depth $z/r_0 = 0.05$ is over-exaggerated for visibility.

3.2.2 Experimental procedure

Suprasil II silica fibers (Heraeus Inc.) were characterized following fiber bending relaxation. The fiber contains 1200 wt. ppm OH and 0.1 wt. ppm Al, with all other impurities less than 0.05 wt. ppm. The Young's modulus of the fiber is 72.0 GPa and the stress optic coefficient is 3.19 Brewsters.⁷³ The glass-transition temperature was estimated to be $\sim 952^\circ\text{C}$ - 1006°C .^{58, 59} Fibers with a diameter, $2r_0$, of 125 μm were placed into a static two-point bending configuration using 15, 20, and 22 mm inner diameter silica glass tubes. This configuration gave an initial maximum bending stress of 728, 545, and 495 MPa, respectively, at the apex of the bend.⁷⁵ Fibers were

then heat-treated in lab air at 300-500°C for various lengths of time, up to 17 days. The partial pressure of water in the lab air was estimated to be about 7 torr, or 1kPa as assumed in past fiber bending experiments. Following relaxation, the fibers that were removed from the tubes exhibited a residual bend from the surface stress relaxation during heat treatment.

Stress birefringence measurement of silica glass fibers was described in detail in previous work.⁷⁷ In the present experiment also, fibers were placed upon slides in index-matching fluids and the retardance integrated along the x direction of the entire fiber cross section shown in figure 3.1 was determined. Polarized light was passed through the sample along the y-axis in order to measure this retardance in order to calculate the residual stress in the fiber axial direction. Following bending relaxation and subsequent removal from this configuration, the residual stress distribution is expected to follow equation (3.13).

This theoretical stress distribution can be converted to retardance as a function of position x by application of equation (3.2)⁷⁷:

$$\Delta(x) = \int_{y_{min}=-\sqrt{r_o^2-x^2}}^{y_{max}=\sqrt{r_o^2-x^2}} C \cdot \{\sigma_{res}(x, y)\} dy \quad (3.14)$$

where y_{min} and y_{max} determine the sample thickness at position x . To avoid including the residual stress present from the fiber drawing process in this analysis, the retardance profile of an as-received fiber was subtracted from the retardance measured following relaxation. Retardance profiles presented in this work are given with negative retardance plotted in the positive y direction, in order to match previous work.⁷⁷ Retardance was fit to equation (3.13) and (3.14) using only z as the fitting parameter, as C , E , R_0 , and r_o are known. The z parameter was substituted into equation (3.1) and fit as a function of heat treatment time in order to calculate an

effective diffusivity of surface stress relaxation. For comparison, Φ was also measured.

Substitution of equation (3.10) into equation (3.3) gives Φ in terms of z , which allows for direct comparison.⁵⁴

$$\Phi = \frac{R_o}{R_s} \cdot \frac{\pi}{2} = \frac{4.51\pi z}{2r_0} \quad (3.15)$$

3.2.3 Results

Bending relaxation of silica glass fibers resulted in the expected stress distribution predicted by Lezzi et al¹² when retardance of the as-received fiber is removed (see figure 3.3).⁷⁷

Several retardance profiles were fit to equation (3.14). Examples of the fit are shown in figure 3.4 and figure 3.5.

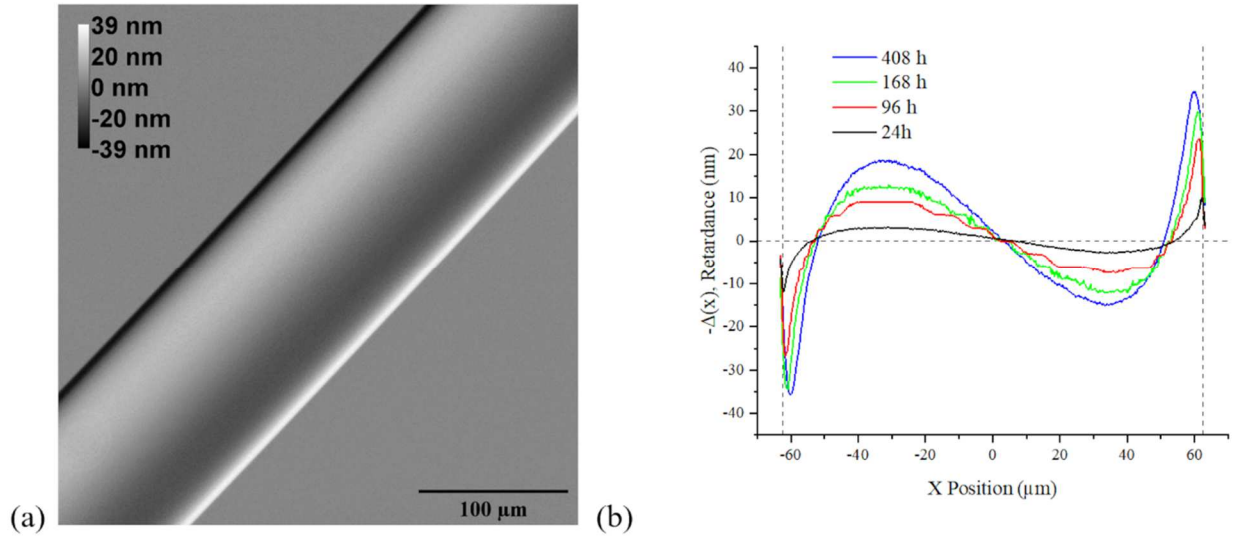
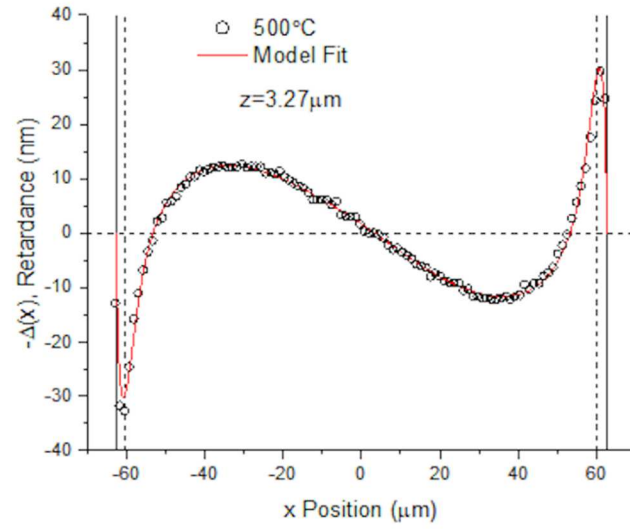
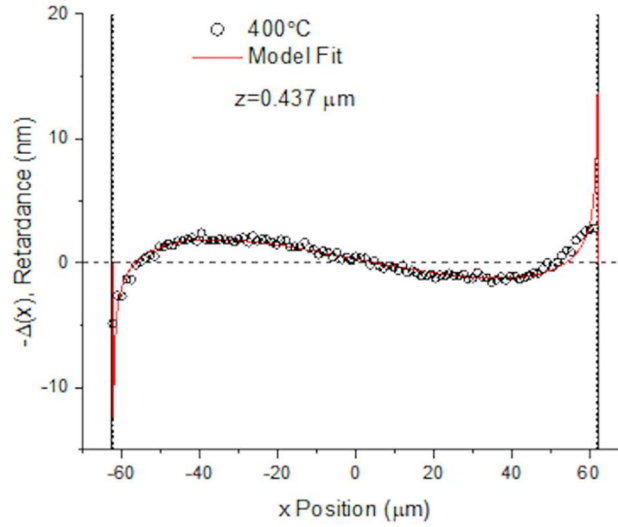


Figure 3.3. (a) Example of a measured fiber bending retardance map of a 500°C, 408 h treatment as measured with retardance profile. The positive y direction corresponds to negative retardance and thus residual compressive stress. (b) Theory fit following heat treatments at 500°C from 24 to 408 hours under a maximum bending stress of 728 MPa. Fiber edges are indicated by vertical lines.



(a)



(b)

Figure 3.4. Fiber bending retardance data fit using equation (3.14). Curves are shown to fit to the optical retardance measurements for samples heat treated at (a) 500°C and (b) 400°C with a maximum bending stress of 728 MPa for 408 hours. In this case, the tensile and compressive stress fits of depth z do not appear to differ significantly. The fiber surface is indicated by solid vertical lines, with z depth indicated by dashed lines.

Retardance corresponding to compressive stress is positive.

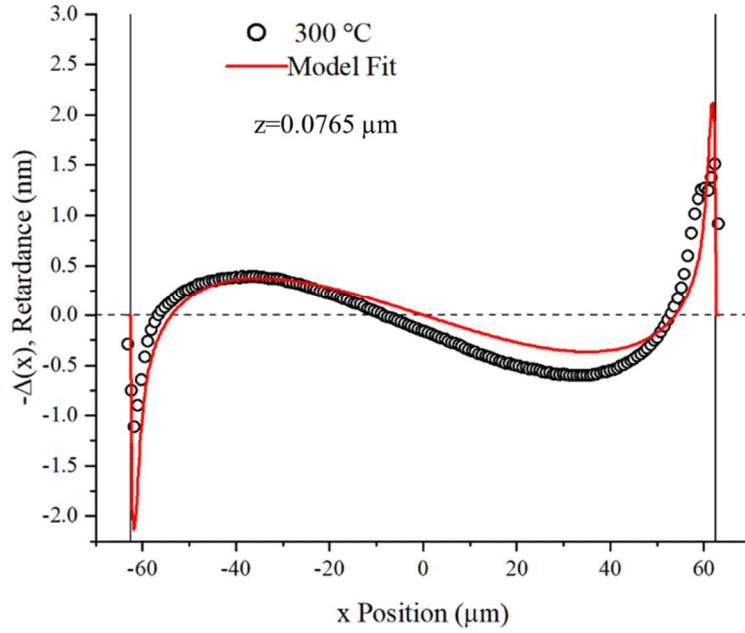


Figure 3.5. Fiber bending retardance profile for sample heat treated at 300°C under a maximum bending stress of 728 MPa for 168 hours. The slight deviation between peak widths for the side which was heated under compression (left) versus tension (right) is apparent at this lower temperature.

The diffusivity of surface stress relaxation has been calculated through a linear fit of z^2 as a function of t at a given temperature. These diffusivities were organized into an Arrhenius plot shown in figure 3.6, which were found to follow to a single line with an activation energy of 122 ± 8 kJ/mol.

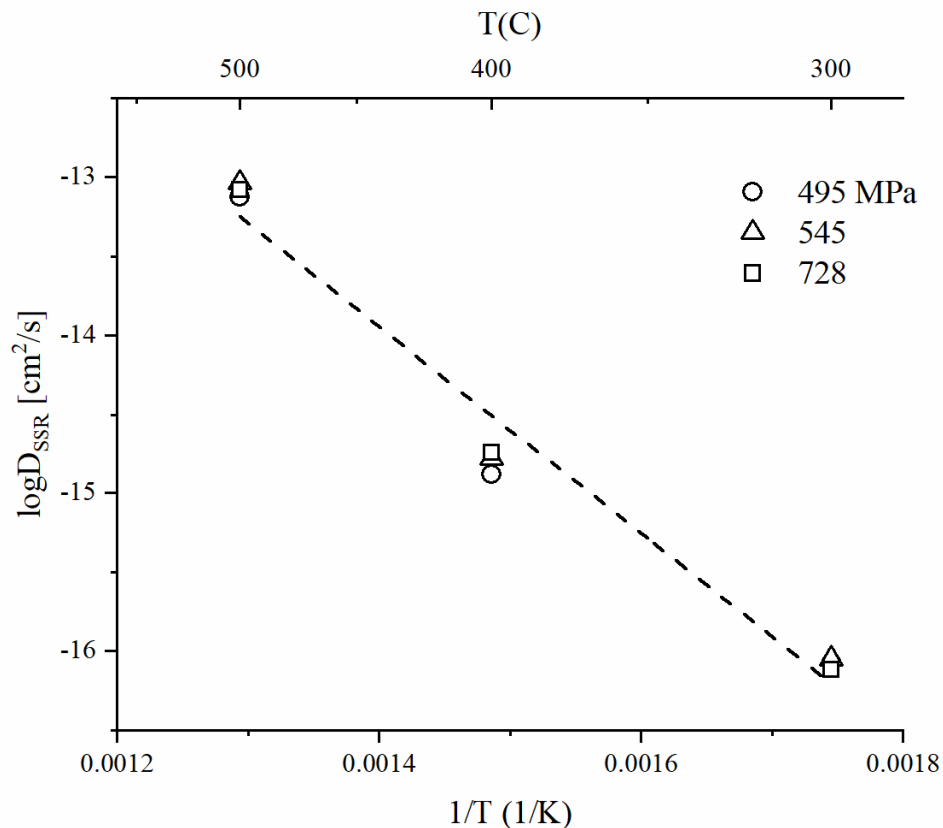


Figure 3.6. Arrhenius plot of bending relaxation diffusivity for various stress values. Line indicates activation energy of 122±8 kJ/mol.

Diffusivity was also calculated using the fiber bending angle and compared to the values obtained by retardance measurement in this work, as well as previously obtained values⁷⁸ from bending angle measurements (see figure 3.7). New calculations of diffusivity by bending angle resulted in an activation energy calculation of 109±14 kJ/mol. The diffusivity values calculated by the retardance method were consistently lower than those calculated by the bending angle measurement method for the same samples (see Table 3.1).

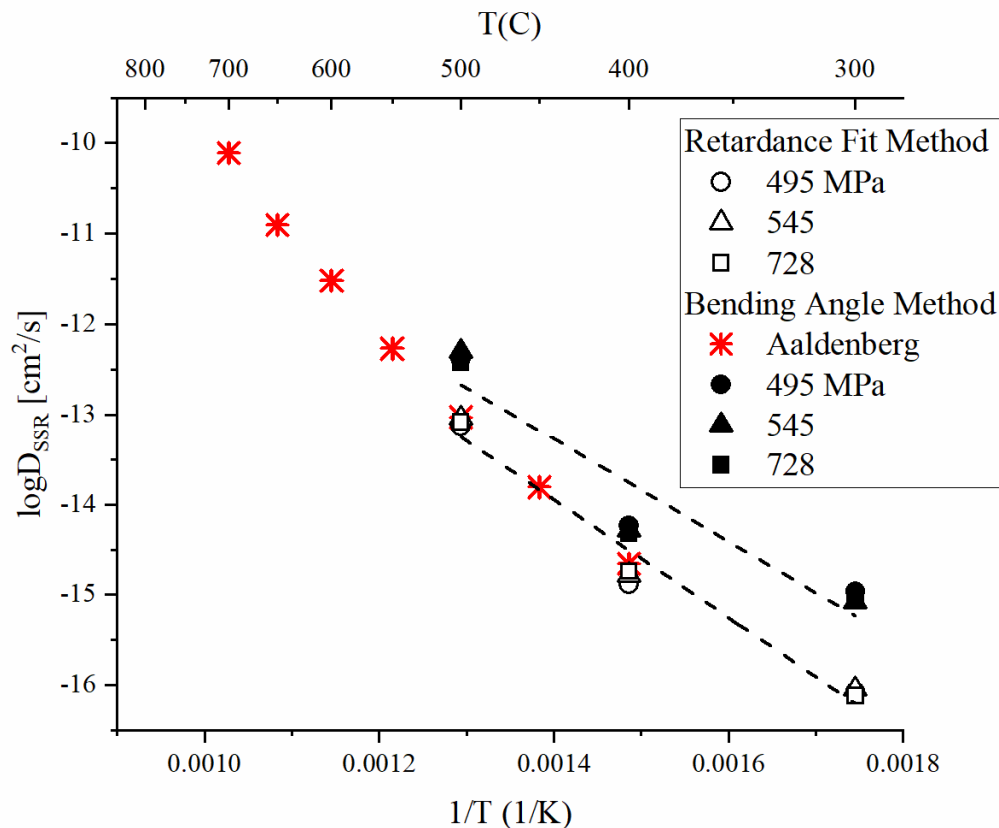


Figure 3.7. Arrhenius plot comparing diffusivity measurement methods as applied in this work and previous work.⁷⁸ The current work's measurements are differentiated by applied stress. Dashed lines indicate the activation energy fit for retardance and bending angle diffusivity calculations (122 ± 8 and 109 ± 14 kJ/mol, respectively). In all cases, diffusivity calculated by bending angle measurement was slightly higher than the corresponding retardance measurement calculation.

Table 3.1. Diffusivity of bending stress relaxation, measured by bending angle Φ and retardance fit of z .

| Temperature [°C] | Applied Stress [MPa] | D_{SSR} , Retardance [cm ² /sec] | D_{SSR} , Bending Angle [cm ² /sec] |
|---------------------|-------------------------|--|---|
| 300 | ±495 | 7.67×10^{-17} | 9.85×10^{-16} |
| | ±545 | 8.97×10^{-17} | 8.34×10^{-16} |
| | ±728 | 8.49×10^{-17} | 1.10×10^{-15} |
| 400 | ±495 | 1.81×10^{-15} | 4.78×10^{-15} |
| | ±545 | 1.66×10^{-15} | 5.25×10^{-15} |
| | ±728 | 1.32×10^{-15} | 5.85×10^{-15} |
| 500 | ±495 | 8.29×10^{-14} | 3.74×10^{-13} |
| | ±545 | 9.24×10^{-14} | 5.01×10^{-13} |
| | ±728 | 7.48×10^{-14} | 4.17×10^{-13} |

Figure 3.8 compares the surface stress relaxation diffusion coefficients determined by the two different methods. The two methods give diffusivity within 10 percent of each other, although fiber bending angle measurement consistently resulted in a higher diffusivity calculation.

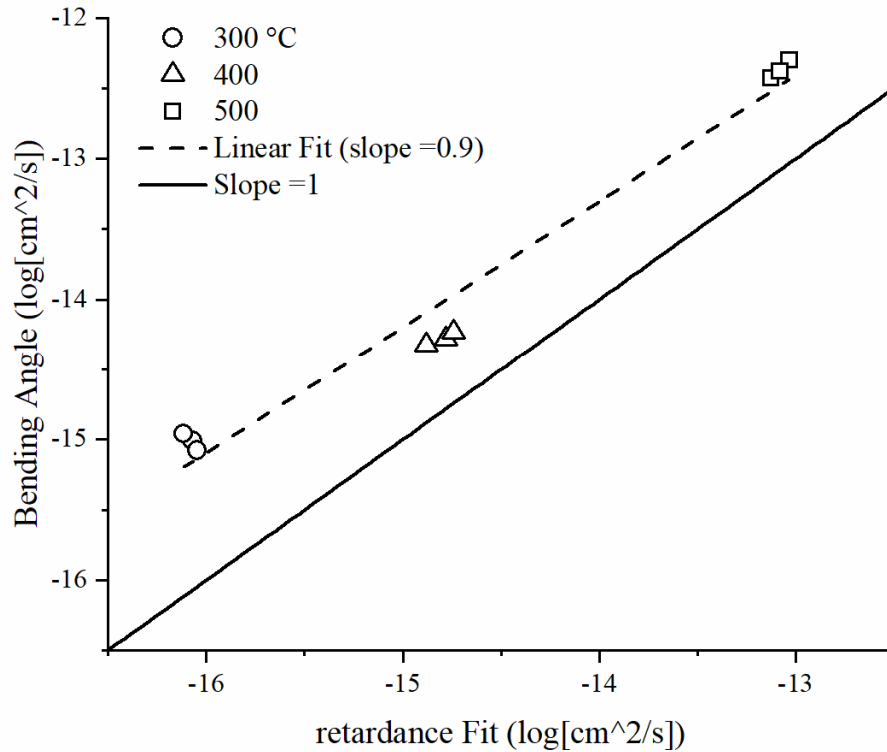


Figure 3.8. Comparison of diffusivity values calculated using the two discussed methods. A linear regression was applied to demonstrate the systematic difference in calculated diffusivities of about 10 percent overall.

3.2.4 Discussion

Diffusivity values measured via birefringence are consistent with the fiber bending angle measurement method developed previously within the measurable temperature range, affirming previous predictions above 300°C.⁵⁴ Diffusivity of surface stress relaxation for silica glass with various impurities were measured previously in the temperature range 400-700°C. Within this temperature range, a single activation energy, higher than observed in this work, was observed of ~164-188 kJ/mol.^{54, 78} The difference in measured diffusivity of bending angle and retardance may be a result of changes in the fiber surface stress optic coefficient or elastic modulus via increased water content following heat treatment.

Diffusivity of surface stress relaxation appears to be slightly higher for surfaces under compression (see figure 3.5). This result has also been shown previously for water diffusion in thin glass plates under bending, in which the stress dependence of water diffusivity changes trend in the same manner seen here in bending stress relaxation diffusivity.¹⁸ Previous work has also found that OH diffusivity is time-dependent at low temperatures due to the non-equilibrium nature of its reaction with the silica network.⁶ As the stress relaxation diffusivity is dependent on diffusion of water, it is possible that at low temperatures the relaxation diffusivity may also be time dependent. This may be investigated with longer time relaxation experiments or by altering environmental water concentration.

The presence of a small residual stress in the as-received fiber may have also influenced the diffusivity of surface stress relaxation. The fiber used in this work was found to have a small residual compressive stress at the surface prior to heat treatment, which may have resulted in an underestimation of applied compressive stress as well as an overestimation of the applied tensile stress at the bending apex. Fiber annealing has been shown to eliminate any measurable retardance caused by residual stress or anisotropy in the as-received fibers.⁷⁷ Although annealed fibers have shown some difference in the diffusivity of surface stress relaxation due to changes in fictive temperature, no difference in the activation energy with fictive temperature was observed in the 450-700°C temperature range, previously characterized in silica glass fibers with 1000 ppm Cl impurities.⁹ Use of annealed fibers to measure the diffusivity of surface stress relaxation at low temperatures, therefore, would eliminate the effects of residual stress from fiber

drawing or anisotropy and additionally remove the need for background subtraction of residual stress.

3.3 Shear stress relaxation and residual stress

3.3.1 Analysis of residual shear stress

Shear strain was applied to a silica glass rod by applying a constant angle of twist. A monotonic decrease in the total torque in the sample was monitored as the rod was heat-treated, demonstrating a stress relaxation over time.²³ At the beginning of the experiment, applied shear stress is a function of radial position

$$\tau_{applied} = \frac{G \cdot r \cdot q}{L} \quad (3.16)$$

where q is the angle of twist in radians, L is the gage length of the sample, G is the shear modulus, and r is a radial coordinate defined within the rod from $0 \leq r \leq r_o$. The maximum shear stress, τ_{max} , occurs at r_o at time 0, prior to any relaxation. Similar to the relaxation that occurs in fiber bending, the stress is assumed to relax in a diffusion-controlled manner approximated by the complementary error function. The change in the shear stress due to relaxation is given by equation (3.17).

$$\Delta\tau_{relax} = \tau_{applied} \cdot \operatorname{erfc}\left(\frac{(r_o-r)}{2z}\right) \quad (3.17)$$

The shear stress as a function of radial position and time during the relaxation experiment is therefore defined as

$$\tau(r, t) = \tau_{applied} - \Delta\tau_{relax} = \tau_{applied} \cdot \operatorname{erf}\left(\frac{r_o-r}{2z}\right) \quad (3.18)$$

The total torque in the sample is a function of time throughout the duration of the heat-treatment.

$$T(t) = \int_A \tau(r, t) r dA = \int_0^{2\pi} \int_0^{r_o} \tau(r, t) r^2 dr d\theta \quad (3.19)$$

Substitution of equation (3.18) into equation (3.19) gives

$$T(t) = G \frac{q}{L} \frac{\pi}{2} \left[-\frac{2r_0 z \left(-4(r_0^2 + 4z^2) + e^{-r_0^2/4z^2} (r_0^2 + 10z^2) \right)}{\sqrt{\pi}} + \right. \\ \left. (r_0^4 + 12r_0^2 z^2 + 12z^4) \operatorname{erf} \left(\frac{r_0}{2z} \right) \right] \quad (3.20)$$

When $z \ll r_0$,

$$T(t) = G \frac{q}{L} \frac{\pi}{2} \left[-\frac{8r_0^3 z}{\sqrt{\pi}} + r_0^4 \operatorname{erf} \left(\frac{r_0}{2z} \right) \right] \quad (3.21)$$

At the completion of the rod heat-treatment, the applied strain is removed. The rod springs back to an angle of twist per unit length $\frac{q_{spring}}{L}$, where $\frac{q_{spring}}{L} < \frac{q}{L}$.

$$\Delta \tau_{spring} = Gr \left(\frac{q}{L} - \frac{q_{spring}}{L} \right) \quad (3.22)$$

The residual shear stress in the rod is defined by

$$\tau_{residual} = \tau_{applied} - \Delta \tau_{relax} - \Delta \tau_{spring} \quad (3.23)$$

Since no torque is being applied, the total torque in the rod would become zero.

$$T = 0 = \int_A \tau_{residual} r dA = \int_0^{2\pi} \int_0^{r_0} \tau_{residual} r^2 dr d\theta \quad (3.24)$$

Substitution for $\tau_{residual}$ in equation (3.24) and solving for $\frac{q_{spring}}{L}$ gives

$$\frac{q_{spring}}{L} = \frac{4}{r_0^4} \frac{q}{L} \int_0^{r_0} r^3 \operatorname{erfc} \left(\frac{r_0 - r}{2z} \right) dr \quad (3.25)$$

Equation (3.23) becomes

$$\tau_{residual} = G \cdot r \cdot \frac{q}{L} \cdot \left[\frac{4}{r_0^4} \int_0^{r_0} r^3 \cdot \operatorname{erfc} \left(\frac{r_0 - r}{2z} \right) dr - \operatorname{erfc} \left(\frac{r_0 - r}{2z} \right) \right] \quad (3.26)$$

where z is the only unknown and all other variables are measurable.

A schematic of the shear stress applied to the rod, shear stress after relaxation has occurred to $z = 0.05r_o$, and the residual shear stress following spring-back are shown in figure 3.9 assuming an erfc relaxation profile.

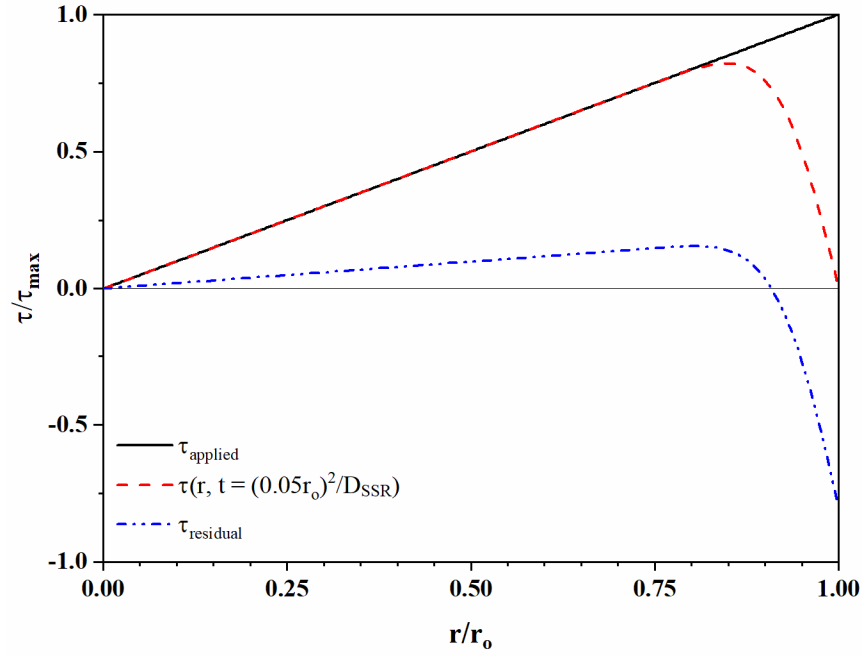


Figure 3.9. Schematic of shear stress relaxation relative to the maximum applied shear stress. Applied stress is defined by equation (3.14). Once the stress has relaxed to depth $z = 0.05r_o$, the stress is defined by equation (3.16). The residual stress following removal of the applied shear strain is defined by equation (3.24).

3.3.2 Experimental procedure

A silica glass rod (GE 214) with radius $r_o = 3.515 \pm 0.010$ mm and a 10 cm long gage section was used for the shear stress relaxation experiment. GE 214 has a shear modulus (G) of 31.6 GPa.²³ A shear strain was applied to the rod by applying a constant angle of twist, giving $T(0) = 0.6805 \text{ N} \cdot \text{m}$, $\frac{\theta}{L} = 0.08978 \text{ rad} \cdot \text{m}^{-1}$, and $\tau_{\text{max}} = 9.978 \text{ MPa}$. The sample was heat-treated at 650°C for 4 days in air with 7 torr ($\sim 1 \text{ KPa}$) of water vapor. The gage section of the rod was sectioned according to figure 3.10 in order to measure this shear stress. The circular faces of each

cylinder were mechanically ground using silicon carbide paper from 400 to 1200 grit in water followed by a final chemical-mechanical polish using a cerium oxide and water slurry. This procedure allowed retardance to be measured over a constant thickness. Six cylinders were cut and polished concurrently, resulting in a final thickness of 2.800 ± 0.014 mm. Rotational alignment was maintained by scribing a shallow scratch along the sample (see the red line in figure 3.10).

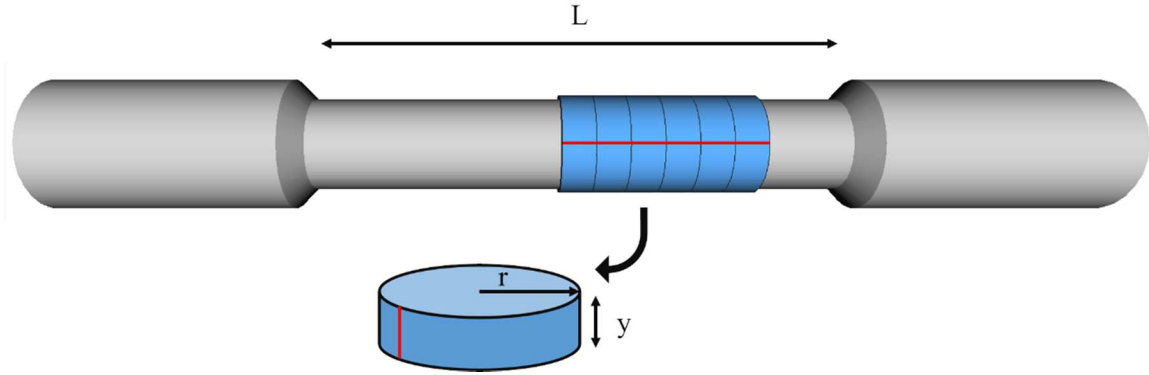


Figure 3.10. Schematic of shear relaxation sample geometry. Gage section was cut and polished to a consistent thickness for six samples. Dimensions indicated correspond to those in equations (3.13) and (3.14). The line across the section surface corresponds to the scribe mark used for section alignment.

Retardance in the glass cylinders was measured by passing polarized light through the sample along the y -direction in figure 3.10. Samples were immersed in index-matching fluid during measurement in order to mitigate scattering at the sample surface. The stress distribution is related to the retardance measurement by

$$\Delta(r) = C \cdot y \cdot \tau_{res} \quad (3.27)$$

where y is the thickness of the cylinder. The stress optic coefficient C can be shown to be the same value for shear and normal stresses in birefringent glasses.⁷⁹ In this work, C was estimated to be 3.0 Brewster [$10^{-12} Pa^{-1}$] based on values measured for similar silica compositions.⁷⁶ The shear stress measured in this work is the circumferential shear stress near the surface of the

cylinder parallel to its surface and is assumed to relax proportionally to the total torque relaxation of the rod. The retardance profile is thus fit using the parameter z since y , q/L , and r_0 are known. The relaxation depth, z , and diffusivity of surface stress relaxation, D_{SSR} , calculated from the retardance profile was compared to the values calculated from equation (3.21) for an erfc relaxation profile and the values calculated by Aaldenberg et al.²³ for a step function relaxation profile assuming complete relaxation from the surface to the depth z and no relaxation elsewhere (equation (3.28)).

$$T(t) = \frac{q \cdot G \cdot \pi}{2L} (r_0 - z)^4 \quad (3.28)$$

3.3.3 Results

Retardance measurements were taken from six low-magnification images and averaged to generate a representative profile (see figure 3.11). A higher magnification image was taken in order to better resolve the surface retardance as shown in figure 3.12. The depth of surface stress relaxation in figure 3.12b was estimated by fitting equation (3.26) and equation (3.27) to the retardance profile. Rotation of sample did not alter the birefringence pattern, indicating a circular symmetry of the residual stress, as expected.

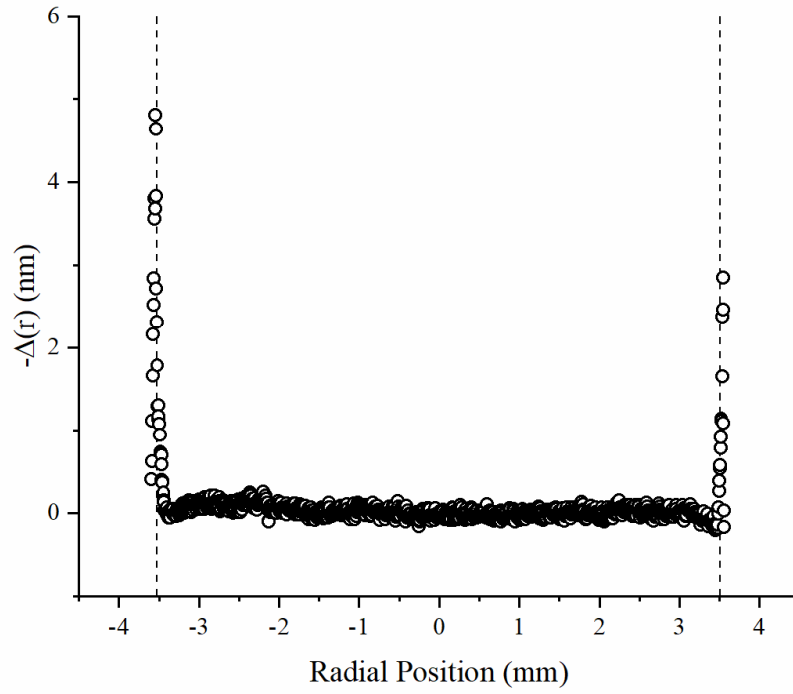


Figure 3.11. A superposition of six individual radial profiles is shown, confirming the predicted residual surface stress form but lacking necessary detail for fitting. The vertical lines mark the sample surface.

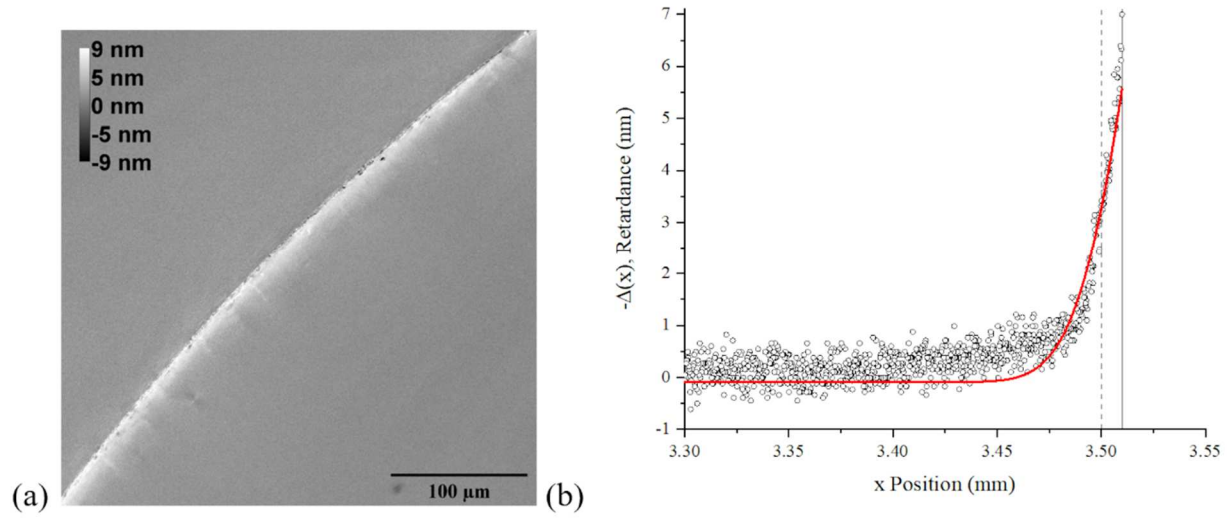


Figure 3.12. (a) High magnification image of the sample surface. Sample section interior is shown in the bottom right while the index matching oil is in the upper left. (b) Radial profile fit to equation (3.26). Relaxation depth z is indicated by the dashed line and the sample surface is indicated by the solid line.

The torque relaxation depth was also estimated using equation (3.21) and (3.28), as shown in figure 3.13.²³ The diffusion depth estimates from optical measurement and torque relaxation are given in table 3.2 along with the diffusivity for surface stress relaxation from equation (3.1). It was observed that the surface relaxation depth determined by Optical Retardance was greater than that determined by relaxation kinetics by $\sim 50\%$.

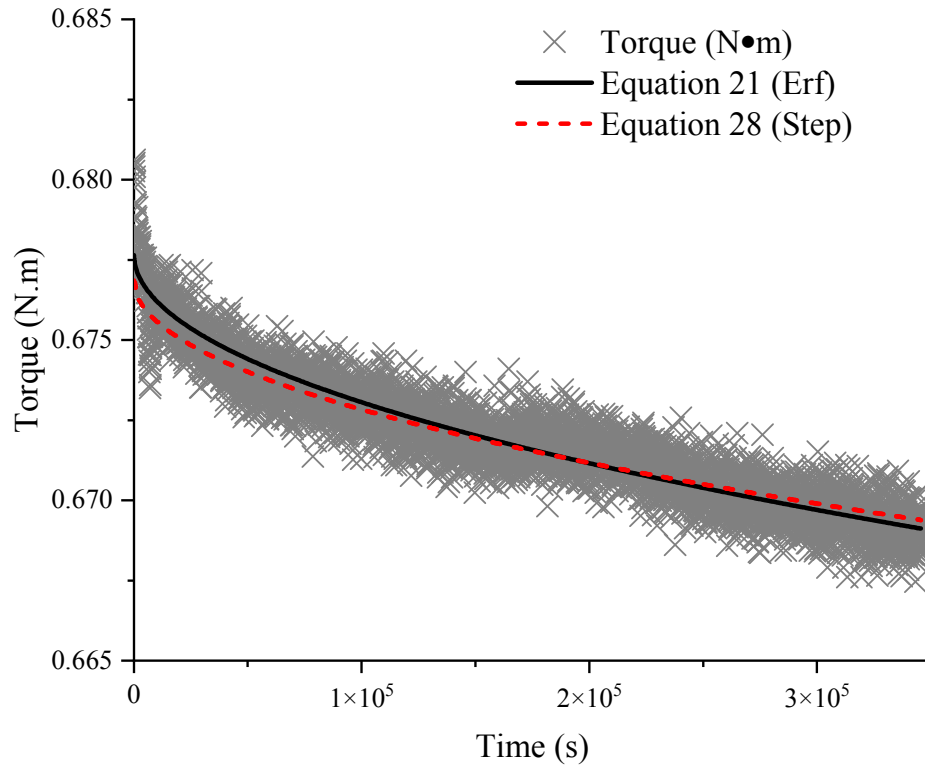


Figure 3.13. Torque relaxation during heat treatment with fits using equation (3.21) and (3.28).

Table 3.2. Comparison of surface shear stress relaxation depth and diffusivity by method.

| Method | Equation | z [μm] | D_{SSR} [cm^2/s] |
|---|----------|-----------------------|---|
| Optical retardance | 3.27 | 16.9 | 8.25×10^{-12} |
| Torque relaxation, erf relaxation profile | 3.21 | 9.89 | 2.84×10^{-12} |
| Torque relaxation, step relaxation profile ²³ | 3.28 | 10.9 | 3.43×10^{-12} |

3.3.4 Discussion

Application of the error function fit retains the consistency of the simpler step function for fitting the measured torque relaxation, while also allowing for fitting of the measured retardance profile. This compatibility further affirms that torque relaxation follows the developed surface stress relaxation model. Retardance measurement of the residual stress finds a diffusivity which is higher than the torque relaxation fit regardless of assumptions regarding relaxation profile. In order to confirm that the observed larger surface stress relaxation diffusion coefficient obtained by birefringence was not caused by sample thickness variation (i.e., non-uniform thickness near the sample surface), deviation from the sample thickness as measured by micrometer was found as a function of radial position (figure 3.14). This deviation was obtained by use of a contact profilometer, which measured change in relative height from the sample surface up to one edge. The change in thickness ($\sim 0.035\%$) was found to be sufficiently small as to not significantly affect the retardance measurement. This thickness variation accounts for possible retardance variance of only ± 0.024 nm.

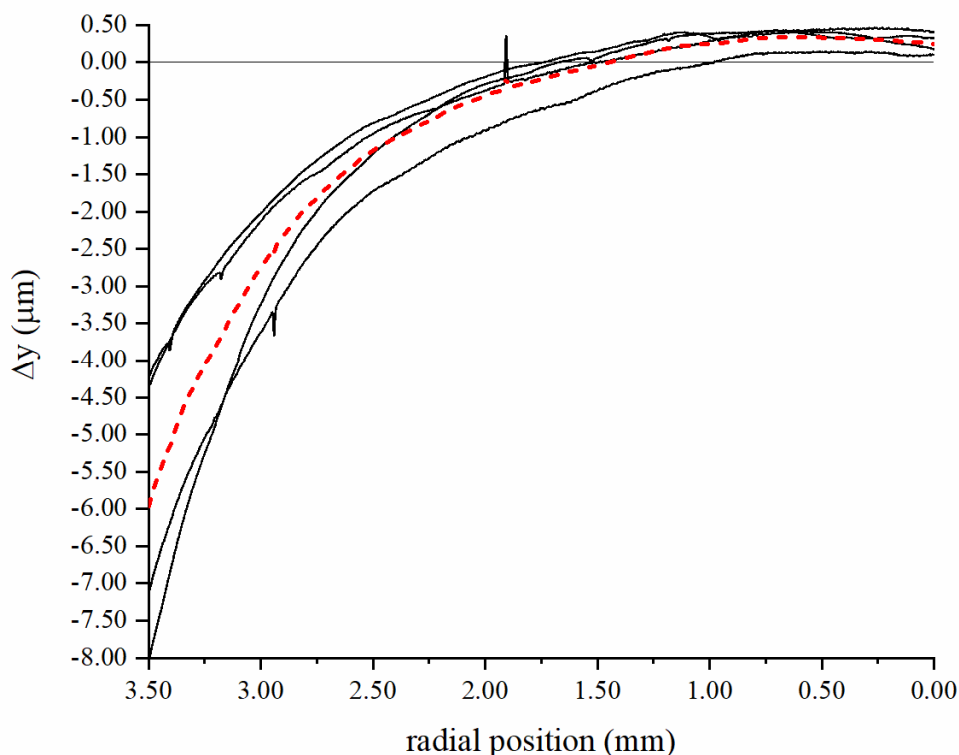


Figure 3.14. Deviation from thickness measured by micrometer as a function of radial position for one sample, as measured by profilometer. The solid curves are profiles measured from several sample rotations, with an average given by the dashed line. Maximum change in depth near the sample surface was found to be about 10 microns.

The observed difference between torque relaxation and retardance-measured z values is likely due to a combination of the greater sensitivity of the retardance measurement as well as the surface roughness at the cylindrical face of the sample (a consequence of sample machining before heat treatment), leading to slightly deeper relaxation than predicted for a perfect cylinder. This machined surface is preferable however to a smooth flame-polished surface, as it has been shown flame polishing introduces OH groups into the glass surface, thereby altering relaxation behavior.⁷² Other possible sources of error are similar to that of the optical fiber experiment,

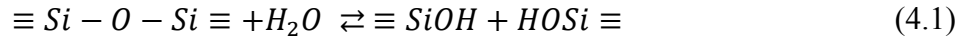
such as changes in the stress optical coefficient or shear modulus of the glass following water diffusion.

3.4 Conclusion

Low temperature stress relaxation has been confirmed to occur in the near-surface region of bent silica fibers as well as in sheared silica rods using optical retardance measurements. The stress distribution as calculated from retardance measurements agrees with the expected result, assuming a diffusion-controlled relaxation using the complementary error function. Agreement with the model is good across a large time and temperature range in bending. Differences in low temperature bending relaxation in the tensile and compressive surfaces, as indicated by the retardance measurements at 300°C agree with previous observations. In shear, torque relaxation measurements were found to agree well with the measured retardance profile, both of which can be modeled with good agreement using assuming diffusion-based surface stress relaxation.

4. RESIDUAL STRESS AND WATER DIFFUSION IN AT-REST SILICA GLASS PLATES AT LOW TEMPERATURES

Diffusion of water in silica glass has been frequently studied and is known to be sensitive to environmental changes such as temperature and ambient water vapor^{6, 8, 80}, as well as impurity compositions and applied strain.^{17, 18} Water diffuses as molecular water, H₂O, which reacts with the glass network to form immobile hydroxyl, OH, groups by the following reaction⁴:



At high temperature the reaction takes place rapidly, and reaches the local reaction equilibrium and its effective diffusion coefficient has been found to follow the following:

$$D_{\text{eff}} = \frac{4 \cdot [OH] D_{H_2O}}{K} \quad (4.2)$$

where K is the reaction equilibrium,

$$K = \frac{[OH]^2}{[H_2O]} \quad (4.3)$$

D_{H_2O} is molecular water diffusion coefficient, and $[OH] \gg [H_2O]$.

Previous works have characterized water diffusion through measurement of OH concentration profiles in low-water silica glass.^{6, 9, 22} At very low temperatures, below 550°C, surface OH concentration increases toward an equilibrium concentration over several hours. Between 550 and 850°C, surface OH concentration is seen to increase beyond equilibrium value, extrapolated from higher temperature values, then decreasing toward the expected concentration based on higher temperature data. It has been proposed that this is due to initial compressive stress generation from water diffusion, which drives the reaction (4.1) to the right, followed by surface

stress relaxation which drives the same reaction (4.1) to the left⁹ (figure 1.2, line (b)). These characteristics are summarized in figures 1.2 and 1.3.

This hypothesis appears to be consistent with the effect of applied bending stress on water diffusion in SiO₂ glasses^{17, 18}. Nogami and Tomozawa¹⁷ showed that the water solubility in silica glass is higher under compressive bending stress and lower under tensile stress at 192°C and 350°C. Agarwal et al¹⁸ subsequently showed that water solubility was higher under compressive stress and was lower under tensile stress at 250°C, while water solubility at 650°C was higher under compressive stress for short times, eventually reversing at longer heat treatment time.

In the present work, residual stress profiles of silica glass were measured as a function of water diffusion time using photoelastic techniques and were compared with previously obtained OH diffusion profiles in order to verify the theory of stress buildup and relaxation during low temperature heat treatments.

4.1 Experimental procedure

4.1.1 Sample preparation

Low water silica glass samples were cut from optical fiber preform (Furukawa Electric Co.) containing < 0.1 wt. ppm of OH and 1000 wt. ppm of Cl. This glass is similar to Type IV according to the classification by Bruckner.⁸¹ The glass transition temperature has been reported as 1096 °C.⁵⁹ Samples were cut into rectangular prisms of 10mm x 10mm x ~75mm and polished on two of the long parallel surfaces with shaded planes with 10 mm x 75 mm (see figure 4.1 (a)). Polishing was performed using a progression of silicon carbide paper from 240 to 1000 grit

followed by a final polish using cerium oxide in distilled water. Samples were then annealed at T_g for one hour in lab air at ~ 1 kPa (~ 7 Torr) water vapor pressure and left to furnace cool. To remove potential surface crystallization due to annealing, the sample was etched in 48% HF for 60 seconds to remove ~ 1 μm from all of the surfaces. After polishing and etching, final dimensions of the sample cross section were ~ 7 mm x 10 mm.

Samples were heat-treated successively from 100 to 900 hours in an environment of constant partial water vapor pressure of 47.33 kPa (355 Torr). The temperatures of 350 and 650 $^{\circ}\text{C}$ were chosen in order to compare stress profiles with previous OH concentration measurements.^{6, 19, 22} In order to measure the stress profile of the sample cross section, a 3mm-thick child sample was cut from the main piece and the cross section was polished perpendicular to the previously polished diffusion surfaces using the same procedure and resulting in a final child sample average thickness of 1.8 ± 0.3 mm (see figure 4.1).

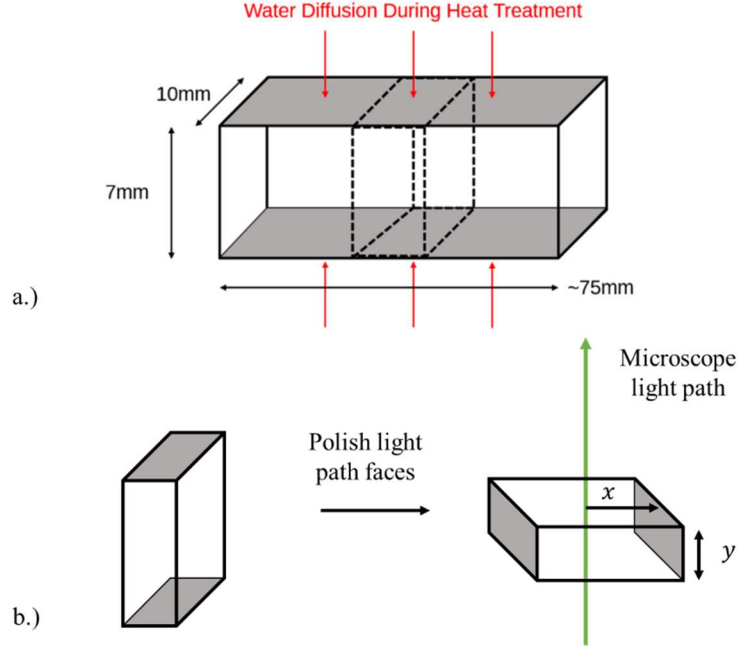


Figure 4.1. a.) Schematic of silica parent sample with the surface polished before heat treatment indicated with shading and approximate dimensions. An interior section is removed for characterization as indicated by the dashed lines. Incremental heat-treatment and thus water diffusion can be evaluated by subsequent sectioning. b.) Polishing of the cut cross section, and retardance measurement of said cross section is performed perpendicular to the diffusion surface or interest. Dimension y is the cross-section thickness (~ 2 mm) and x is the direction of diffusion, measured from the shaded surface inward.

4.1.2 Stress measurement

Stress profiles near the glass surface were measured using a polarized light microscope (Nikon Eclipse LV100N POL) via the Sènarmon technique for retardance measurement (figure 4.2).^{36, 41, 42, 77} Samples are immersed in an index-matching fluid to mitigate surface reflection of incident light (figure 4.3). Retardance was then measured as a function of position within the glass. Retardance is related to residual stress (in MPa) by the stress-optic law:

$$\sigma(x) = \frac{\Delta(x, \theta)}{C \cdot y} \quad (4.4)$$

where Δ is the retardance in nm, C is the stress-optic coefficient of the material in Brewsters [$10^{-12} \cdot \text{Pa}^{-1}$], and y is the path length through the material in mm. Retardance is found via

rotation of the microscope analyzer incrementally to determine the minimum transmitted intensity at a given point in the material. Retardance is then proportional to this angle and the wavelength of the microscope light source:

$$\Delta(x, \theta) = \frac{\lambda \cdot \theta_{min}(x)}{180^\circ} \quad (4.5)$$

the stress optic coefficient is approximated as 3.0 Brewster to estimate the magnitude of residual stress.⁷³ Stress as a function of depth, $\sigma(x)$, can accordingly be calculated by equation (4.4). The spatial resolution of the stress measurement is limited by the resolution of the camera and microscope optics to about $\pm 0.2 \mu\text{m}$. This is similar to the resolution of the OH profiles obtained by Davis, where successive etching of silica with dilute HF produced point measurements of OH concentration with a resolution of $\pm 0.5 \mu\text{m}$. The OH concentration profile was then measured from the change in these point measurements, resulting in an OH profile resolution of about $\pm 0.75 \mu\text{m}$.¹⁹ Calculated stress profiles were then used to determine stress generation and relaxation kinetics and compared with previously obtained OH diffusion profiles.

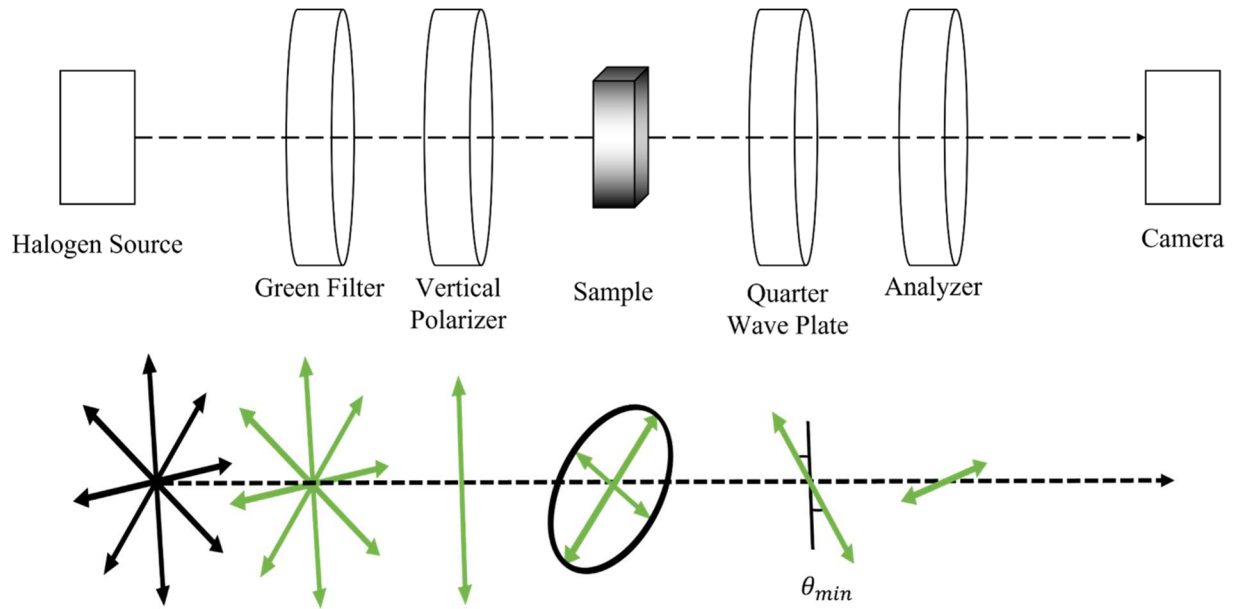


Figure 4.2. Schematic of the microscope configuration used for retardance measurement with the Sénarmont method. The optical components are shown above with the polarization state of the light shown schematically below. Elliptically polarized light is output from the sample which is at 45 degrees to the incoming polarized light. The difference in semimajor axes is proportional to the birefringence. Analyzer angle θ is incremented to find the minimum intensity resulting from a rotation of polarized light by the quarter wave plate, and thus retardance via equation (4.5).

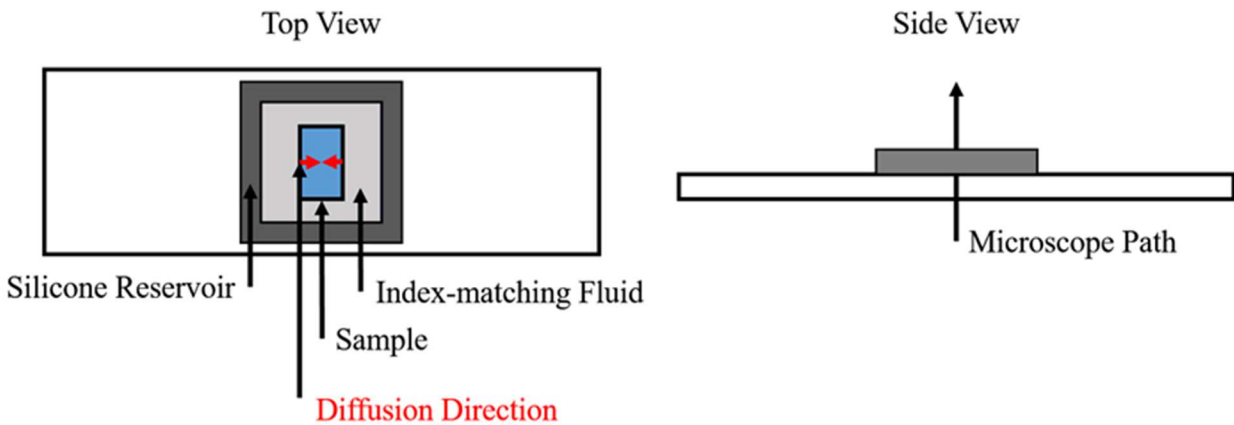


Figure 4.3. Experimental configuration during retardance measurement following heat-treatment illustrating orientation between the microscope and sample fixture. The sample is indicated in the center and measures roughly 10mm x 7mm x 2mm. Diffusion direction during heat treatment is indicated by arrows within the sample along the x axis defined in figure 4.1.

4.2 Results

Residual stress parallel to the glass surface was calculated as a function of distance from the surface using the measured retardance values (figure 4.4). Compressive stress was found to increase with successive 350 °C treatments up to 900 hours, similar to the trend seen in surface OH concentration (figure 4.5). A trend similar to surface OH concentration is observed in 650 °C treatments of initial increase followed by decrease (figure 4.6). At this higher temperature, surface stress is observed to relax on a similar timescale as OH concentration decrease, although the relaxation occurs more quickly. Along with a surface compressive stress, at 650 °C an interior tensile stress was observed, indicating temperatures are high enough for a structural deformation to occur at this timescale without significant change in water content deep within the glass. The interior zero-stress point is observed to correspond approximately with the previously measured depth of OH diffusion at the same heat treatment times (figure 4.6). These correlations are summarized in figure 4.7 in which the surface stress is compared to the surface OH concentration as a function of time.

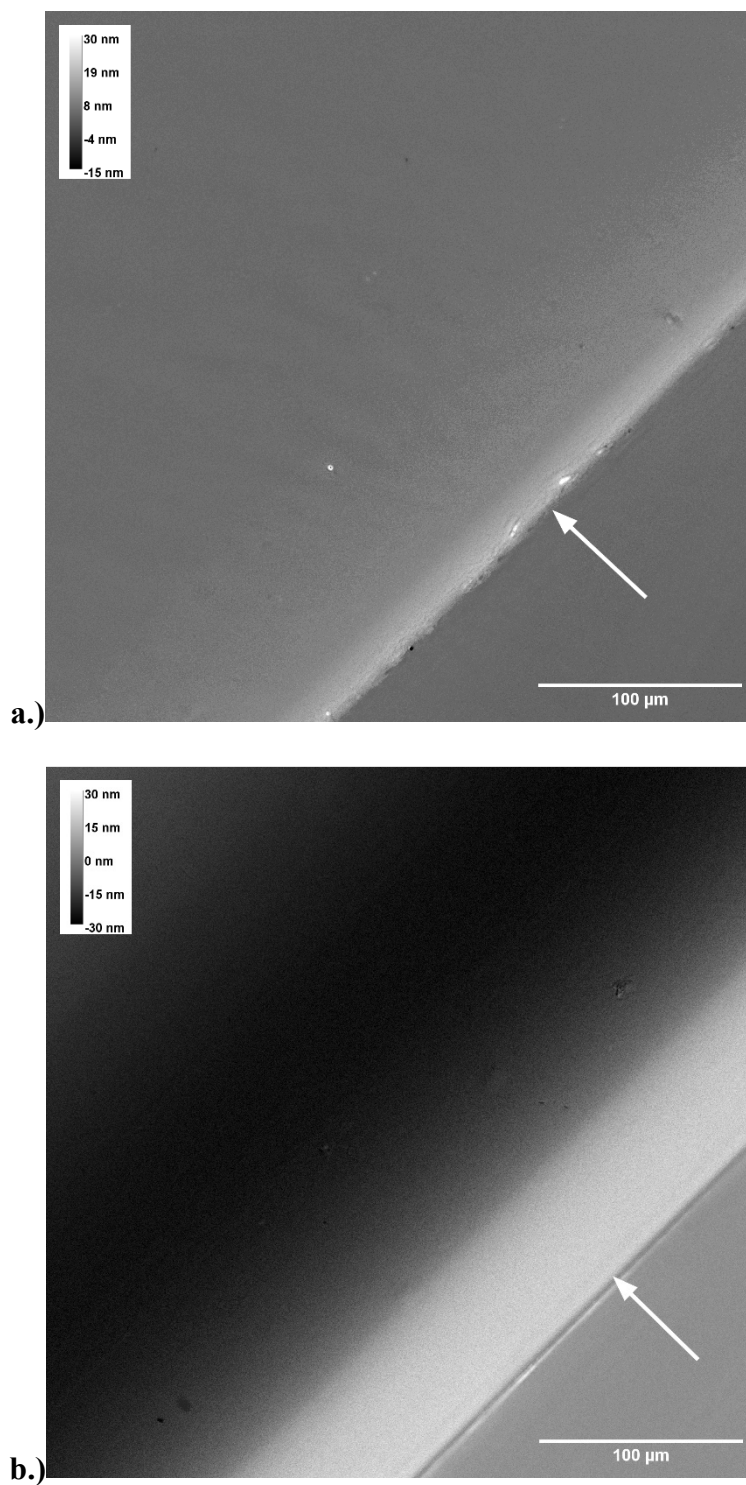


Figure 4.4. Retardance map of silica glass sample surfaces for samples heat-treated for 400 hours at 350 °C (a) and 650 °C (b). Glass surface is indicated with an arrow with the water diffusion into glass proceeding in the direction of the arrow (along coordinate x).

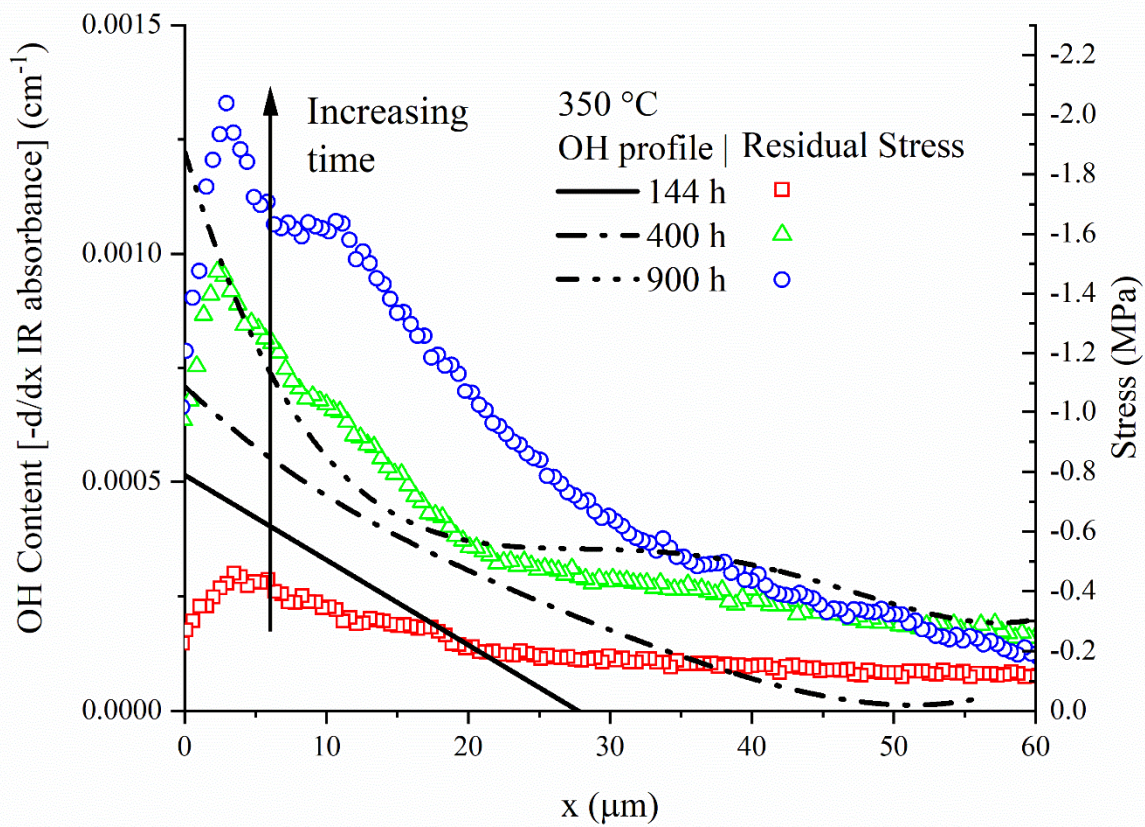


Figure 4.5. Residual stress profiles plotted alongside OH concentration profiles for 350 °C. OH concentration profile adapted from Davis.¹⁹

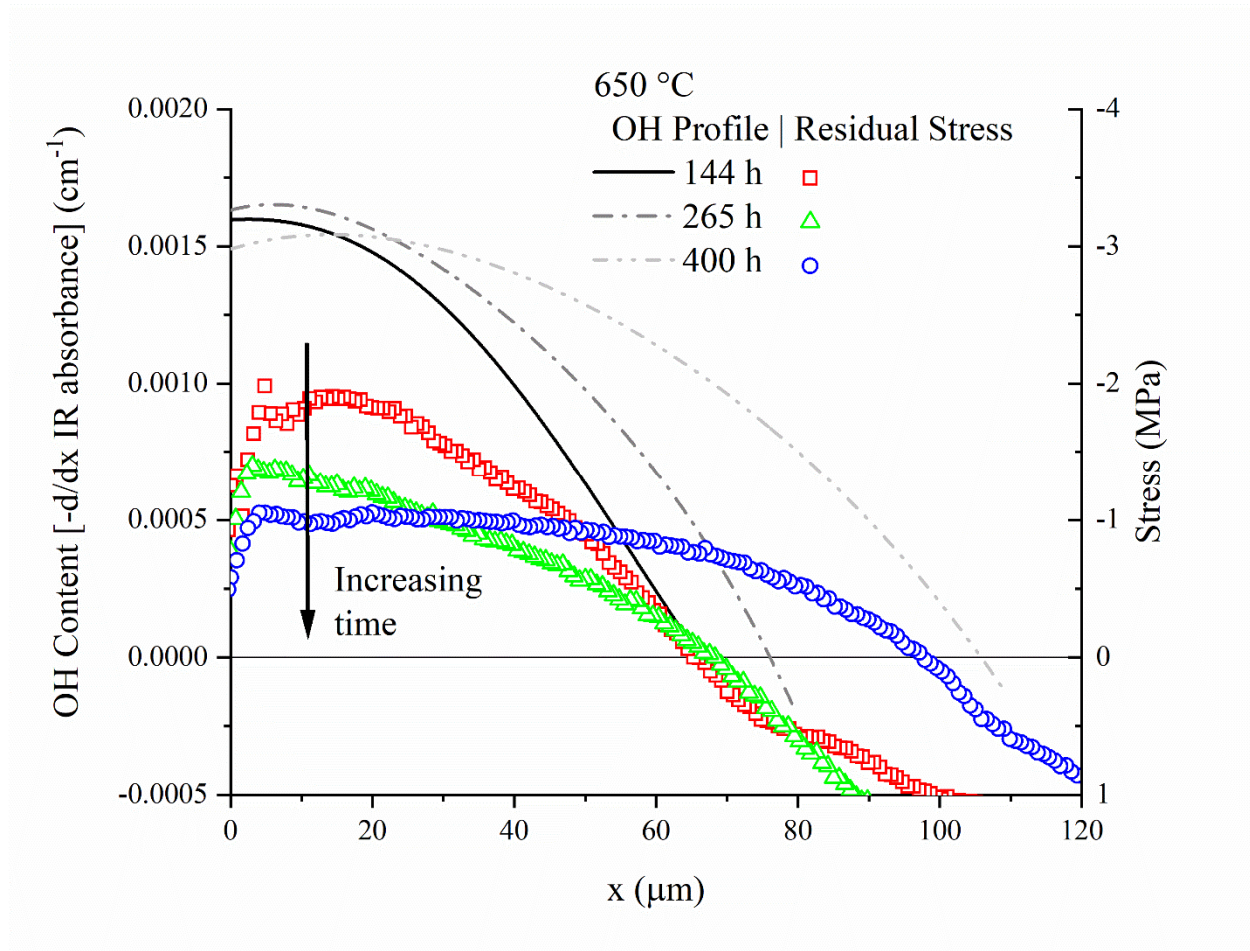


Figure 4.6. Residual stress profiles plotted alongside OH concentration profiles for 650 °C. OH concentration profile adapted from Davis.¹⁹ Over identical time periods, surface OH concentration is found to initially increase then decrease, while the same pattern is observed in residual stress following an initial delay.

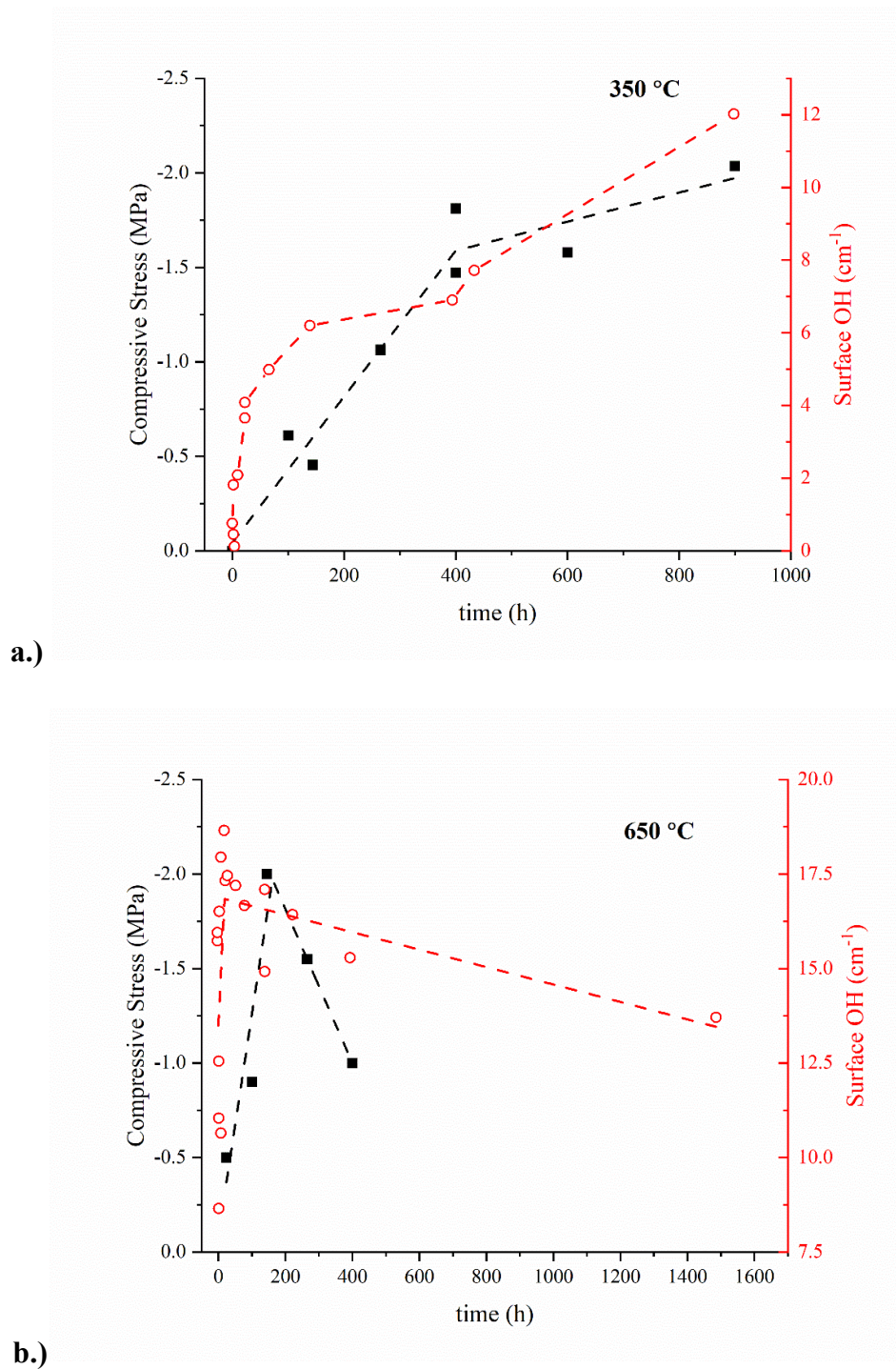


Figure 4.7. Comparison of surface residual stress (closed points) and surface OH content (open points) within the first $0.5\ \mu\text{m}$ of material as a function of heat treatment time for $350\ ^\circ\text{C}$ (a) and $650\ ^\circ\text{C}$ (b). Surface OH concentration adapted from reference.⁶ Note the slight delay at the higher temperature between surface OH concentration and residual stress change.

4.3 Discussion

The correlation between surface residual compressive stress and surface OH concentration is consistent for both temperatures, although at the higher temperature there is a more rapid relaxation than there is a decrease in surface OH concentration. Because fast relaxation at the glass surface has been observed at temperatures as low as 200°C, stress buildup in this work must be occurring more rapidly than relaxation in order to observe the initial increase.⁹ Upon reaching sufficient OH content and sufficiently decreased relaxation time, further stress increase may no longer outpace relaxation even at lower temperatures, producing the eventual decrease in surface compressive stress observed only at the higher temperature within the experimental timescale. This is likely a cause of time-dependent diffusivity of water in silica glass.^{8,9}

Although the compressive stress generated by water diffusion into silica glass can promote the reaction between silica glass and water molecule, the reaction is not instantaneous. Therefore, the compressive stress profile may precede the hydroxyl concentration profiles. The two profiles may not exhibit the same time and position profiles.

4.4 Conclusion

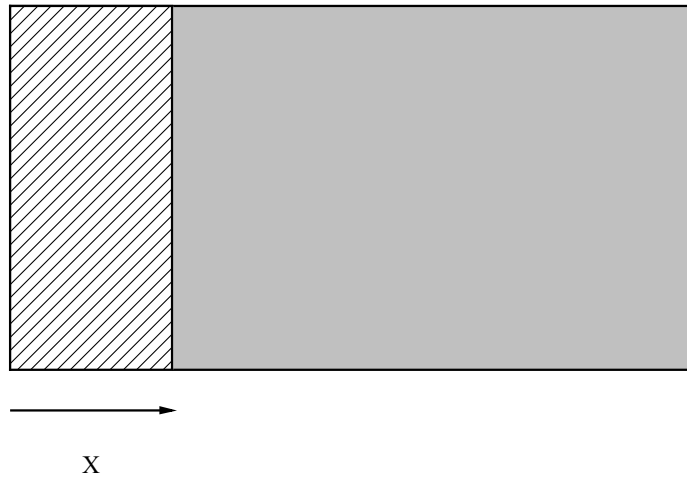
Low-temperature, long-time heat treatments of silica glass were found to result in residual stress buildup in a humid atmosphere of 355 Torr partial water vapor pressure at 350 and 650 °C. At both temperatures, residual stress was analyzed using photoelastic techniques and was found to correlate well with diffusion depth of OH groups in the glass network. At 650 °C surface compressive stress begins to decrease at a similar rate as surface OH content, implying a relation between residual stress relaxation and equilibrium OH concentration. The observed residual stress is likely the cause of previously measured time-dependent diffusivity in silica glass over similar temperature ranges.

5. CASE II DIFFUSION IN SODIUM SILICATE GLASS

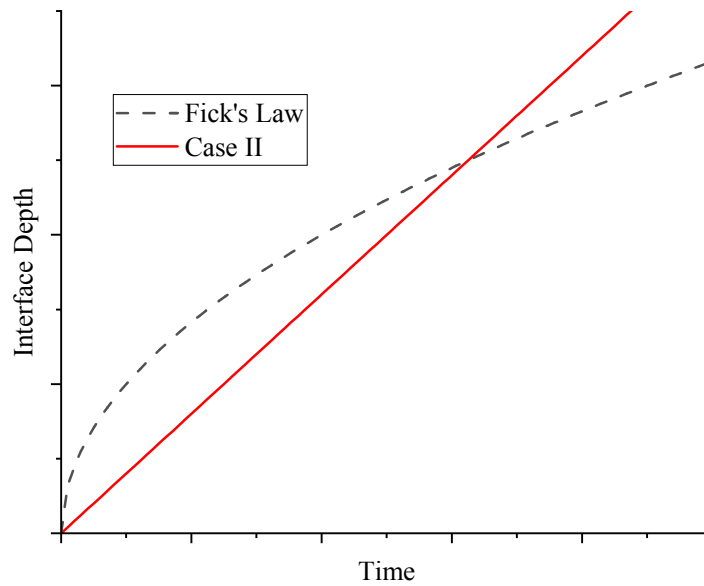
Transport properties in sodium trisilicate glass have been previously investigated, with particular interest in the diffusivity and conductivity of sodium ions in the material.^{28, 29, 33, 82, 83} During these works it was also found that below a certain temperature and depending on water content of the original glass, water transport does not follow the expected Fick's law behavior but instead can be described by what Alfrey *et al.*²⁶ originally referred to as case II diffusion (figure 5.1(a)). Case II diffusion occurs when there exists a step-like concentration profile which progresses through the material at a constant rate, with the concentration interface linearly progressing with time.²⁵ This is in contrast to Fick's law, which predicts an error function profile that progresses linearly with the square root of time (figure 5.1(b)).²⁵ At long times it has further been predicted for solvent diffusion in glassy polymers that case II diffusion would likely approach Fick's law square root dependence (figure 5.2).⁸⁴

Swollen Compressive Layer

Dry Tensile Layer



a.)



b.)

Figure 5.1. a.) Schematic of typical diffusion interface progression of case II diffusion, showing the interface progression at point X. b.) Schematic curves describing case II and Fick's law interface progression as a function of time.

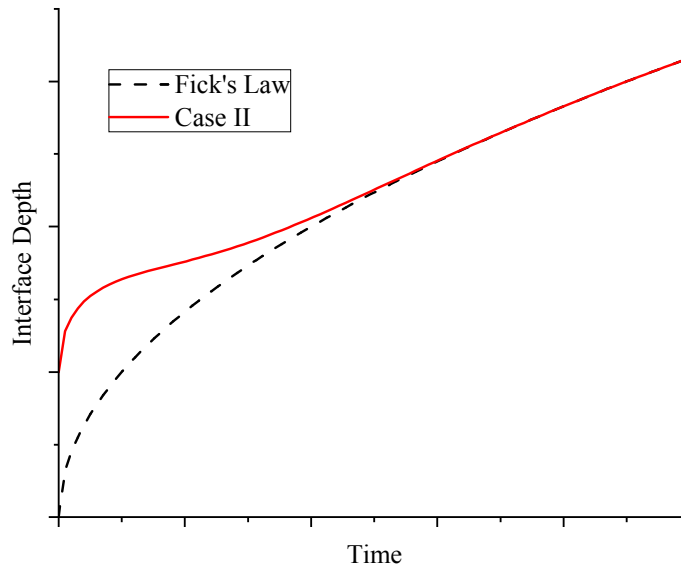


Figure 5.2. Schematic of the long-time behavior of case II diffusion, which has been observed to approach Fick's law as a result of stress relaxation in the case of glassy polymers.

Several theories have been developed to model possible mechanisms of case II diffusion, with particular focus on the phenomenon as it has been measured for solvent diffusion into glassy polymers. Crank proposed that case II behavior can be modeled as a concentration-dependent diffusivity, with a diffusion interface that can be predicted by an additional linear constant upon the boundary progression expected of Fick's law^{24, 85}:

$$X = k \cdot \sqrt{Dt} \quad (5.1)$$

where k is a constant determined for the material and experimental conditions, D is the diffusivity of the solvent, and t is time.

It was later suggested by Wang, Kwei, and Frisch³⁰ that a rule of mixing be applied to determine the case II and Fickian contribution to diffusion:

$$X = 2k \cdot \sqrt{Dt} + vt \quad (5.2)$$

where v is a term relating to the stress within the polymer as well as the general mobility of the penetrating species, both of which were thought to be relevant to the dominance of case II behavior in polymer-solvent systems.

A similar theory was developed by Cox and Cohen⁸⁴ which proposed that modification of the flux within the material include a linear dependency upon the stress gradient at the interface:

$$J = -\frac{\partial \mu}{\partial C} \nabla C - \frac{\partial \mu}{\partial \sigma} \nabla \sigma \quad (5.3)$$

where J is the flux in the material, μ is the chemical potential (assumed to depend on concentration and stress), C is the concentration, and σ is the stress within the plane where the flux is being measured, most notably near the diffusion interface. A similar, more general consideration has been suggested for diffusion in the presence of any external potential by Shewmon, with similar applicability⁸⁶:

$$J = -D \left(\nabla C + \frac{C \nabla V}{kT} \right) \quad (5.4)$$

where V is a general applied potential, stress or otherwise, and k is the Boltzmann constant.

Inspection of equations (5.3) and (5.4) allows a comparison between Cox and Cohen's stress gradient prediction and Shewmon's potential:

$$\nabla \sigma \propto \frac{\nabla V}{kT} \quad (5.5)$$

It is thus expected that the effect of the stress gradient is likewise thermally activated, similar to any other potential gradient effect upon the flux.

The conception of the stress dependence of flux at the interface is of interest as the stress in a material such as sodium trisilicate glass is measurable using photoelastic techniques,

allowing for experimental confirmation in a manner that is difficult to obtain for a polymer/solvent system. This work therefore investigates the diffusion behavior of sodium trisilicate glass while concurrently measuring the residual stress profiles at the diffusion interface in order to determine if the origin of case II diffusion behavior in the material might be described by the model developed via equations (5.3) and (5.4).

5.1 Experimental procedure

Sodium trisilicate glass, received as a large slab (Corning Inc.), was cut into samples measuring roughly one cubic centimeter. These were then annealed at 500 °C for one hour before furnace cooling. The annealing temperature of 500 °C was determined to be sufficient by differential thermal analysis (DTA) of a powdered sample to characterize T_g (figure 5.3), as has been measured for the same material previously.⁸⁷ A T_g of 457 °C was found, which was likewise found to be in good agreement with the estimated as-received water content of 800 ± 50 ppm or 0.08 wt% as determined by FTIR spectroscopy (figure 5.4).²⁷

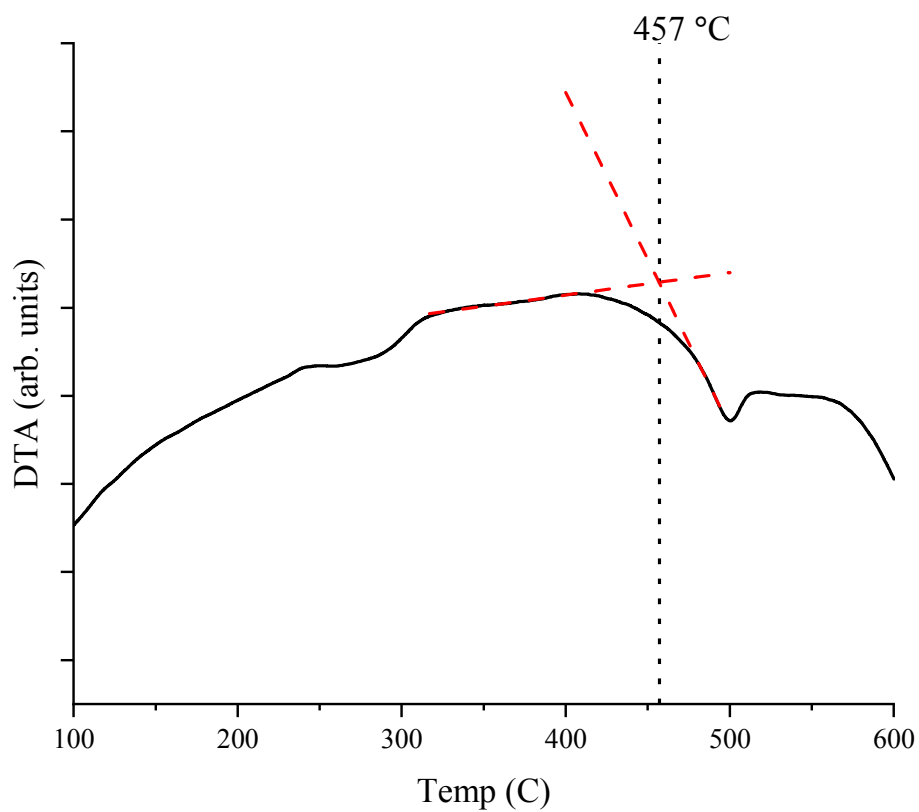


Figure 5.3. DTA curve depicting the glass transition temperature estimate from the change in heat of the glass sample. T_g value agrees with a sodium trisilicate glass containing approximately 0.1 wt% water.

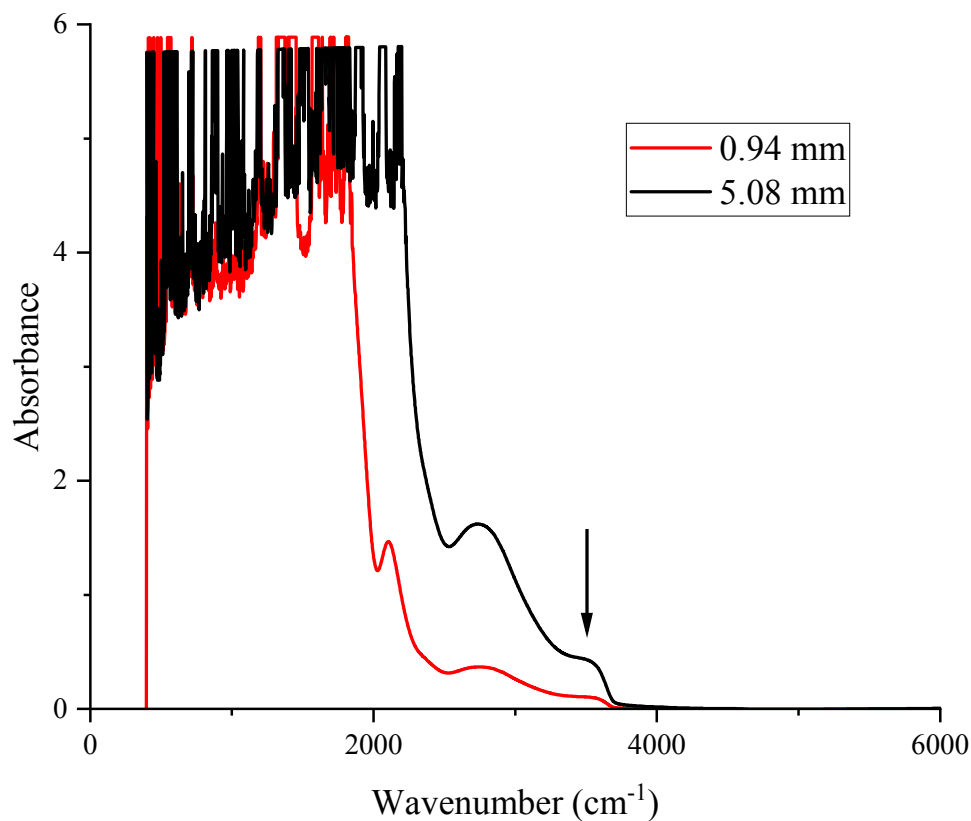


Figure 5.4. FTIR spectrum of two samples of sodium trisilicate glass polished to the indicated thickness. Water content was estimated to be 800 ± 50 wt. ppm using a practical extinction coefficient of 24 for the 3500 cm^{-1} as previously determined by Acocella.²⁷ The relevant band is indicated by the arrow for both spectra.

Four surfaces on the annealed samples were polished using progressively finer silicon carbide paper in steps of 240, 400, 600, and 1200 grit before a final polish of cerium oxide in distilled water. After polishing and immediately before heat treatment, samples were etched in a solution of 5% HF and 10% H₂SO₄ for 30 seconds. Initial dimensions of each sample were obtained following etching via optical measurement (Nikon Eclipse LV100N POL) in order to compare to the final dimensions of the sample following heat treatment and hydrated layer removal.

Samples were heat treated at 80 °C in a 355 torr saturated water vapor environment. In order to maintain this vapor pressure, samples were placed within a sealed PTFE container and suspended over a reservoir of deionized water (figure 5.5). Following successively doubled heat treatment times ranging from 6 to 48 hours, samples were removed from the reservoir and the hydrated surfaces were readily dissolved by room temperature water. The new dimensions of the sample were then measured optically and compared to the as-polished sample to find the depth of the diffusion interface.

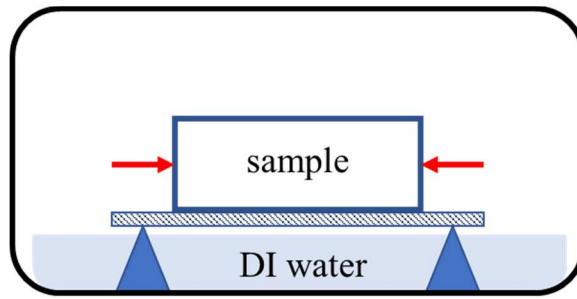


Figure 5.5. Schematic of sample configuration during heat treatment. Samples are suspended above deionized water, upon a silica plate, within a sealed PTFE vessel to ensure saturated vapor pressure during the experiment.

In addition to the depth of hydration, the residual stress in the remaining sample was characterized via birefringence measurement, using previously developed photoelastic techniques employed by the same microscope used for dimensioning of the sample (figure 4.2).^{38, 41, 77, 88} Birefringence is related to residual stress in the glass by the stress optic law:^{35, 73}

$$\sigma = \frac{\Delta}{C \cdot y} \quad (5.6)$$

where σ is stress in MPa, Δ is retardance in nm, C is the stress optic coefficient in Brewsters ($10^{-12} \cdot Pa^{-1}$), and y is thickness of the measured material in mm. Results are reported as birefringence (Δ/y) alongside approximate equivalent stress as it is unclear to what degree the

stress optic coefficient may vary with water content near the hydrated interface (although it is expected to be a small variation).⁸⁹ It is also likely that the effect upon stress optic coefficient is consistent across all heat treated samples. To avoid the interference of thermal expansion differences due to the change in temperature, a heated microscope stage (Bioscience Tools) was employed to perform the stress measurement at 80 °C in lab air (figure 5.6). The relatively low partial pressure of water assured negligible hydration during the measurement. Likewise, stress measurement at the chosen furnace temperature would assure all residual stress was a result of the heat treatment and hydration itself as opposed to the subsequent cooling of the sample. The collected residual stress profiles were then compared to existing models for Case II diffusion in order to discern if evidence for a clear mechanism existed in the measured stress and theorized water concentration profiles.

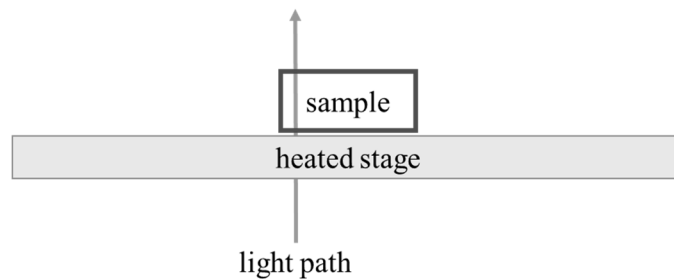


Figure 5.6. Schematic of the heated stage in relation to the incident light of the microscope and the sample.

5.2 Results

From 6 to 48 hours, the diffusion interface of the hydrated layer with the unreacted glass was found to progress at a rate of 4.67 ± 0.23 μm per hour (figure 5.7). As this interface progressed, a residual tensile stress was found consistently within the unreacted glass (figure 5.8). Maximum

stress initially increased before gradually decreasing with heat treatment time. The stress magnitude relaxation was fit to an exponential relaxation:

$$\sigma(t) \propto e^{-\frac{t}{\tau}} \quad (5.7)$$

where relaxation time τ of 37 ± 1.5 hours was found (figure 5.9).

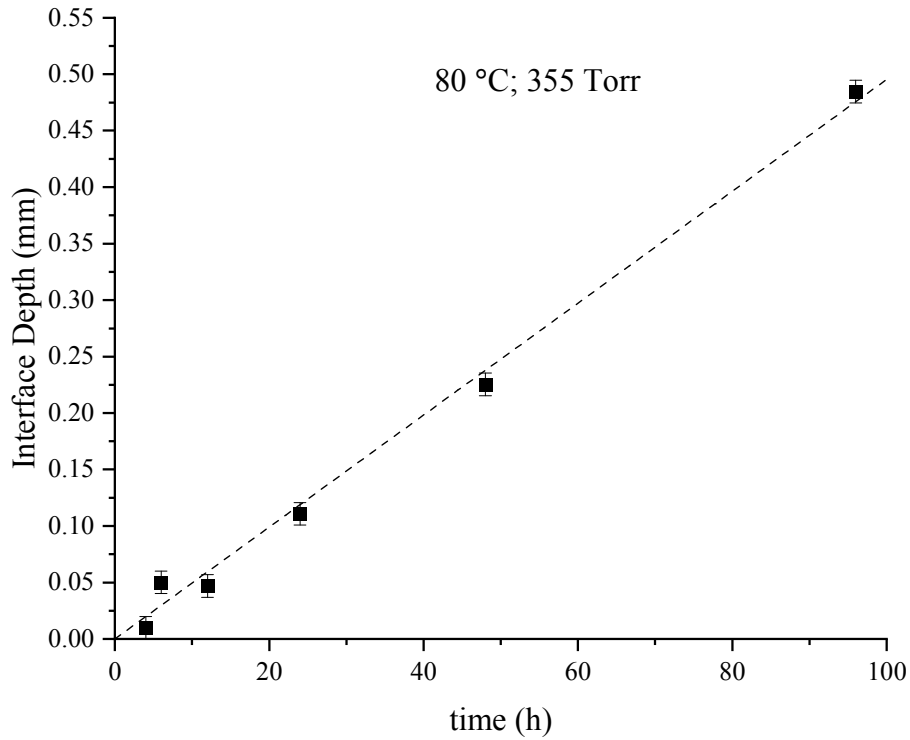


Figure 5.7. Diffusion interface depth versus time for water in sodium trisilicate at 80 °C saturated water vapor. Fit is linear with an intercept of zero and rate of $4.67 \pm 0.23 \mu\text{m}$ per hour.

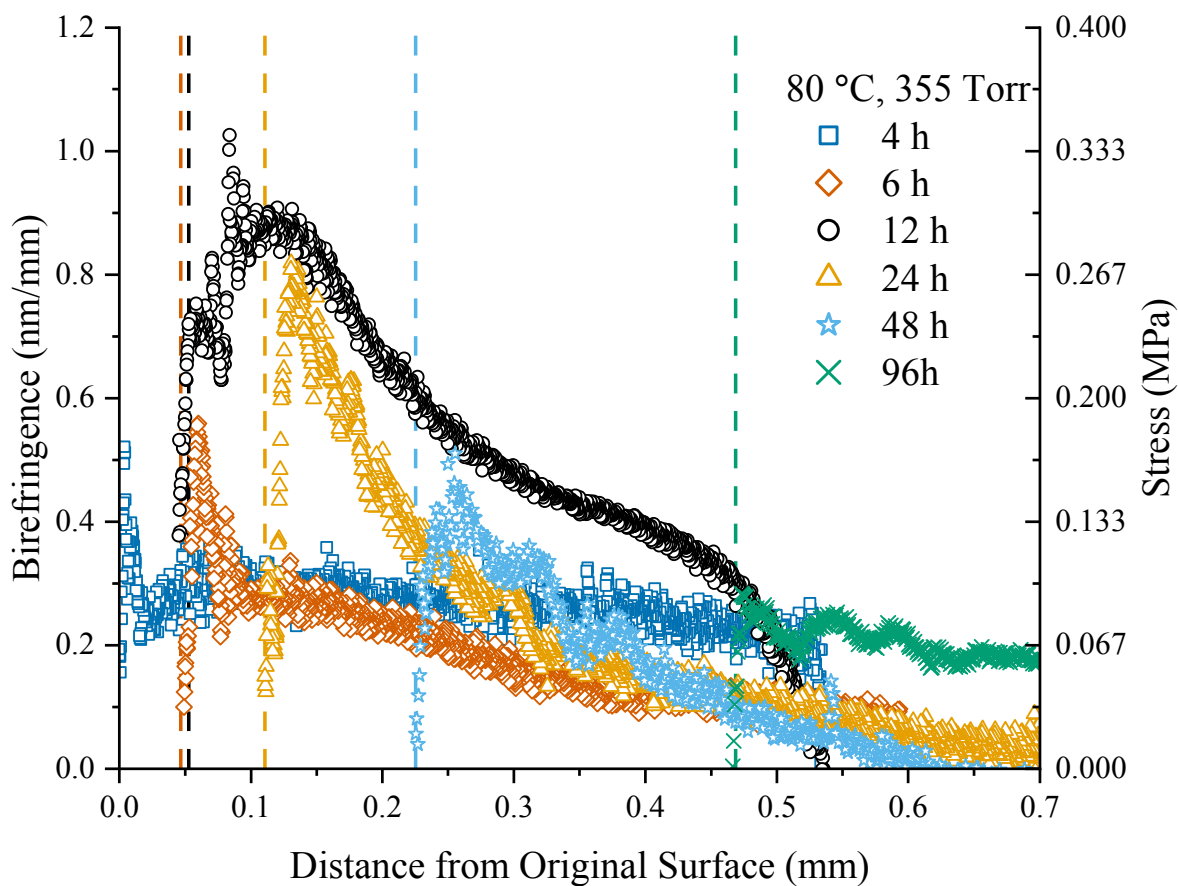


Figure 5.8. Residual stress profiles on the unreacted side of the diffusion interface in sodium silicate for 4 to 96 hours. Between 6 and 12 hours, the maximum stress begins to decrease. The interface appears to progress more slowly at this inflection but is still within experimental error for a constant interface velocity.

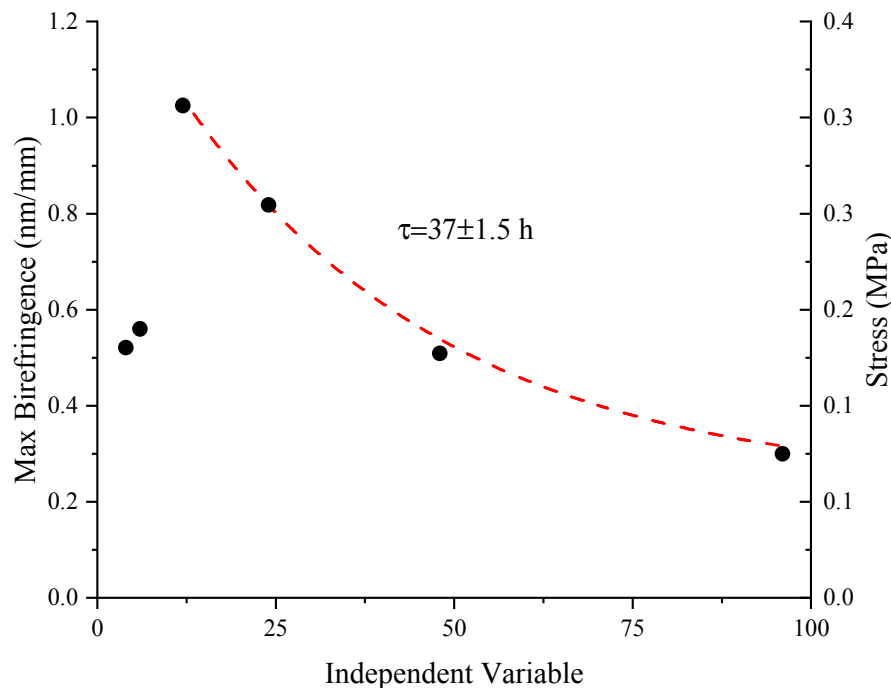


Figure 5.9. Measured maximum birefringence as a function of heat treatment time. A maximum is reached at about 12 hours at which point an exponential decay occurs as described by equation (5.7), with a relaxation time of about 37 hours.

5.3 Discussion

The width of the stress profiles follow a similar trend to the stress magnitude shown in figure 5.8, indicating the form of the stress profile is likely in fact the thermodynamically driven pressure profile predicted by Thomas and Windle^{31, 90} corresponding to a “solvent” (molecular water) activity that extends beyond the reacted water (OH) volume fraction profile. This is consistent with what is understood of molecular water transport in other glasses, in which molecular water diffuses more quickly into the network before reacting to form hydroxyl groups in a manner similar to the activity/volume fraction inequality described by Thomas and Windle for solvents in polymer systems.⁹ There are other parallels which can be drawn to Thomas and

Windle, namely the conception of the stress component of diffusion being directly correlated to the creep behavior of the material.⁹⁰ The magnitude of tensile stress decreases exponentially with time, similar to assumptions within Cox and Cohen's original derivation in which a standard linear model is assumed for viscoelastic stress relaxation.⁸⁴ The very high viscosity at room temperature for the unreacted glass excludes viscoelastic relaxation as the sole mechanism however; in reality, a combination of the rapidly changing sample geometry and viscosity with water uptake, as well as structural relaxation near the diffusion interface, may account for the relatively fast relaxation time at 80°C in saturated water vapor. Future work would benefit from characterization of the temperature dependence of case II diffusion in comparison to creep in the same material, as the activation energy for each process have been found to correlate experimentally for polymer/solvent systems.⁹⁰

It has previously been found that case II diffusion behavior was observed in sodium trisilicate glass as a function of temperature and water content well below the glass transition temperature (figure 5.10). The demarcation between case II and Fick's law behavior thus likely corresponds to the point at which the effective relaxation time becomes slower than the transport and reaction of water in the glass.

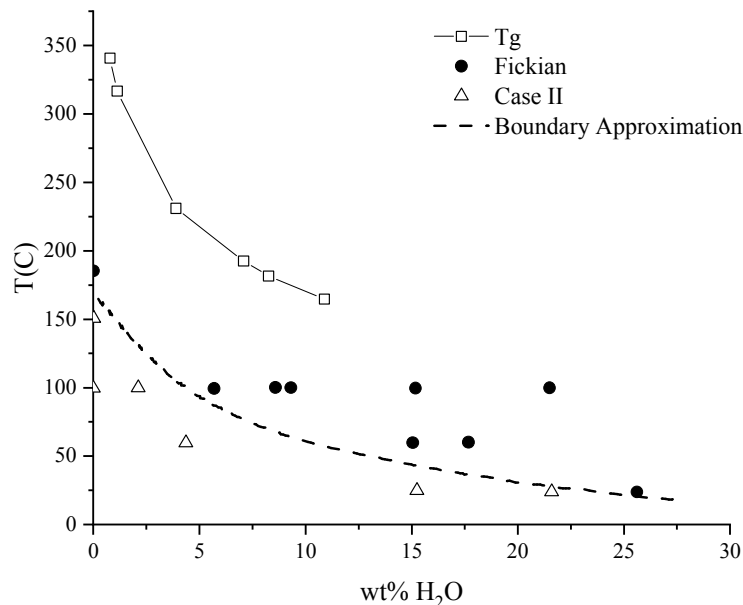


Figure 5.10. Comparison of dominant diffusion behavior in sodium trisilicate glass as a function of temperature and water content of the unreacted glass. The dependence of T_g with water content is also included. Data collected by Tomozawa and Molinelli.³³

Also noteworthy is the slope of the residual stress profile at the surface of each sample is very consistent between heat treatments (0.014 ± 0.009 MPa/mm) (figure 5.11). Because the interface moves at a constant velocity during heat treatment, it is to be expected that each interface experience the same degree of surface stress relaxation upon removal of the reacted gel layer, which accounts for the deviation between the observed and predicted stress profiles (figure 5.12). The negative stress gradient beyond the relaxation at the surface of the interface (directly following the sub-surface stress maximum) is similar to that predicted for a residual stress effect on the flux, as has been theorized in analogous polymer/solvent systems by Cox and Cohen.^{32, 84} In consideration of this, a linear fit of the residual stress gradient past the initial surface relaxation region was made and was found to decay relatively quickly before decaying significantly more slowly, (figure 5.13). The stress gradient seems to decay so slowly as to be

nearly constant beyond the point in time where maximum stress in the material occurs, suggesting a steady state of case II diffusion is reached. The slow decay of stress gradient meanwhile indicates the diffusion shall likely approach Fick's law behavior at much longer time, as predicted by Cox and Cohen. These observations agree with the behavior predicted by equations (5.3) and (5.4) and strongly suggest that for sodium trisilicate glass, case II diffusion is originated via the tensile stress gradient at the diffusion front.

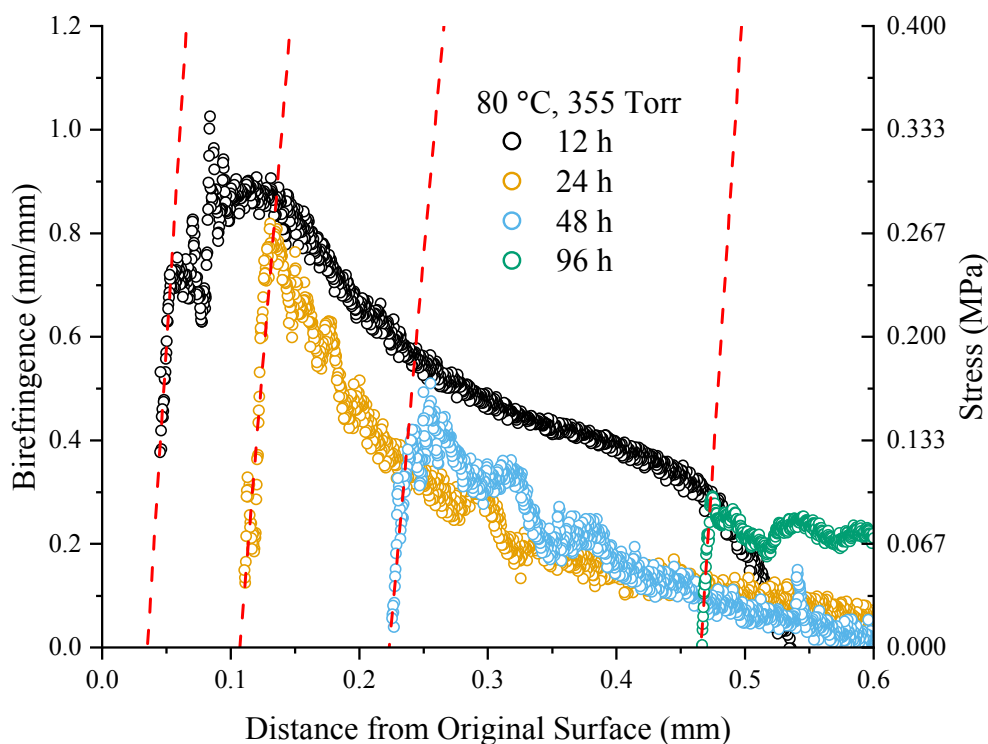


Figure 5.11. Retardance profiles from 12 to 96 hours displaying nearly identical initial slopes from the surface inward. The data was fit to an average slope of 0.014 ± 0.009 MPa/mm, or 0.0341 nm/mm^2 .

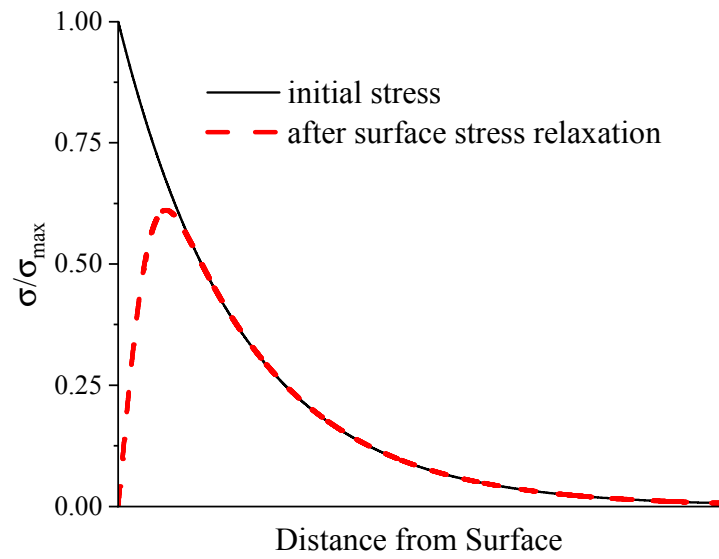


Figure 5.12. Schematic of the surface stress relaxation in comparison to the expected stress pattern assuming an error function relaxation, as observed in surface stress relaxation elsewhere. This relaxation accounts for the positive stress gradient at the surface whereas a negative gradient is to be expected if there were no relaxation.

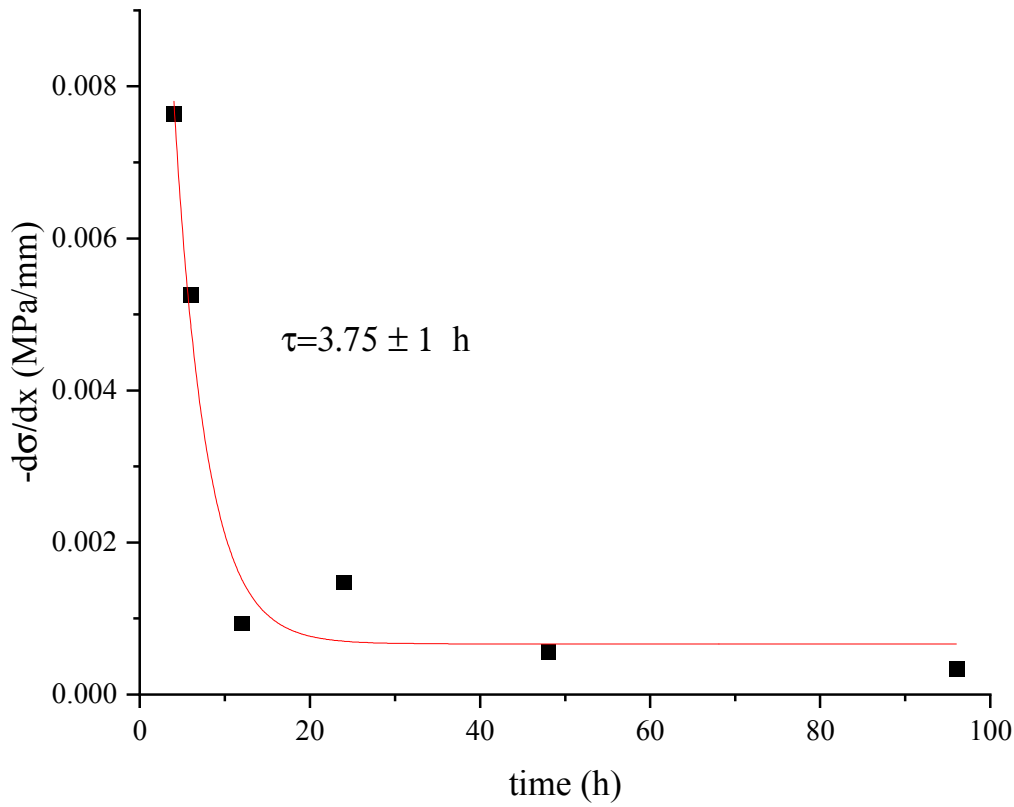


Figure 5.13. Negative stress gradient near the diffusion interface as a function of heat treatment time. The gradient is seen to decrease with time in a manner similar to the maximum tensile stress as seen in figure 5.9, although at a much faster pace. The relaxation time was estimated using the same exponential proportion as equation (5.7) and was found to be 3.75 ± 1 hour.

5.4 Conclusions

Residual stress at the diffusion interface has been measured as a function of successive low-temperature heat treatment in a saturated water vapor atmosphere. Case II diffusion was found to occur, with a near-constant tensile stress gradient found at the interface likely resulting from surface stress relaxation. Beyond the surface relaxation, the negative stress gradient is similar to what had been proposed theoretically and observed experimentally in glassy polymers. The fact

that a residual stress arises within the unreacted glass network likewise agrees with both the expected pressure profile predicted for solvents in glassy polymers, as well as with the previously observed diffusion/reaction behavior of molecular water within silicate glasses. The tensile stress gradient beyond the diffusion interface agrees with predictions of the stress dependence of flux in the material by Edwards and Cohen, indicating that tensile stress is the origin of case II diffusion in sodium trisilicate glass.

6. CONCLUSIONS

Residual stress in glass has been characterized following several experimental configurations, glass geometries, and thermal histories to better understand the effects of water in such procedures. Polarized light microscopy has been employed in concert with digital photography in order to measure the optical retardance following interaction with water. Through analysis of these characterizations, the following advances in understanding have been obtained:

- The strengthening effect of low temperature heat treatments of silica optical fibers under an applied tensile stress was confirmed to be the result of a surface compressive stress which arises as a consequence of surface stress relaxation. Residual stress is described accurately assuming an error function relaxation during heat treatment in a water-containing atmosphere.
- The same relaxation model can accurately describe surface stress relaxation of applied bending and torsion, confirming no volume change is necessary for fast surface stress relaxation and that in all cases relaxation can be modeled as an error function.
- Anomalous water diffusion in low-water silica glass was found to be highly correlated to surface residual stress. A strong correlation was found between surface hydroxyl concentration and surface compressive stress at 350 °C, while at 650°C the generation and subsequent relaxation of residual stress likewise correlates with hydroxyl concentration. This finding confirms previous hypotheses that the time dependence of solubility in silica at low

and intermediate temperatures is a result of stress relaxation driving reaction of water with the silica network.

- Water diffusion into sodium trisilicate glass follows a case II behavior in which a step-like concentration profile progresses with constant velocity through the material. A residual tensile stress was found at the diffusion interface, which matches previous models and experimental observations obtained for polymer/solvent systems which also display case II diffusion behavior. The combined observation of a linear interface velocity with a consistent tensile stress gradient at the interface itself confirms the origin of case II diffusion in sodium trisilicate glass as had been previously predicted for diffusion in glassy polymers.

These insights into the behavior of water at glass surfaces invite further investigation.

Replication and iteration of such experiments may allow insight toward the universality of the observations made during this work. Future work may include greater analysis of glass composition effects, expansions upon the experimental parameter space such as temperatures chosen for thermal processing, as well as entirely unique works leveraging the techniques developed here for separate purposes.

REFERENCES

1. Wiederhorn SM. Influence of water vapor on crack propagation in soda-lime glass. *J Am Ceram Soc.* 1967;50(8):407–414. <https://doi.org/10.1111/j.1151-2916.1967.tb15145.x>
2. Wiederhorn SM, Freiman SW, Fuller ER, Simmons CJ. Effects of water and other dielectrics on crack growth. *J Mater Sci.* 1982;17(12):3460–3478. <https://doi.org/10.1007/BF00752191>
3. Freiman SW, Wiederhorn SM, Mecholsky John J. J. Environmentally enhanced fracture of glass: A historical perspective. *J Am Ceram Soc.* 2009;92(7):1371–1382. <https://doi.org/10.1111/j.1551-2916.2009.03097.x>
4. Doremus RH. The Diffusion of water in fused silica. In: Mitchell JW, DeVries RC, Roberts RW, Cannon P, eds. *Reactivity of solids*. New York, NY: John Wiley & Sons; 1969:667–671.
5. Doremus RH. Diffusion of water in silica glass. *J Mater Res.* 1995;10(9):2379–2389. <https://doi.org/10.1557/JMR.1995.2379>
6. Davis KM, Tomozawa M. Water diffusion into silica glass: Structural changes in silica glass and their effect on water solubility and diffusivity. *J Non Cryst Solids.* 1995;185(3):203–220. [https://doi.org/10.1016/0022-3093\(95\)00015-1](https://doi.org/10.1016/0022-3093(95)00015-1)
7. Doremus RH. Diffusion-controlled reaction of water with glass. *J Non Cryst Solids.* 1983;55(1):143–147. [https://doi.org/10.1016/0022-3093\(83\)90014-5](https://doi.org/10.1016/0022-3093(83)90014-5)
8. Wakabayashi H, Tomozawa M. Diffusion of water into silica glass at low temperature. *J Am Ceram Soc.* 1989;72(10):1850–1855. <https://doi.org/10.1111/j.1151-2916.1989.tb05990.x>
9. Tomozawa M, Davis KM, Seaman JH, Aaldenberg EM. The origin of anomalous water diffusion in silica glasses at low temperatures. *J Am Ceram Soc.* 2017;100(10):4548–4561. <https://doi.org/10.1111/jace.14969>
10. Day DE, Stevels JM. Effect of dissolved water on the internal friction of glass. *J Non Cryst Solids.* 1974;14(1):165–177. [https://doi.org/10.1016/0022-3093\(74\)90027-1](https://doi.org/10.1016/0022-3093(74)90027-1)
11. Reinsch S, Müller R, Deubener J, Behrens H. Internal friction of hydrated soda-lime-silicate glasses. *J Chem Phys.* 2013;139(17):174506. <https://doi.org/10.1063/1.4828740>
12. Lezzi PJ, Tomozawa M, Blanchet TA. Evaluation of residual curvature in two-point bent glass fibers. *J Non Cryst Solids.* 2013;364(1):77–84. <https://doi.org/10.1016/j.jnoncrysol.2012.12.046>
13. Lezzi PJ, Tomozawa M. An overview of the strengthening of glass fibers by surface stress relaxation. *Int J Appl Glas Sci.* 2015;6(1):34–44. <https://doi.org/10.1111/ijag.12108>

14. Seaman JH, Blanchet TA, Tomozawa M. Origin of the static fatigue limit in oxide glasses. *J Am Ceram Soc.* 2016;99(11):3600–3609. <https://doi.org/10.1111/jace.14375>
15. Seaman JH, Lezzi PJ, Blanchet TA, Tomozawa M. Degradation of ion-exchange strengthened glasses due to surface stress relaxation. *J Non Cryst Solids.* 2014;403:113–123. <https://doi.org/10.1016/j.jnoncrysol.2014.07.016>
16. Lezzi PJ, Xiao QR, Tomozawa M, Blanchet TA, Kurkjian CR. Strength increase of silica glass fibers by surface stress relaxation: A new mechanical strengthening method. *J Non Cryst Solids.* 2013;379:95–106. <https://doi.org/10.1016/j.jnoncrysol.2013.07.033>
17. Nogami M, Tomozawa M. Effect of stress on water diffusion in silica glass. *J Am Ceram Soc.* 1984;67(2):151–154. <https://doi.org/10.1111/j.1151-2916.1984.tb09634.x>
18. Agarwal A, Tomozawa M, Lanford WA. Effect of stress on water diffusion in silica glass at various temperatures. *J Non Cryst Solids.* 1994;167(1):139–148. [https://doi.org/10.1016/0022-3093\(94\)90378-6](https://doi.org/10.1016/0022-3093(94)90378-6)
19. Davis KM. The diffusion of water into silica glass at low temperature [Doctoral dissertation]. Troy, NY: Rensselaer Polytechnic Institute; 1993
20. Tomozawa M, Hong JW, Hepburn RW, Lee YK, Peng YL. Surface relaxation of silica glass - permanent deformation of SiO₂ optical fibres at low temperatures. *Phys Chem Glas.* 2002;43C:503–507.
21. Lezzi PJ, Seaman JH, Tomozawa M. Strengthening of E-glass fibers by surface stress relaxation. *J Non Cryst Solids.* 2014;402:116–127. <https://doi.org/10.1016/j.jnoncrysol.2014.05.029>
22. Tomozawa M, Kim D-L, Agarwal A, Davis KM. Water diffusion and surface structural relaxation of silica glasses. *J Non Cryst Solids.* 2001;288(1–3):73–80. [https://doi.org/10.1016/S0022-3093\(01\)00648-2](https://doi.org/10.1016/S0022-3093(01)00648-2)
23. Aaldenberg EM, Aaldenberg JS, Blanchet TA, Tomozawa M. Surface shear stress relaxation of silica glass. *J Am Ceram Soc.* 2019;102(8):4573–4582. <https://doi.org/10.1111/jace.16342>
24. Crank J. A theoretical investigation of the influence of molecular relaxation and internal stress on diffusion in polymers. *J Polym Sci.* 1953;11(2):151–168. <https://doi.org/10.1002/pol.1953.120110206>
25. Crank J. *The mathematics of diffusion.* London, England: Oxford University Press; 1975
26. Alfrey T, Gurnee EF, Lloyd WG. Diffusion in glassy polymers. *J Polym Sci Part C Polym Symp.* 1966;12(1):249–261. <https://doi.org/10.1002/polc.5070120119>
27. Acocella J. The nature of dissolved water in sodium silicate glasses and its effect on various properties [Doctoral dissertation]. Troy, NY: Rensselaer Polytechnic Institute;

1983

28. Tomozawa M, Ito S, Molinelli J. Hygroscopicity of glasses with high water content. *J Non Cryst Solids*. 1984;64(1–2):269–278. [https://doi.org/10.1016/0022-3093\(84\)90222-9](https://doi.org/10.1016/0022-3093(84)90222-9)
29. Molinelli J, Tomozawa M, Takata M. Sodium transport in the Na₂O-H₂O-SiO₂ glass system. *J Am Ceram Soc*. 1985;68(3):165–168. <https://doi.org/10.1111/j.1151-2916.1985.tb09658.x>
30. Wang TT, Kwei TK, Frisch HL. Diffusion in glassy polymers. III. *J Polym Sci Part A-2 Polym Phys*. 1969;7(12):2019–2028. <https://doi.org/10.1002/pol.1969.160071204>
31. Thomas N., Windle A. A theory of case II diffusion. *Polymer (Guildf)*. 1982;23(4):529–542. [https://doi.org/10.1016/0032-3861\(82\)90093-3](https://doi.org/10.1016/0032-3861(82)90093-3)
32. Edwards DA, Cohen DS. A mathematical model for a dissolving polymer. *AIChE J*. 1995;41(11):2345–2355. <https://doi.org/10.1002/aic.690411102>
33. Tomozawa M, Molinelli J. Non-Fickian diffusion of water in glass. *Riv della Staz Sper Vetro*. 1984;(5):33–37.
34. Pedrotti FL, Pedrotti LM, Pedrotti LS. *Introduction to optics. 3rd ed.* Upper Saddle River, NJ: Cambridge University Press; 2007
35. Brewster D. On the laws which regulate the polarisation of light by reflexion from transparent bodies. *Philos Trans R Soc London*. 1815;105:125–159.
36. De Senarmont H. Sur les modifications que la réflexion spéculaire à la surface des corps métalliques imprime à un rayon de lumière polarisée. *Ann Chim Phys*. 1840;73:337–362.
37. Goranson RW, Adams LH. A method for the precise measurement of optical path-difference, especially in stressed glass. *J Franklin Inst*. 1933;216(4):475–504. [https://doi.org/10.1016/S0016-0032\(33\)90918-7](https://doi.org/10.1016/S0016-0032(33)90918-7)
38. Jessop HT. On the Tardy and Senarmont methods of measuring fractional relative retardations. *Br J Appl Phys*. 1953;4(5):138–141. <https://doi.org/10.1088/0508-3443/4/5/303>
39. Aben H, Guillemet C. *Photoelasticity of glass*. Berlin, Germany: Springer Berlin Heidelberg; 1993 <https://doi.org/10.1007/978-3-642-50071-8>
40. Jones RC. A new calculus for the treatment of optical systems I: Description and discussion of the calculus. *J Opt Soc Am*. 1941;31(7):488. <https://doi.org/10.1364/JOSA.31.000488>
41. Chu PL, Whitbread T. Measurement of stresses in optical fiber and preform. *Appl Opt*. 1982;21(23):4241. <https://doi.org/10.1364/AO.21.004241>

42. Mori A, Tomita R. Semi-automated Sénarmont method for measurement of small retardation. *Instrum Sci Technol*. 2015;43(4):379–389. <https://doi.org/10.1080/10739149.2014.1003072>
43. Hutsel MR, Ingle R, Gaylord TK. Accurate cross-sectional stress profiling of optical fibers. *Appl Opt*. 2009;48(26):4985. <https://doi.org/10.1364/AO.48.004985>
44. Hutsel MR, Ingle RR, Gaylord TK. Technique and apparatus for accurate cross-sectional stress profiling of optical fibers. *IEEE Trans Instrum Meas*. 2010;60(3):971–979. <https://doi.org/10.1109/TIM.2010.2062690>
45. Hutsel MR, Gaylord TK. Concurrent three-dimensional characterization of the refractive-index and residual-stress distributions in optical fibers. *Appl Opt*. 2012;51(22):5442–5452. <https://doi.org/10.1364/AO.51.005442>
46. Yablon AD, Yan MF, DiGiovanni DJ, *et al*. Frozen-in viscoelasticity for novel beam expanders and high-power connectors. *J Light Technol*. 2004;22(1):16–23.
47. Durr F, Limberger HG, Salathe RP, Yablon AD. Inelastic strain birefringence in optical fibers. Paper presented at the 2006 Optical Fiber Communication Conference and the National Fiber Optic Engineers Conference. March 5-10 2006; Anaheim, CA; <https://doi.org/10.1109/OFC.2006.215442> [proceedings paper – published]
48. Murach J, Brückner R. Preparation and structure-sensitive investigations on silica glass fibers. *J Non Cryst Solids*. 1997;211(3):250–261. [https://doi.org/10.1016/S0022-3093\(96\)00635-7](https://doi.org/10.1016/S0022-3093(96)00635-7)
49. Rongved L, Kurjian CR, Geyling FT. Mechanical tempering of optical fibers. *J Non Cryst Solids*. 1980;42(1):579–584. [https://doi.org/10.1016/0022-3093\(80\)90057-5](https://doi.org/10.1016/0022-3093(80)90057-5)
50. Brückner R, Murach J, Hao S. Generation and relaxation of flow birefringence of high-viscous alkali phosphate glass melts. *J Non Cryst Solids*. 1996;208(3):228–236. [https://doi.org/10.1016/S0022-3093\(96\)00516-9](https://doi.org/10.1016/S0022-3093(96)00516-9)
51. Takamori T, Tomozawa M. Birefringence and microstructure of anisotropic borosilicate glasses. *J Am Ceram Soc*. 1976;59(9–10):377–379. <https://doi.org/10.1111/j.1151-2916.1976.tb09499.x>
52. Brückner R, Yue Y. Non-Newtonian flow behaviour of glass melts as a consequence of viscoelasticity and anisotropic flow. *J Non Cryst Solids*. 1994;175(2):118–128. [https://doi.org/10.1016/0022-3093\(94\)90003-5](https://doi.org/10.1016/0022-3093(94)90003-5)
53. Wissuchek DJ, Ponader CW, Price JJ. Analysis of residual stress in optical fiber. In: Matthewson MJ, ed. *Optical fiber reliability and testing*. Vol. 3848. Boston, MA: SPIE; 1999:34–43. <https://doi.org/10.1117/12.372783> [proceedings paper – published]
54. Tomozawa M, Lezzi PJ, Hepburn RW, Blanchet TA, Cherniak DJ. Surface stress relaxation and resulting residual stress in glass fibers: A new mechanical strengthening

- mechanism of glasses. *J Non Cryst Solids*. 2012;358(18–19):2650–2662.
<https://doi.org/10.1016/j.jnoncrysol.2012.06.018>
55. Seaman JH, Lezzi P, A. Blanchet T, Tomozawa M. Modeling slow crack growth behavior of glass strengthened by a subcritical tensile stress using surface stress relaxation. *J Am Ceram Soc*. 2015;98(10):3075–3086. <https://doi.org/10.1111/jace.13710>
 56. Lezzi PJ, Tomozawa M, Hepburn RW. Confirmation of thin surface residual compressive stress in silica glass fiber by FTIR reflection spectroscopy. *J Non Cryst Solids*. 2014;390:13–18. <https://doi.org/10.1016/j.jnoncrysol.2014.02.021>
 57. Paek UC, Kurkjian CR. Calculation of cooling rate and induced stresses in drawing of optical fibers. *J Am Ceram Soc*. 1975;58(7–8):330–335. <https://doi.org/10.1111/j.1151-2916.1975.tb11490.x>
 58. Agarwal A, Davis KM, Tomozawa M. A simple IR spectroscopic method for determining fictive temperature of silica glasses. *J Non Cryst Solids*. 1995;185(1):191–198.
[https://doi.org/10.1016/0022-3093\(94\)00676-8](https://doi.org/10.1016/0022-3093(94)00676-8)
 59. Kuzuu N. Characteristic temperature, fictive temperature. In: Kawazoe H, ed. *Practical handbook for amorphous siliceous materials*. Tokyo, Japan: Realize Inc.; 1999:91–98.
 60. Jessop HT. On the Tardy and Sénarmont methods of measuring fractional relative retardations. *Br J Appl Phys*. 1953;4(5):138–141. <https://doi.org/10.1088/0508-3443/4/5/303>
 61. Park Y, Ahn T-J, Kim YH, Han W-T, Paek U-C, Kim DY. Measurement method for profiling the residual stress and the strain-optic coefficient of an optical fiber. *Appl Opt*. 2002;41(1):21–26. <https://doi.org/10.1364/AO.41.000021>
 62. Standard test method for measuring optical retardation and analyzing stress in glass. West Conshohocken, PA: ASTM International; 2019
 63. Acheroy S, Merken P, Ottevaere H, Geernaert T, Thienpont H, Berghmans F. Influence of measurement noise on the determination of the radial profile of the photoelastic coefficient in step-index optical fibers. *Appl Opt*. 2013;52(35):8451–8459.
<https://doi.org/10.1364/AO.52.008451>
 64. Sato T, Funamori N, Yagi T. Differential strain and residual anisotropy in silica glass. *J Appl Phys*. 2013;114(10):103509. <https://doi.org/10.1063/1.4820263>
 65. Champagnon B, Degioanni S, Martinet C. Anisotropic elastic deformation of silica glass under uniaxial stress. *J Appl Phys*. 2014;116(12):123509.
<https://doi.org/10.1063/1.4896401>
 66. Yablon AD. Optical and mechanical effects of frozen-in stresses and strains in optical fibers. *IEEE J Sel Top Quantum Electron*. 2004;10(2):300–311.
<https://doi.org/10.1109/JSTQE.2004.826570>

67. Scherer GW. Experimental studies of relaxation and creep. In: *Relaxation in glass and composites*. Malabar, FL: Krieger; 1992:41–46.
68. Tomozawa M, Koike A, Ryu S-R. Exponential structural relaxation of a high purity silica glass. *J Non Cryst Solids*. 2008;354(40–41):4685–4690.
<https://doi.org/10.1016/j.jnoncrysol.2008.07.005>
69. Koike A, Ryu SR-R, Tomozawa M. Adequacy test of the fictive temperatures of silica glasses determined by IR spectroscopy. *J Non Cryst Solids*. 2005;351(52):3797–3803.
<https://doi.org/10.1016/j.jnoncrysol.2005.10.005>
70. Aaldenberg EM, Tomozawa M. Composition fluctuation in silica glass containing water. *Am Ceram Soc Bull*. 2019;98(5):34–35.
71. Thomas GA, Shraiman BI, Glodls PF, Stephen MJ. Towards the clarity limit in optical fibre. *Nature*. 2000;404(6775):262–264. <https://doi.org/10.1038/35005034>
72. Kim BH, Han SR, Paek U-CC, Han W-TT. Diffusion of OH in optical fiber preform by oxy-hydrogen burner. *J Non Cryst Solids*. 2004;349(1–3):248–253.
<https://doi.org/10.1016/j.jnoncrysol.2004.08.150>
73. Lagakos N, Mohr R, El-Bayoumi OH. Stress optic coefficient and stress profile in optical fibers. *Appl Opt*. 1981;20(13):2309. <https://doi.org/10.1364/AO.20.002309>
74. Lezzi PJ, Seaman JH. Static fatigue and compressive stress generation in an aged crack. *J Am Ceram Soc*. 2018;101(4):1526–1536. <https://doi.org/10.1111/jace.15336>
75. Matthewson MJ, Kurkjian CR, Gulati ST. Strength measurement of optical fibers by bending. *J Am Ceram Soc*. 1986;69(11):815–821. <https://doi.org/10.1111/j.1151-2916.1986.tb07366.x>
76. Aben H, Guillemet C. Basic photoelasticity. In: *Photoelasticity of glass*. Berlin, Germany: Springer Berlin Heidelberg; 1993:51–68.
77. Hausmann BD, Miller PA, Aaldenberg EM, Blanchet TA, Tomozawa M. Modeling birefringence in SiO₂ glass fiber using surface stress relaxation. *J Am Ceram Soc*. 2020;103(3):1666–1676. <https://doi.org/10.1111/jace.16900>
78. Aaldenberg EM. Fast stress relaxation at the surface of silica glass : mechanism and effects [Doctoral dissertation]. Troy, NY: Rensselaer Polytechnic Institute; 2019
79. Onogi T, Inoue T, Osaki K. Shear birefringence measurement on amorphous polymers around the glass transition zone. *Nihon Reoroji Gakkaishi(Journal Soc Rheol Japan)*. 1998;26(4):237–241. https://doi.org/10.1678/rheology1973.26.4_237
80. Wiederhorn SM, Rizzi G, Wagner S, Hoffmann MJ, Fett T. Diffusion of water in silica glass in the absence of stresses. *J Am Ceram Soc*. 2017;100(9):3895–3902.
<https://doi.org/10.1111/jace.14937>

81. Brückner R. Properties and structure of vitreous silica. I. *J Non Cryst Solids*. 1970;5(2):123–175. [https://doi.org/10.1016/0022-3093\(70\)90190-0](https://doi.org/10.1016/0022-3093(70)90190-0)
82. Takata M, Acocella J, Tomozawa M, Watson EB. Effect of water content on the electrical conductivity of Na₂O-3SiO₂ glass. *J Am Ceram Soc*. 1981;64(12):719–724. <https://doi.org/10.1111/j.1151-2916.1981.tb15894.x>
83. Tomozawa M, Takata M, Acocella J, Watson EB, Takamori T. Thermal properties of Na₂O-3SiO₂ glasses with high water content. *J Non Cryst Solids*. 1983;56(1):343–348. [https://doi.org/10.1016/0022-3093\(83\)90491-X](https://doi.org/10.1016/0022-3093(83)90491-X)
84. Cox RW, Cohen DS. A mathematical model for stress-driven diffusion in polymers. *J Polym Sci Part B Polym Phys*. 1989;27(3):589–602. <https://doi.org/10.1002/POLB.1989.090270308>
85. Crank J, Park GS. Diffusion in high polymers: some anomalies and their significance. *Trans Faraday Soc*. 1951;47:1072–1084.
86. Shewmon P. *Diffusion in solids*. Cham, Switzerland: Springer International Publishing; 2016 <https://doi.org/10.1007/978-3-319-48206-4>
87. Tomozawa M, Takata M, Acocella J, Watson EB, Takamori T. Glass transition temperature of Na₂O * 3SiO₂ glasses with high water content. *Yogyo Kyokai Shi/Journal Ceram Soc Japan*. 1983;91(8):377–383.
88. Hausmann BD, Aaldenberg EM, Tomozawa M. Photoelastic confirmation of surface stress relaxation in silica glasses: Fiber bending and rod torsion. *J Am Ceram Soc*. 2021;104(7):3087–3096. <https://doi.org/10.1111/jace.17690>
89. Acheroy S, Merken P, Geernaert T, Ottevaere H, Thienpont H, Berghmans F. Algorithms for determining the radial profile of the photoelastic coefficient in glass and polymer optical fibers. *Opt Express*. 2015;23(15):18943–18954. <https://doi.org/10.1364/OE.23.018943>
90. Thomas NL, Windle AH. A deformation model for case II diffusion. *Polymer (Guildf)*. 1980;21(6):613–619. [https://doi.org/10.1016/0032-3861\(80\)90316-X](https://doi.org/10.1016/0032-3861(80)90316-X)

APPENDIX A: SÈNARMONT METHOD JONES MATRIX EVALUATION

Equation (1.14) is expanded below one Jones matrix multiplication at a time to show the effect of each element upon the input electric field vector, as shown in figure 1.7. The electric field vector emitted by each element will be designated 1 through 4 for each respective element.

Beginning with the vertical polarizer, equation (1.9):

$$E_1 = \begin{bmatrix} 0 & 0 \\ 0 & 1 \end{bmatrix} \cdot \begin{bmatrix} 1 \\ 1 \end{bmatrix}$$

$$E_1 = \begin{bmatrix} 0 \\ 1 \end{bmatrix} \tag{A.1}$$

Followed by the sample rotated 45 degrees, equation (1.11):

$$E_2 = \begin{bmatrix} \cos\left(\frac{\delta}{2}\right) & -i \cdot \sin\left(\frac{\delta}{2}\right) \\ -i \cdot \sin\left(\frac{\delta}{2}\right) & \cos\left(\frac{\delta}{2}\right) \end{bmatrix} \cdot E_1$$

$$= \begin{bmatrix} \cos\left(\frac{\delta}{2}\right) & -i \cdot \sin\left(\frac{\delta}{2}\right) \\ -i \cdot \sin\left(\frac{\delta}{2}\right) & \cos\left(\frac{\delta}{2}\right) \end{bmatrix} \cdot \begin{bmatrix} 0 \\ 1 \end{bmatrix} \tag{A.2}$$

$$= \begin{bmatrix} -i \cdot \sin\left(\frac{\delta}{2}\right) \\ \cos\left(\frac{\delta}{2}\right) \end{bmatrix}$$

Followed by the quarter wave plate, equation (1.12):

$$\begin{aligned}
E_3 &= \begin{bmatrix} e^{-i(\frac{\pi}{4})} & 0 \\ 0 & e^{i(\frac{\pi}{4})} \end{bmatrix} \cdot E_2 \\
&= \begin{bmatrix} e^{-i(\frac{\pi}{4})} & 0 \\ 0 & e^{i(\frac{\pi}{4})} \end{bmatrix} \cdot \begin{bmatrix} -i \cdot \sin\left(\frac{\delta}{2}\right) \\ \cos\left(\frac{\delta}{2}\right) \end{bmatrix} \\
&= \begin{bmatrix} \frac{\sqrt{2}}{2} \cdot (-1 - i) \cdot \sin\left(\frac{\delta}{2}\right) \\ \frac{\sqrt{2}}{2} \cdot (1 + i) \cdot \cos\left(\frac{\delta}{2}\right) \end{bmatrix}
\end{aligned} \tag{A.3}$$

Finally, through the analyzer at some angle θ , equation (1.13) resulting in equation (1.14):

$$\begin{aligned}
E_4 = E_{out} &= \begin{bmatrix} \cos^2(\theta) & \sin(\theta) \cos(\theta) \\ \sin(\theta) \cos(\theta) & \sin^2(\theta) \end{bmatrix} \cdot E_3 \\
&= \begin{bmatrix} \cos^2(\theta) & \sin(\theta) \cos(\theta) \\ \sin(\theta) \cos(\theta) & \sin^2(\theta) \end{bmatrix} \cdot \begin{bmatrix} \frac{\sqrt{2}}{2} \cdot (-1 - i) \cdot \sin\left(\frac{\delta}{2}\right) \\ \frac{\sqrt{2}}{2} \cdot (1 + i) \cdot \cos\left(\frac{\delta}{2}\right) \end{bmatrix} \\
&= \begin{bmatrix} \frac{\sqrt{2}}{2} \cdot (-1 - i) \cdot \cos(\theta) \cdot \left(\cos(\theta) \cdot \sin\left(\frac{\delta}{2}\right) - \cos\left(\frac{\delta}{2}\right) \cdot \sin\left(\frac{\delta}{2}\right) \right) \\ \frac{\sqrt{2}}{2} \cdot (-1 - i) \cdot \cos(\theta) \cdot \left(\cos(\theta) \cdot \sin\left(\frac{\delta}{2}\right) - \cos\left(\frac{\delta}{2}\right) \cdot \sin\left(\frac{\delta}{2}\right) \right) \end{bmatrix}
\end{aligned} \tag{A.4}$$

In order to calculate the magnitude of the electric field, which is proportional to the intensity of emitted light from the configuration (equation 1.15), you multiply the result of equation (A.4) by the transpose of the complex conjugate of E_4 . This is very similar in form to E_4 , with the only difference being the change in sign of the imaginary term:

$$E_4^* = \begin{bmatrix} \frac{\sqrt{2}}{2} \cdot (-1 + i) \cdot \cos(\theta) \cdot \left(\cos(\theta) \cdot \sin\left(\frac{\delta}{2}\right) - \cos\left(\frac{\delta}{2}\right) \cdot \sin\left(\frac{\delta}{2}\right) \right) \\ \frac{\sqrt{2}}{2} \cdot (-1 + i) \cdot \cos(\theta) \cdot \left(\cos(\theta) \cdot \sin\left(\frac{\delta}{2}\right) - \cos\left(\frac{\delta}{2}\right) \cdot \sin\left(\frac{\delta}{2}\right) \right) \end{bmatrix}^T \tag{A.5}$$

Multiplication of equations (A.4) and (A.5) simplifies to equation (1.15). Iterative application of the well-known “product-to-sum” trigonometric identities results in the final simplified form:

$$\begin{aligned} \frac{I}{I_o} \propto E_4 \cdot E_4^* &= \left[\frac{\sqrt{2}}{2} \cdot (-1 - i) \cdot \cos(\theta) \cdot \left(\cos(\theta) \cdot \sin\left(\frac{\delta}{2}\right) - \cos\left(\frac{\delta}{2}\right) \cdot \sin\left(\frac{\delta}{2}\right) \right) \right] \\ &\quad \left[\frac{\sqrt{2}}{2} \cdot (-1 + i) \cdot \cos(\theta) \cdot \left(\cos(\theta) \cdot \sin\left(\frac{\delta}{2}\right) - \cos\left(\frac{\delta}{2}\right) \cdot \sin\left(\frac{\delta}{2}\right) \right) \right]^T \\ &\quad \left[\frac{\sqrt{2}}{2} \cdot (-1 + i) \cdot \cos(\theta) \cdot \left(\cos(\theta) \cdot \sin\left(\frac{\delta}{2}\right) - \cos\left(\frac{\delta}{2}\right) \cdot \sin\left(\frac{\delta}{2}\right) \right) \right] \end{aligned} \quad (\text{A.6})$$

$$= -2 \cos^2(\theta) \cos^2\left(\frac{\delta}{2}\right) - 2 \sin\left(\frac{\delta}{2}\right) \sin(\theta) \cos\left(\frac{\delta}{2}\right) \cos(\theta) + \cos^2(\theta) + \cos^2\left(\frac{\delta}{2}\right)$$

$$= \frac{1}{2} - \frac{\cos(\delta - 2\theta)}{2}$$

APPENDIX B: FORCE BALANCE IN FIBER CROSS SECTION

FOUND BY DIFFERENT INTEGRATIONS

The development of surface stress relaxation models was performed considering the changes in stress as a function of radial position within the fiber, as shown in section 2.5. It is understood that the forces comprised of a surface compressive stress and interior tensile stress must balance in terms of total force on the material (in fact this must be true for residual stress in any material at rest with no external source of stress):

$$\int \sigma_{res} \cdot dA = 0 \quad (B.1)$$

where A is the area of the material cross section and σ_{res} is the residual stress as a function of position. Section 2.5 asserts that selecting radial or rectangular coordinates does not affect the result of this integration as long as the entire cross section of the material is used to calculate the net force. This is shown clearly in the case of radial coordinates integrated upon a residual surface compressive stress as it is assumed that for tensile stress relaxation the residual stress profile does not change based on what cross section diameter you select. In other words, from $-r_o$ to r_o (one fiber surface to the other), the stress profile does not change when the diameter chosen is rotated to any angular coordinate θ (figure B.1).

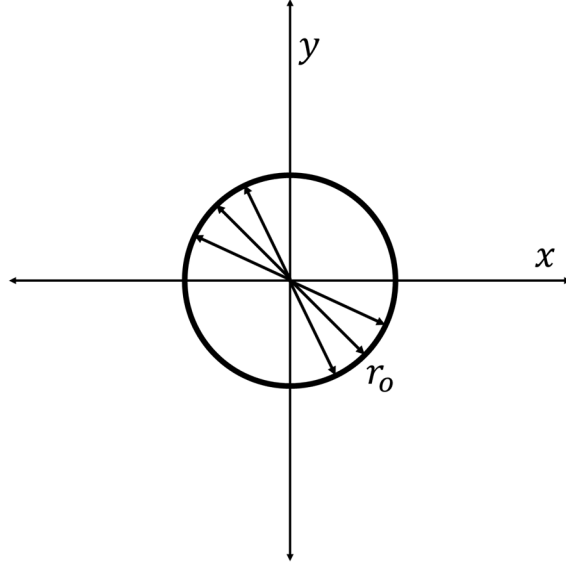


Figure B.1. Schematic of a fiber cross section showing equivalent stress profiles of equivalent diameter at different angles.

Mathematically, the same observation as made in figure B.1 can be expressed by a conversion of equation (B.1) into a double integral using radial coordinates:

$$\int_0^{2\pi} \int_{-r_0}^{r_0} \sigma_{res}(r, \theta) \cdot dr \cdot d\theta = 0 \quad (\text{B.2})$$

This same consideration is made using rectangular coordinates for the integration of stresses through the cross sectional height between y_{max} and y_{min} , which is analogous to the way in which the sample is observed via microscope (figure B.2).

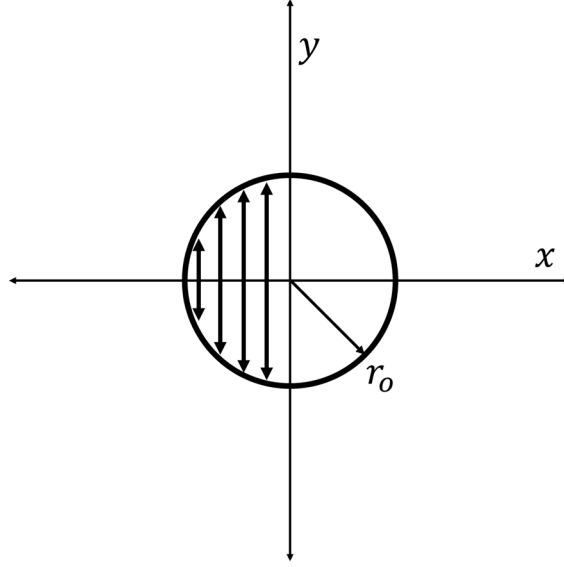


Figure B.2. Schematic of a fiber cross section showing the variation in path length as a function of x position.

Integration along paths in the x and y direction must give the same result as equation (B.2) as they are integrations of the same stress function within the same area:

$$\int_{y_{min}=-\sqrt{r_o^2-x^2}}^{y_{max}=\sqrt{r_o^2-x^2}} \int_{-r_o}^{r_o} \sigma_{res}(x, y) \cdot dx \cdot dy = 0 \quad (B.3)$$

where y_{min} and y_{max} are dictated by the fiber geometry and varies as a function of x position with a value ranging from zero at r_o to the fiber diameter at 0. It stands to reason therefore that equation (B.2) is equal to equation (B.3). Thus although the force balance expected for surface stress relaxation was originally developed using considerations of the radial area, it is also the case that integrations of residual stress as viewed from the microscope (integrated through the fiber path length with respect to y) as a function x are also expected to integrate to zero. This is the case described by equation (B.3) and is the case for retardance profiles $\Delta(x)$ as shown in results such as figure 2.4:

$$\Delta(x) = C \cdot \int_{y_{min}}^{y_{max}} \sigma(x, y) \cdot dy \quad (\text{B.4})$$

which is also to say assuming there is no externally applied force or other source of retardance beyond the residual stress:

$$\int_{-r_o}^{r_o} \Delta(x) \cdot dx = 0 \quad (\text{B.5})$$